FEDERAL UNIVERSITY OF SÃO CARLOS
CENTER FOR EXACT SCIENCES AND TECHNOLOGY
GRADUATE PROGRAM IN MATERIALS SCIENCE AND ENGINEERING

DESIGN, PRODUCTION AND ADVANCED CHARACTERIZATION OF CoCrFeMnNi-BASED MEDIUM- AND HIGH-ENTROPY ALLOYS: UNDERSTANDING THE INTERPLAY WITH COMPOSITION, MICROSTRUCTURE, AND MECHANICAL PROPERTIES

David Domingos Soares da Silva

São Carlos-SP
2024

FEDERAL UNIVERSITY OF SÃO CARLOS
CENTER FOR EXACT SCIENCES AND TECHNOLOGY
GRADUATE PROGRAM IN MATERIALS SCIENCE AND ENGINEERING

DESIGN, PRODUCTION AND ADVANCED CHARACTERIZATION OF CoCrFeMnNi-BASED MEDIUM- AND HIGH-ENTROPY ALLOYS: UNDERSTANDING THE INTERPLAY WITH COMPOSITION, MICROSTRUCTURE, AND MECHANICAL PROPERTIES

David Domingos Soares da Silva

A thesis submitted to Graduate Program in Materials Science and Engineering as requirement to obtain the title of DOCTOR IN MATERIALS SCIENCE AND ENGINEERING.

Advisor: Prof. Dr. Claudemiro Bolfarini
Co-advisor: Prof. Dr. Francisco Gil Coury
Funding agencies: Coordenação de Aperfeiçoamento de Pessoal de Nível Superior (CAPES/Brazil, grant number 88887.502322/2020-00) and Conselho Nacional de Desenvolvimento Científico e Tecnológico (CNPq/Brazil, grant number 200214/2022-5).

São Carlos-SP
2024

VITAE OF CANDIDATE

M.S. in Mechanical Engineering from Federal University of Paraiba (2020). B.S. in Mechanical Engineering from Federal University of Paraiba (2018).

UNIVERSIDADE FEDERAL DE SÃO CARLOS

Centro de Ciências Exatas e de Tecnologia

Programa de Pós-Graduação em Ciência e Engenharia de Materiais

Folha de Aprovação

Defesa de Tese de Doutorado do candidato David Domingos Soares da Silva, realizada em 12/04/2024.

Comissão Julgadora:

Prof. Dr. Claudemiro Bolfarini (UFSCar)

Prof. Dr. Eric Marchezini Mazzer (UFSCar)

Prof. Dr. Walter José Botta Filho (UFSCar)

Profa. Dra. Amy Jean Clarke (LANL)

Prof. Dr. Michael Joseph Kaufman (Mines)

O Relatório de Defesa assinado pelos membros da Comissão Julgadora encontra-se arquivado junto ao Programa de Pós-Graduação em Ciência e Engenharia de Materiais.

ACKNOWLEDGMENTS

I want to express my gratitude to my amazing wife, Caren Silva. Nothing would have any meaning without her support and affection. She has endured this journey with me, supported me from the beginning, and helped me overcome challenges. I love you!

I also thank my parents, Domingos and Eliane, and my brother Michael Douglas, for their unconditional love, support, and all the assistance that enabled me to take each step towards pursuing my dreams and life goals. Thank you for being my foundation. This victory is for you!

I am very grateful to my advisors, Dr. Claudemiro Bolfarini and Dr. Francisco Gil Coury, for their friendship and for dedicating their valuable time to guide and support me throughout this thesis project. By following in their footsteps, I have learned numerous lessons about science, and for that, I am immensely thankful.

I extend my appreciation to Dr. Michael Kaufman and Dr. Amy Clarke for all the opportunities they have offered me during the past year of working together at the Colorado School of Mines. Their guidance and assistance were of great importance for this work. It was truly an honor to learn from them.

I also would like to thank the Defense Committee for taking the time to read and evaluate my thesis. All of you are professors that I admire, and I feel honored to have such a strong committee.

I am grateful to PPGCEM/DEMa/UFSCar for the excellence in teaching and infrastructure, as well as to the Colorado School of Mines for providing me with all the necessary resources during my internship.

I would like to acknowledge the support from the Coordenação de Aperfeiçoamento de Pessoal de Nível Superior (CAPES/Brazil, grant number 88887.502322/2020-00), Conselho Nacional de Desenvolvimento Científico e Tecnológico (CNPq/Brazil, grant number 200214/2022-5), Fundação de Amparo à Pesquisa do Estado de São Paulo (FAPESP/Brazil, grant numbers 2022/02770-7 and 2023/03385-2), and the Center for Advanced Non-Ferrous Structural Alloys (CANFSA), a National Science Foundation Industry/University Cooperative Research Center (I/UCRC) [Award No. 2137243] at the Colorado School of Mines (CSM).

This study was financed in part by the Coordenação de Aperfeiçoamento de Pessoal de Nível Superior - Brasil (CAPES) - Finance Code 001.

Finally, I thank all my family and friends for their constant support.

ABSTRACT

Worldwide, a great research effort is being employed in the development of Medium/high entropy alloys (M/HEAs). Among the M/HEAs produced to date, great emphasis is given to the equiatomic $Co_{20}Cr_{20}Fe_{20}Mn_{20}Ni_{20}$ (at.%) alloy due to its good combination of strength and ductility. Studies in this field are increasingly being expanded to non-equiatomic compositions, and there is great opportunity in the development of M/HEAs with excellent mechanical properties. Therefore, based on thermodynamics calculations (CALPHAD method) novel non-equiatomic CoCrFeMnNi M/HEAs were designed aiming at obtaining optimized mechanical properties, tailoring deformation behaviors (TRIP-TWIP) via constituent concentrations. A total of 3 non-equiatomic M/HEAs ($Co_{15}Cr_{15}Fe_{50}Mn_{10}Ni_{10}$, $Co_{20}Cr_{20}Fe_{40}Mn_{10}Ni_{10}$, and $Co_{25}Cr_{25}Fe_{30}Mn_{10}Ni_{10}$) were produced; the alloys were then annealed, thermomechanically processed, characterized, and mechanically tested by tensile tests. The annealed and deformed samples were characterized by a combination of electron backscattered diffraction (EBSD), high-energy synchrotron X-ray diffraction (HE-SXRD), and transmission electron microscopy (TEM). It was revealed that increased Co and Cr reduced stacking fault energy (SFE), increasing recrystallization rate and suppressing grain growth rate. Grain refinement was more effective in the Co25Cr25 alloy, where the optimal strength-toughness occurred. Due to the decrease in SFE, a transition in the dominant deformation behavior occurred from TWIP (Co15Cr15) to TWIP/TRIP (Co20Cr20) and finally to TRIP (Co25Cr25), with the TRIP being more pronounced in Co25Cr25. This work sheds light on the development of novel FCC M/HEAs from the CoCrFeMnNi system, by identifying alloys that exhibit an optimal strength-ductility balance.

Keywords: Alloy design; Medium- and high-entropy alloys; Deformation mechanisms; Microstructure; Mechanical properties.

RESUMO

PROJETO, PRODUÇÃO E CARACTERIZAÇÃO AVANÇADA DE LIGAS DE MÉDIA E ALTA ENTROPIA À BASE DE CoCrFeMnNi: ENTENDENDO A INTERAÇÃO COM COMPOSIÇÃO, MICROESTRUTURA E PROPRIEDADES MECÂNICAS

Mundialmente, um grande esforço de pesquisa está sendo empregado no desenvolvimento de ligas de média e alta entropia (M/HEAs). Entre as M/HEAs produzidas até hoje, grande destaque é dado à liga equiatômica CoCrFeMnNi $Co_{20}Cr_{20}Fe_{20}Mn_{20}Ni_{20}$ (at.%) por sua boa combinação de resistência e ductilidade. Estudos nessa área estão sendo cada vez mais expandidos para composições não-equiatomicas, e há uma grande oportunidade no desenvolvimento de M/HEAs com excelentes propriedades mecânicas. Portanto, projetamos com base em cálculos termodinâmicos (método CALPHAD) novas M/HEAs CoCrFeMnNi não-equiatomicas visando obter propriedades mecânicas otimizadas, manipulando os comportamentos de deformação (TRIP-TWIP) através da modificação das concentrações dos constituintes. Um total de 3 não-equiatomicas M/HEAs ($Co_{15}Cr_{15}Fe_{50}Mn_{10}Ni_{10}$, $Co_{20}Cr_{20}Fe_{40}Mn_{10}Ni_{10}$ e $Co_{25}Cr_{25}Fe_{30}Mn_{10}Ni_{10}$) foram produzidas, as ligas foram então recozidas, processadas termomecanicamente, caracterizadas e testadas mecanicamente por ensaios de tração. As amostras recozidas e deformadas foram caracterizadas por uma combinação de difração de elétrons retroespalhados (EBSD), difração de raios X com radiação sincrotron de alta energia (HE-SXRD) e microscopia eletrônica de transmissão (TEM). Foi revelado que o aumento de Co e Cr reduziu a energia de falha de empilhamento (SFE), aumentando a taxa de recristalização e suprimindo a taxa de crescimento de grão. O refino de grão foi mais eficaz na liga Co25Cr25, onde a resistência-ductilidade ótima ocorreu. Devido à diminuição da SFE, ocorreu uma transição no comportamento de deformação dominante, de TWIP (Co15Cr15) para TWIP/TRIP (Co20Cr20) e, finalmente, para TRIP (Co25Cr25), sendo que o TRIP foi mais pronunciado em Co25Cr25. Este trabalho lança luz sobre o desenvolvimento de novas M/HEAs FCC do sistema CoCrFeMnNi, identificando ligas que exibem um equilíbrio ótimo entre resistência e ductilidade.

Palavras-chave: Design de liga; Ligas de média e alta entropia; Mecanismo de deformação; Microestrutura; Propriedades mecânicas.

PUBLICATIONS

- Peer-reviewed journals:

[1] David D.S. Silva, Alexandre R.C. Nascimento, Guilherme Y. Koga, Guilherme Zepon, Claudio S. Kiminami, Walter J. Botta, Claudemiro Bolfarini, ***Alloy design for microstructural-tailored boronmodified ferritic stainless steel to ensure corrosion and wear resistance***. Journal of Materials Research and Technology, v. 24, p. 418-429, 2023.

- Presentations at peer-reviewed conferences: oral and poster

[1] David Silva, Gustavo Bertoli, Nelson Neto, Michael Kaufman, Amy Clarke, Francisco Coury, Claudemiro Bolfarini, ***Computational thermodynamics-guided alloy design and phase stability in non-equimolar CoCrFeMnNi multi-principal element alloys: an experimental-theoretical study***, 3rd World Congress on High Entropy Alloys (HEA 2023), 2023, Pittsburgh, PA, USA.

[2] David Silva, Gustavo Bertoli, Michael Kaufman, Amy Clarke, Francisco Coury, Claudemiro Bolfarini, ***Study of the Grain Growth Kinetics and Hall-Petch Relationship in Fe-rich Multi-principal Element Alloys***, TMS 2023 Annual Meeting & Exhibition, 2023, San Diego, CA, USA.

x

CONTENT

Pág.

FOLHA DE APROVAÇÃO i
ACKNOWLEDGMENTS iii
ABSTRACT v
RESUMO vii
PUBLICATIONS ix
SUMÁRIO xi
LIST OF TABLES xiii
LIST OF FIGURES xv
1 INTRODUCTION AND BACKGROUND 1
1.1 Goals 2
1.1.1 Main goal 2
1.1.2 Specific goals 3
2 LITERATURE REVIEW 5
2.1 Brief history about high entropy alloys 5
2.2 M/HEAs from the CoCrFeMnNi family 6
2.3 Alloy design and phase prediction 7
2.3.1 Sigma phase prediction methods/criteria 8
2.4 Strength and deformation behavior of M/HEAs 10
2.4.1 Solid solution strengthening 10
2.4.2 Short-range ordering 10
2.4.3 Grain-boundary strengthening 11
2.4.4 Deformation mechanisms 12
3 MATERIALS AND METHODS 17
3.1 Alloy design and phase prediction 17
3.2 Alloy production and thermomechanical processing 19
3.3 Chemical, microstructural, and structural characterization 21
3.4 Grain growth kinetics analysis and mechanical properties 24
4 RESULTS AND DISCUSSION 25
4.1 Phase prediction using CALPHAD method 25
4.2 Sigma phase prediction using the Tsai criteria (VEC/PSFE) 30

4.3 Chemical, microstructural, and structural characterization 33
4.4 Comparative analysis of sigma phase prediction methods/criteria vs experimental data 38
4.5 Recrystallization, grain growth and mechanical properties.....40
5 SUMMARY AND CONCLUSIONS 59
6 RECOMMENDATIONS FOR FUTURE WORK.....61
7 REFERENCES 63

LIST OF TABLES

Table 3.1 - Sigma-free and sigma-prone binary systems of the CoCrFeMnNi at 900 °C, 1000 °C and 1100 ºC. Binary phase diagram data collected from ASM Handbook 19

Table 4.1 - Compositions of the M/HEAs (at.%), according to ICP-OES analysis 33

Table 4.2 - Content of interstitial elements (wt.%) in the M/HEAs, according to Leco® CS-844/ONH-836 analysis 33

Table 4.3 - Predicted vs experimentally observed phases for the studied M/HEAs compositions. Predictions by the CALPHAD method (at 900, 1000 and 1100 ºC) and by the Tsai Criteria (Sigma-free - VEC outside 6.88-7.84 *or* PSFE < 25%; sigma-prone - VEC inside 6.88-7.84 *and* PSFE > 40%; and Uncertain - VEC inside 6.88-7.84 *and* PSFE between 25% and 40%). Experimentally observed phases obtained by a combination of scanning electron microscopy (EDS, BSE and EBSD) and high-energy synchrotron X-ray diffraction in the thermal aging condition (at 900, 1000 and 1100 ºC for 20 h) 39

LIST OF FIGURES

Pág.

Figure 2.1 - Schematics of the HCP structure formation via shear deformation of the FCC matrix 14

Figure 3.1 - Schematic representation of the thermomechanical processing route followed to obtain two different final microstructures: I - recrystallized (samples annealed at 900 °C for 0.25 h, and II - thermally aged (samples subjected to thermal aging at 900 °C, 1000 °C, and 1100 °C for 20 h to allow the formation of the sigma phase). It should be noted that, although the first group of samples was recrystallized at 900 °C for 0.25 h (temperature at which sigma phase formation is predicted), due to its slow/moderate formation kinetics, sigma formation may be entirely suppressed. Therefore, the formation of the sigma phase is not expected in this recrystallized condition 20

Figure 3.2 - Schematic representation of the thermomechanical processing route followed to obtain 12 different recrystallized microstructures with different grain sizes.. 21

Figure 4.1 - Equilibrium volume fraction of phases calculated by the CALPHAD method at different temperatures for (a, d) $Co_{15}Cr_{15}$, (b, e) $Co_{20}Cr_{20}$ and (c, f) $Co_{25}Cr_{25}$ alloy. Thermo-Calc® software using TCHEA5 database, and Pandat® software using PanHEA2022 database were used to calculate Fig. 2 (a-c) and Fig. 2 (d-f), respectively. The highlighted regions in golden in the diagrams represent the temperatures chosen (900 °C, 1000 °C, and 1100 °C) to predict sigma phase formation. It should be noted that these thermodynamic calculations were performed under equilibrium conditions.... 26

Figure 4.2 - Pseudo-ternary phase diagram (in at.%) for the Fe-$Cr_{50}Co_{50}$-$Ni_{50}Mn_{50}$ system. All single-phase fields are identified. Panels (a, c, e, g) show the 1200 °C, 1100 °C, 1000 °C, and 900 °C isotherms, respectively, and Panels (b, d, f, h) display the calculated volume fraction of sigma phase (%) over the (FCC + σ) region predicted by Thermo-Calc® software using TCHEA5 database. Panels (i, k, m, o) show the 1200 °C, 1100 °C, 1000 °C, and 900 °C isotherms, respectively, and Panels (j, l, n, p) display the calculated volume fraction of sigma phase (%) over the (FCC + σ) region predicted by Pandat® software using PanHEA2022 database. The dark gray points in panels ((b,

d, f, h), (j, l, n, p)) depict predicted sigma phase fractions by the CALPHAD method. A Python code was developed for calculating additional data points within the range of known data points using bilinear interpolation. The colored stars in panels (a-p) represent the three alloys produced in this study. These thermodynamic calculations were performed under equilibrium conditions... 29

Figure 4.3 - Pseudo-ternary diagram (in at.%) for the Fe-$Cr_{50}Co_{50}$-$Ni_{50}Mn_{50}$ system for the prediction study of sigma phase formation using two empirical methods (Tsai criteria). (a) Valence electron concentration (VEC) and (b) Paired sigma-forming element (PSFE). It should be noted that different color bars are used for VEC (a) and PSFE (b) diagrams to better represent different ranges. Specifically, the color bar of VEC diagram represent from lowest values (red for weak intensity) to highest values (blue for strong intensity), while that in the PSFE diagram represent from lowest values (blue for weak intensity) to highest values (red for strong intensity). (c) correlation between PSFE and VEC for sigma phase prediction by the Tsai criteria indicated by the colored zones. Sigma-free (VEC outside 6.88-7.84 *or* PSFE < 25% - blue zone); sigma-prone (VEC inside 6.88-7.84 *and* PSFE > 40% - red zone); and Uncertain (VEC inside 6.88-7.84 *and* PSFE between 25% and 40% - light blue/red zone).. 32

Figure 4.4 - Representative microstructure of M/HEAs (samples recrystallized and thermally aged). EBSD inverse pole figures (IPFs) of (a, c, e, g) Co15Cr15, (I, k, m, o) Co20Cr20, and (q, s, u, w) Co25Cr25 M/HEAs. SEM-BSE images of the typical non-metallic inclusions (NMIs) found in (b, d, f, h) Co15Cr15, (j, l, n, p) Co20Cr20, and (r, t, v, x) Co25Cr25. ((b1-b9), (d1-d9), (f1-f9), (h1-h9), (j1-j9), (l1-l9), (n1-n9), (p1-p9), (r1-r9), (t1-t9), (v1-v9), and (x1-x9)) correspond to EDS mapping of the NMIs shown in (b, d, f, h) Co15Cr15, (j, l, n, p) Co20Cr20, and (r, t, v, x) Co25Cr25, respectively. The mean grain size ($\overline{d}$) of each alloy is also indicated in the IPFs.. 35

Figure 4.5 - Representative high-energy synchrotron X-ray diffraction patterns (logarithmic intensity scale) of the M/HEAs. (a) recrystallized at 900 °C for 0.25 h, (b) thermally aged at 900 °C for 20 h, (c) thermally aged at 1000 °C for 20 h, and (d) thermally aged at 1100 °C for 20 h. As shown, peaks of the FCC phase were predominantly observed, along with very weak signals corresponding to

non-metallic inclusions (NMIs) identified as oxides, sulfides, and carbides. The not indexed low-intensity diffraction peaks (dashed line) correspond to FCC phase reflections caused by the 2nd harmonic of the synchrotron beam. Notably, no indications of the sigma phase were detected.. 37

Figure 4.6 - Microstructure of the recrystallized M/HEAs. EBSD IPFs of Co15Cr15 alloy. The mean grain size ($\overline{\mathrm{d}}$) of each alloy is also indicated in each IPF.....42

Figure 4.7 - Microstructure of the recrystallized M/HEAs. EBSD IPFs of Co20Cr20 alloy. The mean grain size ($\overline{\mathrm{d}}$) of each alloy is also indicated in each IPF.....43

Figure 4.8 - Microstructure of the recrystallized M/HEAs. EBSD IPFs of Co25Cr25 alloy. The mean grain size ($\overline{d}$) of each alloy is also indicated in each IPF.....43

Figure 4.9 - Engineering stress-strain curves at room temperature of the recrystallized M/HEAs with different grain sizes. (a, b, c) Co15Cr15, (d, e, f) Co20Cr20, (g, h, i) Co25Cr25 M/HEAs annealed at 900, 1000 and 1100 °C for 0.25, 0.5, 1 and 2 h, respectively. The inserts in (a-i) summarize the mechanical properties of the alloys determined from tensile tests. σ_{y}, σ_{u}, and $\varepsilon_{\mathrm{UE}}$ refer to yield strength, ultimate tensile strength, and uniform elongation, respectively. σ_{y} was determined as the stress at which 0.2% plastic strain occurs.....46

Figure 4.10 - Hall–Petch plot of the yield strength (σ_y) as a function of the mean FCC grain size ($d^{-1/2}$), excluding twin boundaries, of the M/HEAs.. 48

Figure 4.11 - (a) Predicted Hall-Petch slope (k_{HP}) plotted over the pseudo-ternary diagram (in at.%) for the Fe-$Cr_{50}Co_{50}$-$Ni_{50}Mn_{50}$ system. (b) Predicted solid solution strengthening (σ_{ss}) determined by the Varvenne-EARS method, plotted over the same compositional space.....51

Figure 4.12 - (a) Representative engineering stress-strain curves at room temperature of the recrystallized M/HEAs (samples annealed at 900 °C for 0.25

h). (b) Product of strength and ductility ($\sigma_y.\varepsilon_{UE}$) against σ_y. (c) True stress-strain curves calculated from the engineering stress-strain curves.....54

Figure 4.13 - HE-SXRD pattern (a) before and (b) after tensile testing.....55

Figure 4.14 - (a1,a2; c1,c2; e1,e2) EBSD image quality (IQ) and phase maps of the Co15Cr15, Co20Cr20 and Co25Cr25 M/HEAs, respectively. (b1-b5, d1-d5, f1-f5) EDS maps of the Co15Cr15, Co20Cr20 and Co25Cr25 M/HEAs, respectively.....56

Figure 4.15 - (a1-a3, b1-b3, c1-c3) TEM analysis (bright field (BF), dark field (DF) and selected area electron diffraction (SAED) patterns of the Co15Cr15, Co20Cr20 and Co25Cr25 M/HEAs, respectively. The DF images were acquired using the $\{1\bar{1}1\}_{FCC}$ reflection for the Co15Cr15 and Co20Cr20 M/HEAs and $\{0001\}_{HCP}$ reflection for the Co25Cr25 HEA.....58

1 INTRODUCTION AND BACKGROUND

Medium/high entropy alloys (M/HEAs), complex concentrated alloys (CCAs), and multi-principal element alloys (MPEAs) are classes of materials that have been given a considerable amount of attention in the literature recently due to their high mechanical strength combined with ductility, high fracture toughness, excellent oxidation and corrosion resistance [1–3]. These attractive characteristics therefore make M/HEAs viable candidates for several applications, such as biomedical, energy, mechanical, and aerospace industries.

Unlike conventional alloys, which are normally composed of only one or two principal constituents, M/HEAs consist of a mixture of several main elements in an equal or near equal atomic ratio [3].

Initially, in order to maximize the configurational entropy and facilitate the formation of solid solutions, design of equiatomic M/HEAs were mainly considered [4,5]. However, the new trend is to develop non-equiatomic M/HEAs with single-phase, dual-phase or multi-phase solid solutions aiming optimized properties [6–8]. Thus, great focus has been given to the development of toughness and corrosion resistant alloys, an environment frequently found in several applications in the transportation and energy industries.

Among the different classes of M/HEAs under study, the equiatomic CoCrFeMnNi alloy is one of the most notable to date, and has attracted the interest of many researchers since its first production by Cantor in 2004 [9]. In addition, some compositions derived from the Cantor's alloy that can be highlighted is, for example, the equiatomic CrCoNi alloy, which is one of the toughest materials ever made [10].

Regarding the equiatomic CoCrFeMnNi alloy, although Cr (BCC – A2), Fe (BCC – A2), Ni (FCC – A1), Co (HCP – A3) and Mn (A12) have different crystal structures, their equimolar system surprisingly forms a single-phase structure (FCC). According to the growing number of research carried out in recent years, this alloy has good mechanical properties, combining excellent mechanical strength and ductility, making it a promising material [11,12].

Elements such as Fe, Ni and Mn are the FCC phase stabilizers whereas Co and Cr are the HCP phase stabilizers [13,14]. It means that the addition of Fe, Ni and/or Mn will stabilize the FCC phase meanwhile increase the stacking fault energy (SFE), whereas the addition of Co and/or Cr will stabilize the HCP phase and lower the SFE of the developed Fe-rich M/HEAs, which are comprised of metastable FCC phase at room temperature.

Therefore, having a clear design strategy of non-equiatomic M/HEAs is crucial to develop M/HEAs with optimized mechanical properties. In this regard, the recent development of M/HEAs with adjustable phase stabilities, triggering transformation-induced plasticity (TRIP) and/or twinning-induced plasticity (TWIP) effects [15] via modifying constituent concentrations has introduced an effective way to design high performance M/HEAs. Thus, it has both technological and scientific significance to develop M/HEAs with high performance.

Development of new M/HEAs based on thermodynamics calculations associated with in-depth characterization creates new interest in understanding the deformation mechanism (TRIP/TWIP), as well as the combined effect of these mechanisms. In addition, the complex interplay of elemental redistribution, the associated thermodynamics, kinetics of the deformation mechanisms and the importance of these mechanisms for M/HEAs have thus served as motivation for the present study.

1.1 Goals

1.1.1 Main goal

The main goal of this study is to systematically study the design, production and advanced characterization of CoCrFeMnNi-based medium- and high-entropy alloys with optimized mechanical properties.

1.1.2 Specific goals

To achieve the proposed aim, the following specific goals were considered:

- Perform computational thermodynamics-guided alloy design and phase stability in CoCrFeMnNi-based medium- and high-entropy alloys;
- Investigate through an in-depth characterization the underlying deformation mechanism (TRIP/TWIP), and thereby reveal the interrelationship between microstructure and mechanical properties of the newly developed M/HEAs;
- Establish a correlation between the obtained results to identify the best alloy that exhibit an optimal strength-ductility balance.

2 LITERATURE REVIEW

2.1 Brief history about high entropy alloys

The first results on high entropy alloys (HEAs) were published in 2004 [9] and since then, the field have significantly widened the idea of material design and provided new challenges to material scientists. Different from traditional alloys, such as steels or titanium alloys, which are normally composed of only one or two principal constituents, HEAs consist of at least five principal elements in an equal or near equal atomic ratio aiming at increasing the configurational entropy to form simple solid solutions, such as face-centered cubic (FCC), body-centered cubic (BCC) and hexagonal close-packed (HCP) microstructures [16].

In recent years, HEAs have very rapidly captured the attention of researchers, the world over due to their excellent properties, such as high fracture toughness at cryogenic temperatures [17], high strength at elevated temperatures [18] and excellent resistance to corrosion [19], indicating the promising potentials of the HEAs for harsh environmental applications.

Of the many works and reviews surveyed for this perspective, M/HEAs and associated research are contributing to the new era in metallurgy [20], where computer assisted design is becoming increasingly more important. There are several ways to assess this, but one poignant statement by Gorsse *et al.* [21], is that research into M/HEAs demands an ‘efficient exploration of hyper-dimensional design space’. The 67 stable metallic elements combine in 47,905 equiatomic ternary alloys, 766,480 quaternary ones, and about 10 million quinary ones [21]. In addition, it is still possible to design non-equiatomic alloys [22]. It is speculated that, in a not-too-distant future, it will be possible to design an “on-demand” HEA, highly specialized for a given application [3,23,24].

Up to now, several works on HEAs have been published, including several review papers [2,3,20,23,25–27] and two books [28,29] covering almost every aspect of current research on HEAs [23]. However, it is reasonable to say that our understanding and research on HEAs is just the tip of the iceberg, and due to the vast nature of the field, new data and discoveries are disclosed

continuously. Due to their remarkable properties and promising research prospects, many new findings in HEAs are emerging.

There are two main definitions of HEAs, by composition and entropy, which lead to some confusion and controversy that whether some alloys may be called HEAs [28]. Regarding the composition-based definition, to be considered HEAs, the maximum atomic composition of each element must be less than 35% atomic. This composition-based definition prescribes elemental concentrations only and places no bounds on the magnitude of entropy. In contrast, the other is based on the configurational entropy of a disordered phase, where HEAs have a configurational entropy (ΔS_{conf}) in a random state larger than 1.5R (R is the gas constant), no matter they are single phase or multiphases at room temperature [23]. However, although each definition of HEAs contains a wide range of alloys, both definitions overlap for the most part. Therefore, the definitions of HEAs are simply approximate guidelines, not strict laws [3,28].

2.2 M/HEAs from the CoCrFeMnNi family

Among the wide variety of HEAs, the equiatomic CoCrFeMnNi alloy, which is also referred to as Cantor's alloy [9], attracted extensive attention in the last decade [17,30,31]. Even though containing five components with different crystal structures, CoCrFeMnNi still possesses a single FCC solid solution structure [32].

Interestingly, this alloy exhibited outstanding damage tolerance and fracture toughness under cryogenic conditions, which is resulted from the nanotwins generated in the process of deformation [17,30]. This makes them highly desirable in the rapid-growing cryogenic applications such as liquid gas storage, fusion reactors, and medical devices [33]. However, its yield strength is unremarkable at ambient temperature, although its ductility is quite large [32].

In order to achieve superior strength-ductility combinations of M/HEAs, several research efforts have been devoted to either microstructure control [34] or compositional design [35]. For the microstructure control, many approaches

were proved effective in the improvement of mechanical properties. Such as introducing short-range order clusters [36], ultra-fine grains [31], uniformly distributed nanoprecipitates [37,38], high-density dislocations [39], high-density nano-twins and metastable phase [8,34], resulting in solid-solution strengthening, grain-refinement strengthening, precipitation strengthening, dislocation strengthening, twinning-induced plasticity (TWIP) and transformation-induced plasticity (TRIP) effects. However, the gain in ultra-high strength for M/HEAs through most conventional strengthening methods is generally accompanied by loss of ductility [40]. Thus, the trade-off between strength and ductility still widely exists based on the current strengthening methods. Therefore, desirable strengthening approaches are needed to improve the strength of CoCrFeMnNi without sacrificing its ductility.

2.3 Alloy design and phase prediction

Given the importance of predicting and understanding the microstructures of M/HEAs, various strategies have been developed over the past years to treat the thermodynamics of phase stability in complex alloys more fully, with varying degrees of success [27]. Therefore, predicting the phase constituents accurately in M/HEAs has been a great challenge not only from the fundamental point of view but also for various applications [29].

Numerous studies have attempted to relate phase stability to parameters such as size misfits, valence electron concentrations, electronegativities and mixing enthalpies [41,42]. However, many of these treatments ignore the formation enthalpies of competing compounds, typically intermetallic phases, which, limits their usefulness [27]. In addition, the overall accuracy of the existing physical models is still quite low, with the highest one around 72% and therefore, experimental methods are usually necessary to confirm these predictions [43].

The current computational methods for M/HEAs design include the calculation of phase diagrams (CALPHAD), the first principle calculation (e.g. the *ab-initio* calculation using density functional theory - DFT), molecular

dynamics (MD) and Monte Carlo (MC) [29]. Truly *ab-initio* calculations are computationally expensive, especially at finite temperatures [44,45]. Thus, they are probably best suited to screening narrow composition ranges that have already been identified as being of interest (based on other considerations) and when phase stabilities need to be predicted accurately [27].

Among these computational methods, CALPHAD-type approaches, which use software to calculate phase diagrams based on thermodynamic models, in general have broader applicability and have been shown to be useful in predicting phase stability in several cases [46,47].

This methodology is currently being expanded to alloy systems with a high number of components, targeting particularly the CoCrFeMnNi Cantor system [48]. The Redlich–Kistler functions in these cases also include higher-order interaction parameters, according to the number of components considered. However, outside of the fitted ranges and for cases in which competing intermetallic phases, such as sigma phase appear, this approach currently has limited predictive power [27], as reported by Bertoli *et al.* [22] and Bloomfield *et al.* [49]. Therefore, CALPHAD methods can serve as a first, albeit important, extrapolation step into unchartered compositional territory, as, very often, unexpected intermetallic phases appear [27].

2.3.1 Sigma phase prediction methods/criteria

The formation of sigma phase is a real concern when engineering FCC alloys are subjected to elevated temperatures (600-1000 °C) [50], and is often observed in this CoCrFeMnNi system [49–52]. Its precipitation is responsible for the embrittlement of the material and a consequent drastic reduction in toughness [53,54]. In addition, the sigma formation depletes the Cr content from the matrix, which lead to a loss of corrosion and oxidation resistance of the alloy [55,56]. Therefore, as the lifetime of components is directly affected by the degradation of these properties, predicting its formation is essential in alloy design.

Different methods/criteria are reported in the literature to predict the phase stability of a given alloy. The CALPHAD method uses thermodynamic models to calculate the phase stability in a system [57]. This method is well established in the literature and has proven to be an efficient tool in the study of large compositional fields [3,23,58]. However, the accuracy of CALPHAD predictions relies on the accuracy of the thermodynamic database used as input in the calculations. In addition, in the case of complex phases, such as sigma phase, this approach currently has limited predictive power, as previously mentioned. For this reason, Tsai *et al.* [59,60] formulated two complementary criteria to predict the formation of the sigma phase in Cr-containing M/HEAs.

The 1st Tsai criterion [59] is based upon the valence electron concentration (VEC) of the alloy, which is a weighted average (by atomic fraction) from the VEC of the constituent components (Cr = 6, Mn = 7, Fe = 8, Co = 9, Ni = 10) [3,59,61]:

$$VEC = \sum_{i=1}^{n} c_i (VEC)_i \quad (2.1)$$

where n is the number of components in the alloy, c_i and $(VEC)_i$ are the atomic fraction and VEC of the i^{th} component, respectively. According to the 1st Tsai criterion, the sigma phase is not formed in alloys with VEC value outside the range between 6.88 and 7.84. However, some binary alloys, even with the "correct" VEC to sigma phase formation, simply do not have sigma in their phase diagram, like the FeMn with a VEC of 7.5 does not form sigma phase [62]. For this reason, Tsai *et al.* [60] proposed a 2nd criterion that introduces a new parameter called "paired sigma-forming element" (PSFE).

The PSFE considers if the constituent elements are sigma-prone when in binary solution. Ideally, the binary sigma phase ($A_{50}B_{50}$) is formed by one A element (transition metals of groups VB-VIIB) and one B element (transition metals of groups VIIB-VIIIB) [22].

After defining the A and B elements of the system, the PSFE may be calculated according to Eq. (2.2) for an alloy consists of identifying the atomic concentration of A and B elements, then the PSFE will be double the lowest value obtained:

$$PSFE(c_A, c_B) = \begin{cases} 2\sum c_A, & if \frac{\sum c_A}{\sum c_B} \leq 1 \\ 2\sum c_B, & otherwise \end{cases} \quad (2.2)$$

where c_A and c_B are the vectors containing the atomic concentrations of the A and B elements, respectively. According to the 2nd Tsai criterion, the sigma phase does not form in alloys with PSFE < 20-25%, and forms in alloys with PSFE > 40-45%. Between these limits, the sigma phase may form or not.

2.4 Strength and deformation behavior of M/HEAs

2.4.1 Solid solution strengthening

Solid solution (SS) strengthening is perhaps the mechanism that attracted the most initial attention from the MPEA community. Disordered SS phases have a single crystal lattice and do not possess long rang ordering (LRO), however they may or may not display short-range ordering (SRO) [3].

Solid solution strengthening of M/HEAs can be attributed to the effect of lattice distortion caused by interstitial/substitutional atoms and SRO clusters, which usually impedes the dislocation movement [15,63]. However, according to Coury and co-workers [2], this does not mean that systems simply increasing the number of components will always increase the strength, since each system needs to be evaluated individually as the type and concentration of elements in SS are key to evaluate the degree of lattice distortion.

In summary, similar to traditional alloys, the efficiency of SS strengthening strongly depends on the nature of the solute atoms in M/HEAs (e.g., atomic radius, elastic properties, etc.) [2].

2.4.2 Short-range ordering

Apart from the interstitial or substitutional solute atoms, the formation of chemical short-range ordering (CSRO) or short-range ordering (SRO) for short, in HEAs has also attracted much of literature's attention recently. Some authors claim it can also induce a more severe lattice distortion and thus high SS strengthening [2].

SRO consists of specific preference/avoidance of some of the constituent species in the alloy away from the atomic fractions expected for random mixing, but the chemical order is so short-ranged that it prevails only in the first and the next couple of nearest-neighbor atomic shells around the atom at the center [3,64]. From a fundamental standpoint, the total energy of an atomic arrangement at 0 K is defined by the exact atomic position of each atom, so the smallest energetic difference between two different atomic pairings would be a driving force to SRO or even more often, to LRO into another crystal structure. On the other hand, at higher temperatures, often SRO can be disrupted and/or diminished by thermal energy [2].

Coury *et al.* [2] claim that the biggest point in discussion for M/HEAs is not if there is any driving force for SRO, but rather, if a significant content of SRO can be induced under feasible processing conditions and whether it will significantly affect mechanical properties.

The presence and effect of SRO has been confirmed by both the computational as well as experimental methods [65–67]. Nonetheless, experimental characterization of SRO in M/HEAs has been a challenging task because of the need to acquire detailed information on the atomic scale [65,68,69]. It is worth highlighting those indirect methods are also being used, which basically consist of detecting SRO effects on the mechanical properties such as stacking fault energy changes as well as variations on yield strength, hardness and strain hardening rate [2].

In summary, further research is necessary to understand the SRO formation and its effect on the properties of HEAs. The effective contribution of SRO to strength and operating deformation mechanisms is still open. More details about the SRO on M/HEAs may be found in reviews [2,66].

2.4.3 Grain-boundary strengthening

It is well known that grain refinement is probably one of the most desirable strengthening mechanisms since it is not only able to significantly

increase the mechanical properties with a combination of high strength and good ductility [8].

Numerous researches have shown that the grain size significantly affects the mechanical performance of M/HEAs and may be controlled by rolling and recrystallization [70–73].

Huang *et al.* [74] studied the recrystallization behavior, grain growth kinetics, and corresponding hardness variation of FeCoNiCrPd, FeCoNiCrMn, and their quaternary/ternary FCC-structured alloys annealed under different conditions. Experimental results indicated that the grain size and hardness of these M/HEAs followed the Hall–Petch (H-P) equation, with the H-P coefficient value being mainly dominated by the alloy's SFE and shear modulus.

Sun *et al.* [75] evaluated the temperature dependence of the H–P relationship in CoCrFeMnNi M/HEAs. Superior strength and ductility for the M/HEAs were achieved by refining grain size and decreasing temperature.

Recently, test conducted by Ondicho *et al.* [76] showed the effect of Fe on the H-P relationship of $(CoCrMnNi)_{100-x}$ Fe_x M/HEAs. Solid solution and grain boundary strengthening were significantly reduced at higher Fe content. In addition, the H-P coefficient decreases as the Fe content increases.

Although some studies have been conducted, the factors that affect the grain growth behavior of M/HEAs, as well as the determination of critical grain size that enables the optimal strength-ductility synergy to have not been fully clarified, although they are crucial for designing alloys for future engineering applications.

2.4.4 Deformation mechanisms

A considerable research interest in CoCrFeMnNi alloys lies in the operating deformation mechanisms on these alloys. As most FCC metals, these alloys display dislocation glide as the main deformation mode but depending on the composition and temperature, deformation twinning and phase transformation, FCC phase to HCP ε-martensite phase under deformation can also occur since alloys from this system can have low stacking fault energy

(SFE) values [77,78]. These are reported to generate plasticity increments due to a more pronounced work hardening rate, which leads to higher uniform elongation because of the Considère criterion [79]. These effects are typically called twinning induced plasticity (TWIP) and transformation induced plasticity (TRIP) and are being studied by multiple authors [2].

According to semi-empirical correlations [80], small to intermediate SFE favors twinning, whereas large SFE leads to narrowly dissociated or undissociated dislocations and thus dislocation glide is favored. Very small or negative SFE is known to be responsible for the TRIP effect [81]. Compiling data from steels, in general, the TRIP effect occurs when the SFE value is less than 20 mJ/m^2 and the TWIP effect when the SFE value is between 20 mJ/m^2 and 40 mJ/m^2. Steels with the SFE values between 15 mJ/m^2 and 25 mJ/m^2 undergo both TRIP and TWIP [79].

The sequence of HCP formation within the FCC matrix is depicted in Figure 2.1. The mechanisms of formation and evolution of ε-martensite (TRIP) and twins (TWIP) are in fact similar [2,82]. ε-martensite forms by the arrangement of intrinsic stacking faults on every second $\{111\}$ plane, whereas twins form by overlapping three stacking faults on successive planes [83]; stacking faults typically form by the dissociation of $\frac{1}{2}\langle 110\rangle\{111\}$ dislocations into $\frac{1}{6}\langle 112\rangle\{111\}$ Shockley partials. If a partial dislocation shears the lattice every plane a twin will form, if the process occurs every other plane an HCP lamella will be generated. Locally, the twin will have a stacking sequence of the "… ABA …" type, therefore, the same stacking sequence of the HCP phase [79]. The entire energetic pathway for this shearing process is of great interest and it is frequently studied by means of the generalized stacking fault energy (GSFE) curve of these alloys [13,84].

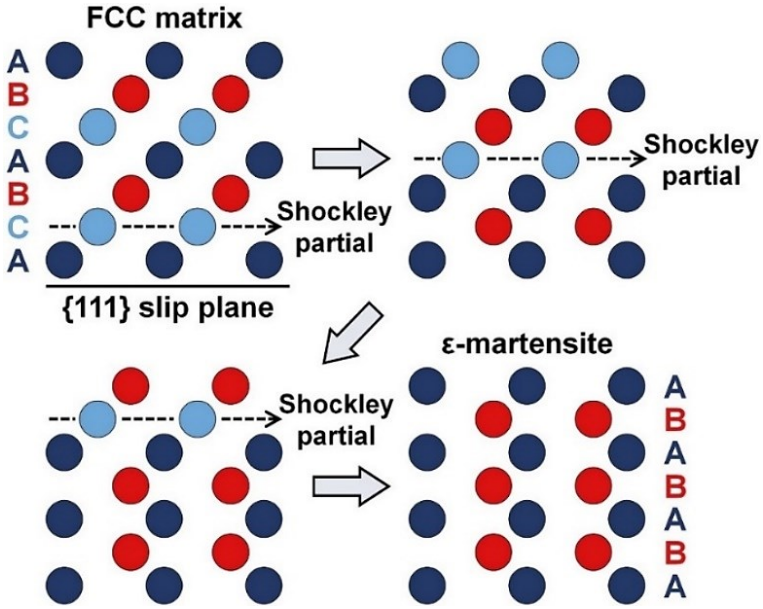

Figure 2.1 - Schematics of the HCP structure formation via shear deformation of the FCC matrix [81,85].

Generally, the SFE can be effectively tailored by adjusting the chemical composition of the alloy. Elements such as Fe, Ni and Mn are the FCC phase stabilizers whereas Co and Cr are the HCP phase stabilizers [13,14]. It means that the addition of Fe, Ni and/or Mn will stabilize the FCC phase meanwhile increase the stacking fault energy (SFE), whereas the addition of Co and/or Cr will stabilize the HCP phase and lower the SFE of the CoCrFeMnNi alloys, which are comprised of metastable FCC phase at room temperature.

Tests conducted by Wei *et al.* [13] confirmed through ab initio and thermodynamics calculations that decreasing the concentrations of Mn, Ni and Fe or increasing the concentrations of Co and Cr does lower the SFE and FCC phase stability of the M/HEAs. Small amounts of Al to FeCoNiCr, reduces the SFE significantly and induces deformation twinning [86]. Also, Wang *et al.* reported that addition of carbon into the $Fe_{40.4}Ni_{11.3}Mn_{34.8}Al_{7.5}Cr_6$ alloy reduced the SFE and significantly improved the mechanical properties [87]. In this regard, careful tailoring the chemical composition and controlling phase stability are important keys for further improvement of the mechanical performance.

It is also known that temperature is another factor that affects SFE. Chandan *et al.* [88] evaluated experimentally the variation in stacking fault energy for $Fe_{40}Mn_{40}Co_{10}Cr_{10}$ alloy with the change in temperature. The authors

reported that, owing to the decrease in SFE, a transition in the deformation behavior occurred from limited twin formation and slip dominance at room temperature to mixed-mode consisting of FCC→HCP transformation and twinning at -100 °C.

Otto *et al.* [30] performed a study of the mechanical properties of the CoCrFeMnNi HEA with special focus on the influence of temperature and microstructure. The alloy was tested at of 77, 293, 473, 673, 873 and 1073 K. It was proved that, the work hardening capability of the CoCrFeMnNi alloy decreases with increasing temperature. However, studies on the influences of temperature on deformation behavior and stacking fault energy of CoCrFeMnNi system has rarely been studied systematically so far, which is important not only for better understanding the resultant deformation mechanism, but also for properly designing M/HEAs with enhanced performance.

3 MATERIALS AND METHODS

3.1 Alloy design and phase prediction

The first stage of this work consisted of designing three non-equiatomic M/HEAs based on the CALPHAD method. The M/HEAs in the $Co_{((80-X)/2)}Cr_{((80-X)/2)}Fe_xMn_{10}Ni_{10}$ system, with x = 30, 40 and 50, at.%, were designed and resulted in the following nominal compositions: $Co_{15}Cr_{15}Fe_{50}Mn_{10}Ni_{10}$, $Co_{20}Cr_{20}Fe_{40}Mn_{10}Ni_{10}$, and $Co_{25}Cr_{25}Fe_{30}Mn_{10}Ni_{10}$ (at.%), hereinafter denoted by Co15Cr15, Co20Cr20 and Co25Cr25, respectively. Thermodynamic calculations were performed to estimate the equilibrium phases at different temperatures. These calculations were performed using two recent thermodynamic databases for HEAs, TCHEA5 (Thermo-Calc® software (version 2021b)) and PanHEA2022 (Pandat® software (version 2022)).

For the CoCrFeMnNi system, the TCHEA5 database describes 10/10 binary (fraction of assessed binaries f_{AB} = 1) and 5/10 ternary systems (fraction of assessed ternaries f_{AT} = 0.5) in the full range of compositions and temperatures. In contrast, the PanHEA2022 database fully describes 10/10 binaries (f_{AB} = 1) and 8/10 ternaries (f_{AT} = 0.8). Specifically, Miracle and Senkov [3] suggested that for a database to be suitable, it is important that f_{AB} = 1 and that one has the highest possible value of f_{AT}. Therefore, this comparative analysis will be performed here.

In this thesis, a systematic study was carried out with the newly designed Fe-rich M/HEAs. Two phase prediction methods, CALPHAD and also by the combination of two methods proposed by Tsai *et al.* [59,60], were applied for predicting the sigma phase. Both methods were applied to wide ranges of compositions. For the Tsai criteria predictions, a Python code was developed, it calculates the VEC and PSFE for each composition with increments of 0.5 at.%.

The isothermal aging treatments at 900 ºC, 1000 °C and 1100 °C were selected due to the fact that CALPHAD and Tsai criteria predictions for sigma phase formation diverged in some cases. Tsai et al. [59] discuss that applying and optimizing the criteria for a wider range of alloys and other temperatures is essential to improving knowledge about sigma phase formation in M/HEAs. As

in the case of this work, where the criteria were applied at three different temperatures, which are different from the 700 ºC originally considered in the criteria. Regarding the aging time, due to its slow formation kinetics, was chosen 20 h, since is more than sufficient time for sigma phase to form.

Both Tsai criteria (based upon VEC and PSFE) predict that the alloys will be: i) sigma-free if the VEC is outside the range of 6.88 and 7.84 OR the PSFE is lower than 20-25%; ii) sigma-prone if the VEC is within the range of 6.88 and 7.84 AND the PSFE is higher than 40-45%; iii) uncertain about the sigma phase formation if none of the previous two items are met. Note that, to further reduce the field of uncertainty, were established as lower and upper PSFE limits as 25% and 40%, respectively.

For the CoCrFeMnNi system, the A elements is only Cr, whereas the B elements could be Mn, Fe, Co and Ni. In order to obtain greater accuracy in the predictions, all binary phase diagrams [62] of this system were consulted to identify those that exhibit the sigma phase at three different temperatures, 900 ºC, 1000 °C and 1100 °C, temperatures at which the heat treatments were carried out in this work.

Based on Table 3.1, the A/B elements (or neither) should be divided as best as possible for each system/subsystem. In the CoCrFeMnNi system, Cr serves as an A element and initially would have Mn, Fe, Co and Ni as possible B elements to form sigma. However, consulting the Cr-Mn, Cr-Fe, Cr-Co and Cr-Ni binary phase diagrams [62], only the Cr-Mn, Cr-Fe and Cr-Co alloys form the sigma phase at 900 ºC, 1000 °C and 1100 °C (see Table 3.1). Thus, only Mn, Fe and Co serve as B elements when paired with Cr. That way, Ni is not a B element. Therefore, in the CoCrFeMnNi system at 1100, 1000 and 900 °C: Cr is A element; Mn, Fe and Co are B elements; and Ni is neither A nor B element.

Table 3.1 – Sigma-free and sigma-prone binary systems of the CoCrFeMnNi at 900 °C, 1000 °C and 1100 ºC. Binary phase diagram data collected from ASM Handbook [62].

		B elements (VIIB-VIIIB groups)			
		Mn	**Fe**	**Co**	**Ni**
A elements (VIB-VIIB groups)	**Cr**	Sigma-prone	Sigma-free (T > 830 ºC)	Sigma-prone	Sigma-free
	Mn	----------	Sigma-free	Sigma-free (T > 550 ºC)	Sigma-free

Both prediction methods (CALPHAD and Tsai criteria) were compared which the experimental characterization by a combination of X-ray diffraction (XRD) and electron backscattering diffraction (EBSD), where the sigma phase can be readily detected by the appearance of extra diffraction peaks on the aged samples or by metallographic analysis. Therefore, the accuracy of the predictions by these different approaches was critically assessed. The discussion presented here is important to guide further studies, especially in the CoCrFeMnNi system.

3.2 Alloy production and thermomechanical processing

The ingots were produced by vacuum induction melting. All raw materials used for casting the alloys were commercially available pure elements, not specifically high purity, and inevitably produce nonmetallic inclusions (NMIs) during casting. Prior to melting, the Mn was cleaned in an aqueous solution of 5% HCl in distilled water and then in 1% HNO_3 in acetone. Afterward, it was cleaned in ultrasonic baths of alcohol for 10 min and dried with compressed air. This cleaning procedure was performed immediately before adding the Mn to the other materials in the vacuum induction furnace. Additionally, an excess of approximately 10% of the original Mn mass was added to compensate for Mn loss due to its relatively high vapor pressure at high temperatures, which can lead to some weight loss as a result of volatilization during melting [89]. In addition, ≈ 0.5 at.% Al was added as a deoxidizer to avoid large angular oxide

inclusions; the remaining metallic Al fraction should remain in solid solution with negligible impact on the solid solution strengthening component and yield strength [73,90].

Fig. 3.1 shows a schematic representation of the thermomechanical processing route followed for the alloy design and phase stability study. After production, the as-cast ingots were subsequently homogenized at 1200 °C for 2 h followed by water quenching. The homogenized alloys were hot rolled at 1100 °C with a total rolling reduction ratio of ≈ 87.5% followed by water quenching. After hot rolling, the alloys were cold-rolled with a total reduction ratio of ≈ 50%. Samples with dimensions 10 x 10 x 1 mm^3 were prepared by wire electrical discharge machining (EDM) from the alloy sheets. The first group of samples were then annealed at 900 °C for 0.25 h followed by water quenching to obtain fully recrystallized microstructures, whereas the second group of samples were aged at 900 °C, 1000 °C, and 1100 °C for 20 h followed by water-quenching to allow the formation of the sigma phase.

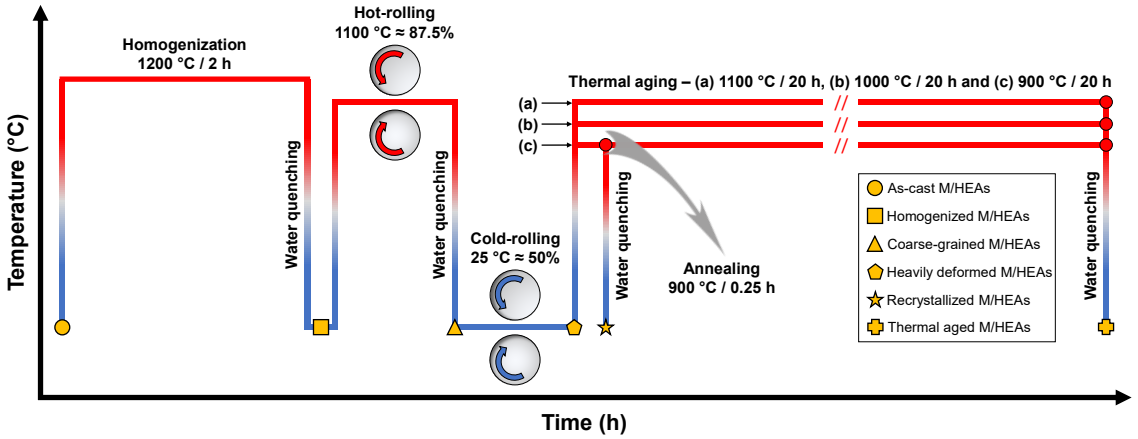

Figure 3.1 - Schematic representation of the thermomechanical processing route followed to obtain two different final microstructures: I - recrystallized (samples annealed at 900 °C for 0.25 h, and II - thermally aged (samples subjected to thermal aging at 900 °C, 1000 °C, and 1100 °C for 20 h to allow the formation of the sigma phase). It should be noted that, although the first group of samples was recrystallized at 900 °C for 0.25 h (temperature at which sigma phase formation is predicted), due to its slow/moderate formation kinetics, sigma formation may be entirely suppressed. Therefore, the formation of the sigma phase is not expected in this recrystallized condition.

Fig. 3.2 shows a schematic representation of the thermomechanical processing route followed for the recrystallization, grain growth and Hall-Petch relationship study. The cast ingots were homogenized at 1200 °C for 2 h, followed by water-quenching. They were then hot-rolled at 1100 °C to a thickness reduction of 87.5%, followed by water-quenching. To refine the grain size, the samples were cold-rolled to a thickness reduction of 50%. Subsequently, to achieve materials with different grain sizes and fully recrystallized, the cold-rolled plates were annealed at varying temperatures and times (900, 1000, and 1100°C for 0.25, 0.5, 1, and 2 h) followed by water-quenching.

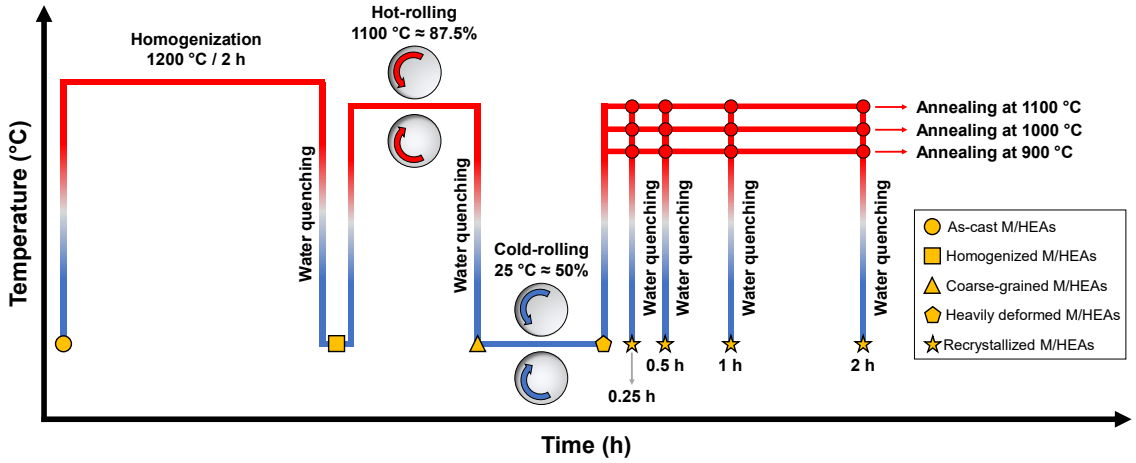

Figure 3.2 - Schematic representation of the thermomechanical processing route followed to obtain 12 different recrystallized microstructures with different grain sizes.

3.3 Chemical, microstructural, and structural characterization

Chemical analysis of the major alloying elements (Co, Cr, Fe, Mn, Ni and Al) was carried out using inductively coupled plasma-optical emission spectrometry (ICP-OES, Thermo 6000). In addition, the interstitial elements (C, S, O, N, and H) were also determined - C and S by direct combustion in a Leco® CS-844 analyzer, O and H by infrared absorption radiation, and N by thermal conductivity in a Leco® ONH-836 analyzer.

The microstructures of the M/HEAs were investigated using a TESCAN S8252G scanning electron microscope (SEM) equipped with energy dispersive

spectroscopy (EDS) and backscattered electron (BSE) detectors. A FEI Helios Nanolab 600i was used for electron backscatter diffraction (EBSD) analysis. The samples were mechanically polished and finished using a 1 µm diamond suspension. In addition, residual stresses, caused by the earlier stages of mechanical polishing, were relieved by a final vibratory polishing step using an aqueous suspension of colloidal silica (0.05 µm) for 24 h. Structural and chemical analyses of the microstructures were investigated with SEM-BSE/EDS at an acceleration voltage of 15 kV, a probe current of 1.4 nA, and a working distance of 10 mm. For the EBSD measurements, different step sizes ranging at an acceleration voltage of 20 kV and probe current of 11 nA were used to characterize the microstructures of the samples with different grain sizes. The raw EBSD data were post-processed using the analysis tools for electron and X-ray diffraction, ATEX-software [91], and eventually the inverse pole figure (IPF), pole figure (PF), phase mapping, and grain size were obtained. Only high-angle grain boundaries (HAGBs) with misorientations (θ) ≥ 15°, excluding twin boundaries (TBs), were considered, when measuring the mean grain sizes ($\overline{d}$). For this purpose, a minimum of 200 grains was considered.

Transmission electron microscopy (TEM) was performed using an FEI Tecnai T12 microscope operating at 120 kV. TEM foils were prepared using an FEI Helios 600 Focused Ion Beam (FIB) system. A final thinning step using 2 kV accelerating voltage was used to minimize the beam damage to the sample.

High-energy synchrotron X-ray diffraction (HE-SXRD) was also used to identify the phase structure evolution. The synchrotron experiments were performed at the P07B High Energy Materials Science beamline of PETRA III/DESY [92]. A high-photon beam energy of 87.1 KeV, corresponding to a wavelength of 0.14235 Å, was used and the beam size was 200 µm x 200 µm. This photon energy allowed performing diffraction experiments in transmission mode, enabling the determination of bulk microstructure information. LaB_6 powder was used as a standard for the calibration of the instrument parameters, and to determine the sample-to-detector distance (1322.5 mm). A two-dimensional PerkinElmer fast detector with pixel size of 200 x 200 μm^2 was used to collect the Debbye-Scherrer rings. After the collection of the 2D images,

post-processing of the raw diffraction data was performed using a combination of tools (pyFAI-calib2 and pyFAI-integrate [93]) based on Python. Phase fractions were calculated by a direct-comparison XRD method using integrated peak intensities.

At the P07B beamline, caution was exercised while indexing the XRD patterns, due to the presence of higher harmonics, such as the 2nd harmonic of the intended energy of 87.1 keV, which can pass through the crystal monochromator, affecting measurements and data analysis. This issue has been previously acknowledged in studies conducted at the same beamline [94–97]. Nonetheless, the exact position of such harmonics can easily be determined so as not to compromise the quality of the overall results.

The peak broadening of the diffraction peak profile enables us to determine the dislocation density [98]. Here, we adopted the well-established modified Williamson–Hall (WH) [99,100]. For this analysis, we used the full azimuthal angle (φ range from 0 to 360°) integration obtained via GSAS II software [101]. The first step was to obtain the position at 2θ and the full width at half maximum (FWHM) of at least three peaks from the same phase. Next, it was necessary to subtract the instrumental broadening ($FWHM_{instrumental}$) from the broadening measured ($FWHM_{measured}$), according to Eq. (3.1), to obtain the broadening of the material/sample ($FWHM_{sample}$). A LaB_6 powder standard was used to obtain instrumental peak broadening, as mentioned previously. As the broadening depends on the diffraction angle, the FWHM was measured for ten peaks of the LaB_6 pattern, and using a linear fitting the instrumental broadening was obtained as a function of the position at 2θ of the peaks.

$$FWHM_{sample}^2 = FWHM_{measured}^2 - FWHM_{instrumental}^2 \quad (3.1)$$

The modified WH method is described by the Eqs. (3.2-3.5), where: θ is the diffraction angle (input); $FWHM_{sample}$ is the peak full width of half maximum of the sample (input); λ is the radiation wavelength (1.4235 nm); d is the crystallite size (output); M is a dimensionless parameter depending on the effective outer cut-off radius of dislocations, initially taken as 2.0 [102]; b is the average Burgers vector (0.254 nm); ρi is the initial dislocation density, (output, m^{-2}); $\bar{C}$ is the average contrast factor of dislocations; $\bar{C}_{h00}$ and q can be

calculated for an FCC crystal using the methodology shown in [103]. Here, a uniform distribution of screw and edge dislocations was assumed. H^2 is a dependent factor calculated from the (hkl) Miller indices for each peak.

$$\frac{2\cos(\theta)FWHM_{sample}}{\lambda} = \frac{0.9}{d} + \left(\frac{\pi M^2 b^2}{2}\right)^{1/2} \rho^{1/2} \left(\frac{2sin(\theta)}{\lambda} \bar{C}^{1/2}\right) \quad (3.2)$$

$$\bar{C} = \bar{C}_{h00}(1 - qH^2) \quad (3.3)$$

$$H^2 = \frac{h^2k^2 + k^2l^2 + l^2h^2}{(h^2 + k^2 + l^2)^2} \quad (3.4)$$

$$\rho i = \frac{2AC^2}{\pi M^2 b^2} \quad (3.5)$$

3.4 Grain growth kinetics analysis and mechanical properties

A scanning electron microscope (SEM, FEI Helios Nanolab 600i) equipped with an energy dispersive spectroscopy (EDS) and electron back-scattering diffraction (EBSD) detectors was used to observe the microstructures and phase compositions of the alloys. During the EBSD measurement, different step sizes ranging from 0.3 μm to 2 μm at an acceleration voltage of 20 kV and probe current of 11 nA were used to characterize the samples with different grain sizes. The raw EBSD data were post-processed using the analysis tools for electron and X-ray diffraction, ATEX-software [91]. Only high-angle grain boundaries (HAGBs) with misorientation (θ) ≥ 15°, excluding twin boundaries (TBs), were considered to measure the mean grain sizes ($\overline{d}$).

Subsize tensile samples with a gauge dimension of 25 x 6 x 1 mm^3, following the ASTM E8/E8M-16 standard [104], were cut from cold-rolled sheets using electrical discharge machining with their longitudinal axes parallel to the rolling direction. Quasi-static uniaxial tensile tests were performed at room temperature on an INSTRON 5500R testing machine with a nominal strain rate of 1 x 10^{-3} s^{-1}. The strain of the gage section was precisely measured using an INSTRON advanced video extensometer. Three samples for each alloy were tested to ensure data reproducibility in this work.

4 RESULTS AND DISCUSSION

4.1 Phase prediction using CALPHAD method

Phase predictions under equilibrium at temperatures from above the liquidus temperature down to 600 °C are plotted in Fig. 4.1 (a-f) using TCHEA5 database (Fig. 4.1 (a-c)) and PanHEA2022 database (Fig. 4.1 (d-f). As shown in Fig. 4.1 (a-f), for both databases, the three alloys are predicted to be single-phase FCC at 1200 °C. Thus, this temperature was chosen for the homogenization heat treatment, as previously mentioned. Sigma phase is predicted to form from the FCC phase after solidification is complete, but not until temperatures below 1180 °C (Fig. 4.1 (c)) and 912 °C (Fig. 4.1 (d)) were attained, depending on the alloy and database, with increasing volume fractions at lower temperatures (600-900 °C). Fig. 4.1 (a-f) also shows that when selecting the temperature range between 900 °C and 1100 °C, the phases predictions using TCHEA5 database (Fig. 4.1 (a-c)) and PanHEA2022 database (Fig. 4.1 (a-c)) completely diverged. Therefore, to assess the accuracy of the CALPHAD method by using two different databases for predicting the formation of the sigma phase, temperatures of 900 °C, 1000 °C, and 1100 °C were selected for thermal aging treatments.

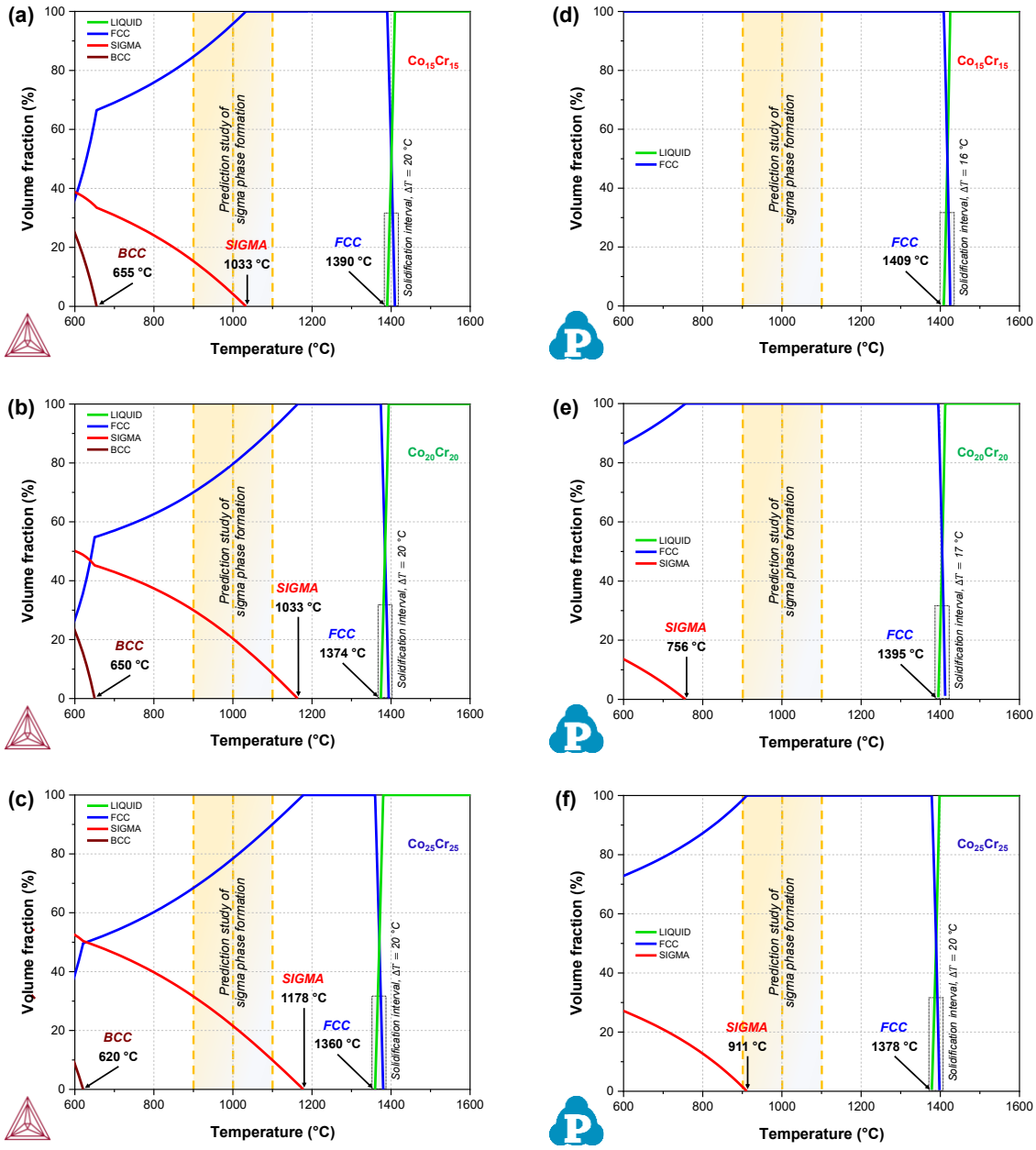

Figure 4.1 - Equilibrium volume fraction of phases calculated by the CALPHAD method at different temperatures for (a, d) $Co_{15}Cr_{15}$, (b, e) $Co_{20}Cr_{20}$ and (c, f) $Co_{25}Cr_{25}$ alloy. Thermo-Calc® software using TCHEA5 database, and Pandat® software using PanHEA2022 database were used to calculate Fig. 2 (a-c) and Fig. 2 (d-f), respectively. The highlighted regions in golden in the diagrams represent the temperatures chosen (900 °C, 1000 °C, and 1100 °C) to predict sigma phase formation. It should be noted that these thermodynamic calculations were performed under equilibrium conditions.

Fig. 4.2 (a-p) shows the CALPHAD phase equilibria predictions for Fe-$Cr_{50}Co_{50}$-$Ni_{50}Mn_{50}$ pseudo-ternary phase diagrams at 1200, 1100, 1000, and 900 °C. As can be seen, decreasing the temperature from 1200 to 1100, 1000 , and 900 °C, the FCC phase field shrinks significantly and favors the formation of the sigma phase, especially for the Cr and Co-rich alloys. However, when comparing the CALPHAD predictions using the TCHEA5 (Fig. 4.2 (a-h)) and PanHEA2022 (Fig. 4.2 (i-p)) databases results have revealed a completely different behavior. On the one hand, the calculations using the TCHEA5 database predicted the formation of sigma phase for the Co20Cr20 and Co25Cr25 alloys at 1100 °C and for the three alloys (Co15Cr15, Co20Cr20, and Co25Cr25) at 1000 and 900 °C. On the other hand, the sigma phase formation was only predicted for the Co25Cr25 alloy at 900 °C when the PanHEA2022 database was used, highlighting the importance of database selection.

To date, several works have shown that comparisons between CALPHAD predictions using the TCHEA1 and TCHEA3 databases and experimental results have revealed an underestimation in the temperature range, where the sigma phase remains stable, thereby representing a question of the fidelity of the prediction [49,52,105,106]. To ensure the viability of the CALPHAD method and accuracy of the database used, it is critical to compare predictions to the experimental data.

Otto *et al.* [107] investigated the phase stability of the equiatomic CoCrFeMnNi alloy widely accepted as a single-phase FCC solid solution. They performed long thermal aging treatment at 900 °C, 700 °C, and 500 °C for 500 days, and found the FCC phase remains stable at 900 °C, however sigma phase forms at 700 °C and three different phases form at 500 °C. Since then, many publications have reported sigma formation in a series of non-equiatomic M/HEAs in the CoCrFeMnNi system. To improve our understanding of phase stability in the CoCrFeMnNi system, it is necessary to determine the effect of each constituent element on phase equilibria.

Previous investigators have studied the effects of alloying elements on the phase stability in the CoCrFeMnNi system, and it is well established that the sigma phase is strongly stabilized by both Cr and Mn, with Cr playing a much

more significant role than Mn, or the combination of Cr with Mn [50,51,106,108,109]. In contrast, Ni, Co, and Fe are strong FCC stabilizers, suppressing the formation of the sigma phase [49,52,109–111]. To date, similarly detailed studies have not been conducted, when simultaneously varying Co and Cr in equivalent ratios, at the expense of Fe, while keeping Ni and Mn constant, and as a result, the synergistic effects of these elements remain unclear.

Independent of database used, the CALPHAD calculations presented in Fig. 4.2 indicate a pronounced Cr-driven stabilization of the sigma phase, outweighing the influence of Co on FCC phase stability. A concurrent increase in Co and Cr concentrations in equivalent ratios yields a higher volumetric fraction of the predicted sigma phase, rendering it progressively thermodynamically favored, irrespective of temperature.

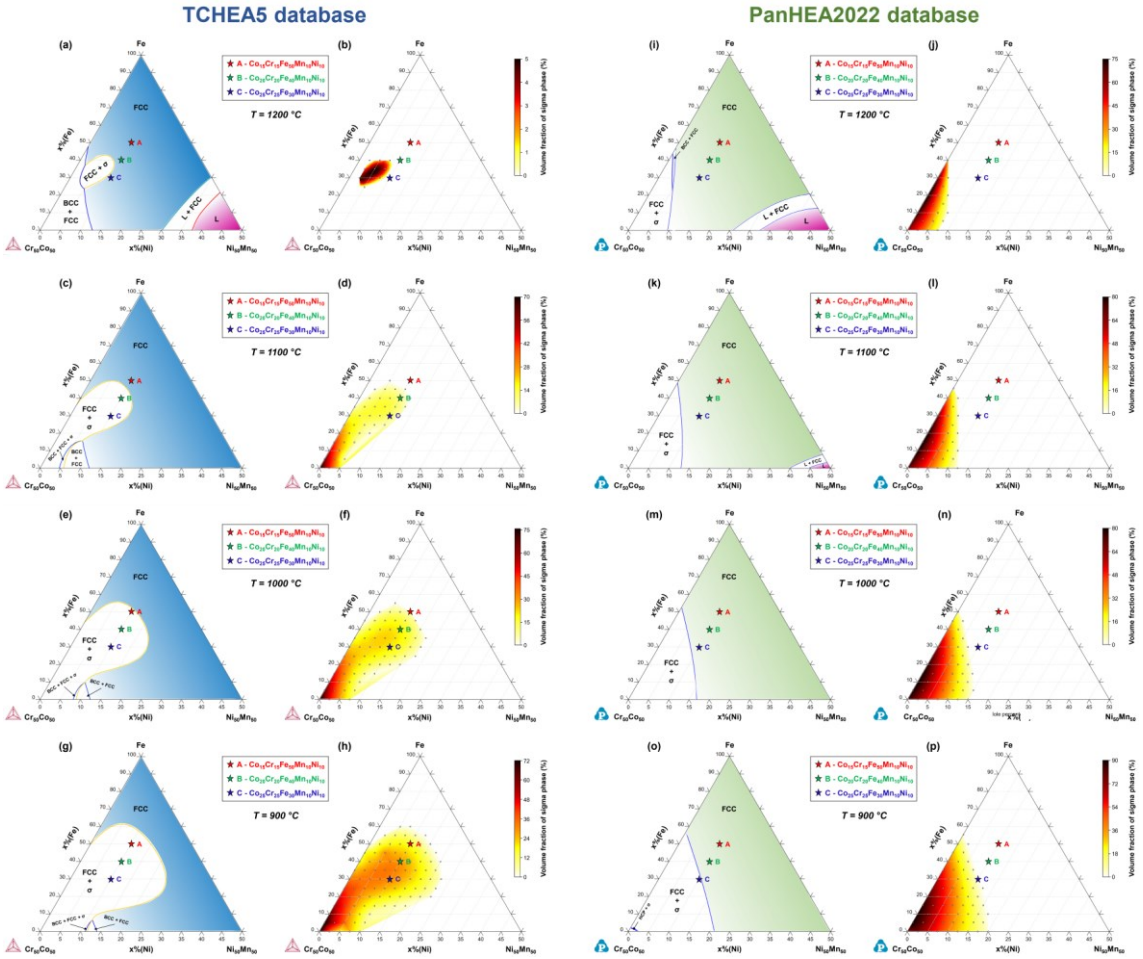

Figure 4.2 - Pseudo-ternary phase diagram (in at.%) for the Fe-$Cr_{50}Co_{50}$-$Ni_{50}Mn_{50}$ system. All single-phase fields are identified. Panels (a, c, e, g) show the 1200 °C, 1100 °C, 1000 °C, and 900 °C isotherms, respectively, and Panels (b, d, f, h) display the calculated volume fraction of sigma phase (%) over the (FCC + σ) region predicted by Thermo-Calc® software using TCHEA5 database. Panels (i, k, m, o) show the 1200 °C, 1100 °C, 1000 °C, and 900 °C isotherms, respectively, and Panels (j, l, n, p) display the calculated volume fraction of sigma phase (%) over the (FCC + σ) region predicted by Pandat® software using PanHEA2022 database. The dark gray points in panels ((b, d, f, h), (j, l, n, p)) depict predicted sigma phase fractions by the CALPHAD method. A Python code was developed for calculating additional data points within the range of known data points using bilinear interpolation. The colored stars in panels (a-p) represent the three alloys produced in this study. These thermodynamic calculations were performed under equilibrium conditions.

4.2 Sigma phase prediction using the Tsai criteria (VEC/PSFE)

Tsai criteria predictions using two empirical methods, VEC and PSFE, are shown in Fig. 4.3 To further explore the dimension of the compositional fields, the predictions were expanded to a wide range of compositions, in which pseudo-ternary diagrams for the Fe-$Cr_{50}Co_{50}$-$Ni_{50}Mn_{50}$ system are presented in Fig. 4.3 (a, b) for the VEC and PSFE predictions, respectively. Furthermore, to make the Tsai criteria clearer and more intuitive, a graphical representation was generated, as shown in Fig. 4.3 (c). Through the correlation between PSFE and VEC, three distinct zones can be observed: sigma-free, sigma-prone, and uncertain, as shown in Fig. 4.3 (c). To further reduce the field of uncertainty, lower and upper PSFE limits of 25% and 40% were established, respectively. Therefore, if the PSFE value is between 25% and 40%, it is unclear whether the sigma phase will form or not.

Despite observing the same trend in the increase in driving force for sigma phase formation (concurrent increase in Co and Cr concentrations in equivalent ratios) when compared to the thermodynamic calculations predicted by the CALPHAD method, the Tsai criteria predictions (Fig. 4.3) diverged from the CALPHAD predictions using the TCHEA5 database (Fig. 4.2 (a-h)), since the Tsai criteria did not predict sigma phase formation for the alloys studied. However, special attention should be paid to the Co20Cr20 and Co25Cr25 alloys, since these alloys present the VEC and PSFE close to the boundary for sigma phase formation, i.e., VEC = 7.90; PSFE = 40% for the Co20Cr20 alloy and VEC = 7.85; PSFE = 50% for the Co25Cr25 alloy.

Laplanche *et al.* [50] studied the kinetics of sigma phase precipitation in an initially single-phase FCC non-equiatomic $Cr_{26}Mn_{20}Fe_{20}Co_{20}Ni_{14}$ HEA. Thermal aging was performed between 600 °C and 1080 °C for times ranging from 0.05 h to 1000 h. The results revealed that grain boundaries acted as preferential nucleation sites for the sigma phase after short annealing periods. However, with longer aging times, the sigma phase was also observed within the grains. For instance, when this alloy was thermally aged for 10 h at 900 °C and 1000 °C, approximately 5% and 12% of sigma phase were formed,

respectively. It's noteworthy that this alloy presents VEC = 7.76 and PFSE = 52%, i.e., sigma-prone.

Recently, Bertoli *et al.* [22] assessed the use of the CALPHAD method and Tsai criteria to aid the study of phase equilibria in the VCrMnFeCo system. Their findings revealed that the CALPHAD method, applied with three distinct databases (TCHEA3, PanHEA2020, and PanHEA2022), and Tsai criteria predictions diverged in some cases, and both were partially accurate when compared to experimental characterization. Therefore, the use of different predictive methods together appears to offer significant advantages for the design of stable M/HEAs.

The application of this approach is somewhat limited, due to the temperature-dependent nature of the critical VEC/PSFE range at which sigma phase formation becomes probable. Furthermore, plastic deformation during cold rolling can also accelerate sigma phase formation within HEAs by providing heterogeneous nucleation sites within the grains [31]. Consequently, an alloy that initially appears to be sigma-free can exhibit sigma phase formation when these variables are considered. As a result, a substantial volume of experimental data is necessary to precisely define these critical ranges. Moreover, it is important to emphasize that the validation of these empirical methods (VEC/PSFE) demands precise experimental investigations, since the overall accuracy of the existing physical models is still quite low, with the highest one around 72% [43], as mentioned previously.

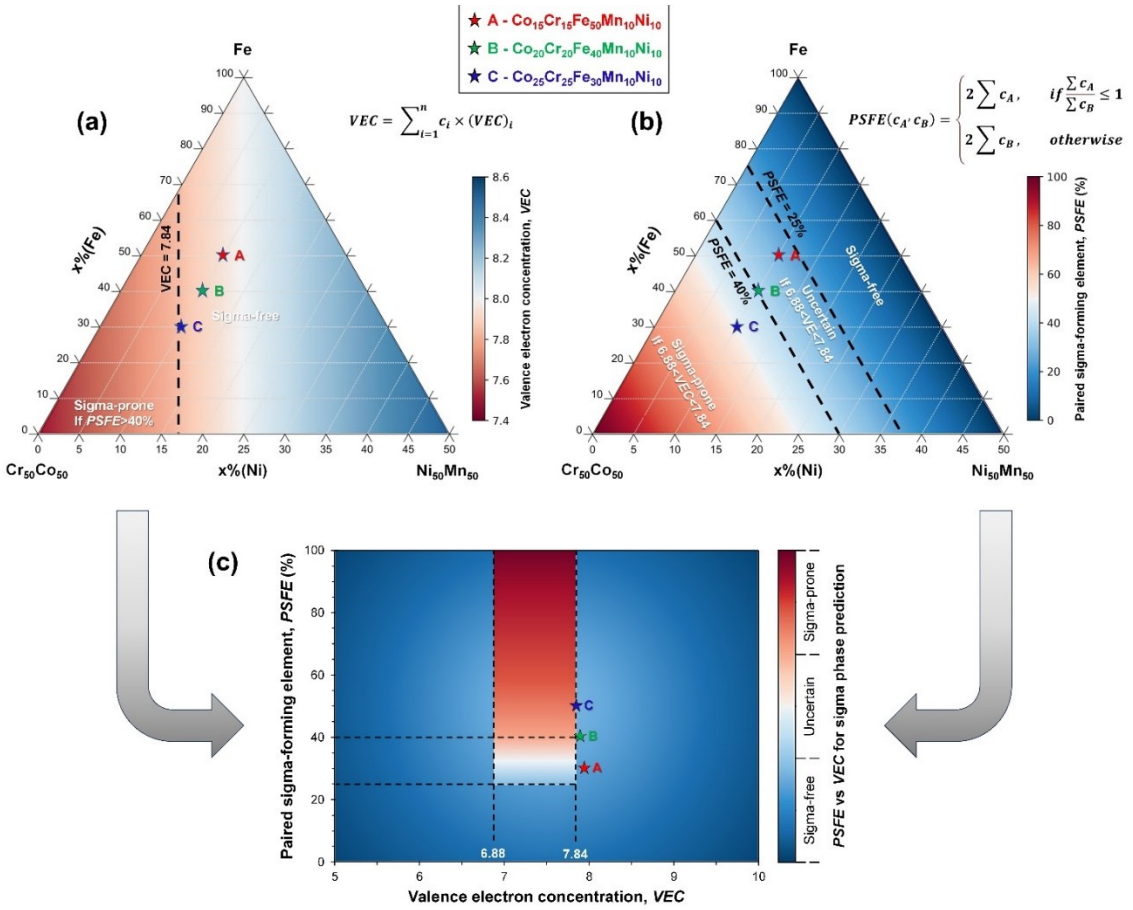

Figure 4.3 - Pseudo-ternary diagram (in at.%) for the Fe-$Cr_{50}Co_{50}$-$Ni_{50}Mn_{50}$ system for the prediction study of sigma phase formation using two empirical methods (Tsai criteria). (a) Valence electron concentration (VEC) and (b) Paired sigma-forming element (PSFE). It should be noted that different color bars are used for VEC (a) and PSFE (b) diagrams to better represent different ranges. Specifically, the color bar of VEC diagram represent from lowest values (red for weak intensity) to highest values (blue for strong intensity), while that in the PSFE diagram represent from lowest values (blue for weak intensity) to highest values (red for strong intensity). (c) correlation between PSFE and VEC for sigma phase prediction by the Tsai criteria indicated by the colored zones. Sigma-free (VEC outside 6.88-7.84 *or* PSFE < 25% - blue zone); sigma-prone (VEC inside 6.88-7.84 *and* PSFE > 40% - red zone); and Uncertain (VEC inside 6.88-7.84 *and* PSFE between 25% and 40% - light blue/red zone).

4.3 Chemical, microstructural, and structural characterization

The composition of the M/HEAs (at.%), as well as the content of interstitial elements (wt.%), are given in Table 4.1 and Table 4.2, respectively. The actual compositions, determined using chemical analysis (ICP-OES), deviate only slightly from the designed compositions, see Table 4.1. The total contents of C, S, O, N, and H, measured by Leco® CS-844 and Leco® ONH-836, were below 355 ppm, 65 ppm, 315 ppm, 225 ppm and 35 ppm, respectively, for all alloys, as indicated in Table 4.2. Therefore, all the thermodynamic calculations described here only considered the substitutional elements. The presence of these interstitial elements is highly likely due to contamination of the melting equipment and the starting feedstocks used in the fabrication of the alloys. It is worth noting that it is extremely difficult to reduce the number of non-metallic inclusions (NMIs) to a low level, when using commercially available pure elements and common vacuum casting methods. One effective way to minimize the content of NMIs is to use high-purity raw materials and high-vacuum production techniques [112].

Table 4.1 - Compositions of the M/HEAs (at.%), according to ICP-OES analysis.

Sample	Nominal concentration	Measured composition					
		Co	Cr	Fe	Mn	Ni	Al
Co15Cr15	$Co_{15}Cr_{15}Fe_{50}Mn_{10}Ni_{10}$	14.9	13.8	49.5	11.4	10.3	0.1
Co20Cr20	$Co_{20}Cr_{20}Fe_{40}Mn_{10}Ni_{10}$	19.3	18.5	39.4	11.6	11.1	0.1
Co25Cr25	$Co_{25}Cr_{25}Fe_{30}Mn_{10}Ni_{10}$	24.3	22.2	32.5	10.4	10.5	0.1

Table 4.2 - Content of interstitial elements (wt.%) in the M/HEAs, according to Leco® CS-844/ONH-836 analysis.

Sample	Interstitial elements				
	C	S	O	N	H
Co15Cr15	0.017	0.006	0.009	0.010	0.003
Co20Cr20	0.026	0.005	0.017	0.013	0.002
Co25Cr25	0.035	0.005	0.031	0.022	0.002

Representative microstructures of recrystallized and aged samples are presented in Fig. 4.4. The EBSD IPF analysis reveals the average grain sizes (excluding twin boundaries) range from 4.0 to 156.5 μm (Co15Cr15), 3.8 to 75.4 μm (Co20Cr20), and 2.7 to 67.3 μm (Co25Cr25) compared to the recrystallized sample (900 °C for 0.25 h) and the 1100 °C, 20 h condition. Consequently, the percentage increase in average grain size for the Co15Cr15 alloy is ≈ 1.6 times greater than that of the Co25Cr25 alloy in terms of order of magnitude. It implies these alloys present different grain growth kinetics.

Despite 20 h of aging at the chosen temperatures (900 °C, 1000 °C, and 1100 °C), it was observed that the sigma phase did not form in any of these alloys. Instead, all alloys consistently retained a single FCC phase. Although Co is not as effective as Ni in suppressing the formation of the sigma phase, it does stabilize the FCC phase, and its effect must be considered. Bloomfield *et al.* [49] studied the effect of Co on the phase stability of the $CrMnFeCo_xNi$ system, where x = 0, 0.5, and 1.5. The alloys contained 0, 11.1, and 27.27 at.% Co, respectively. It was shown that for the two alloys containing Co, single FCC phase was obtained in the homogenized condition. Exposures at 900 °C and 700 °C for 1000 h resulted in the formation of sigma phase in the alloy containing 11.1 at.% Co, but not in the alloy containing 27.27 at.% Co. Therefore, these data, in conjunction with previously published results, indicate that Co stabilizes the FCC matrix in this temperature range. Here in the CoCrFeMnNi-based M/HEAs studied, the Co and Cr content simultaneously changed, at the expense of Fe, while keeping Ni and Mn constant.

Unlike the sigma phase that can be avoided if alloy compositions or heat treatments are well designed based on thermodynamic principles, nonmetallic inclusions (NMIs), e.g., oxides, sulfides and/or carbides are inevitable compounds in many engineering alloys that can be introduced unintentionally through normal production routes/service atmospheres [112–115]. Although the oxygen, sulfur, and carbon concentrations in the M/HEAs were at ppm levels, see Table 4.2, NMIs were observed.

To further clarify the microstructure and elemental composition, SEM-BSE/EDS analysis was performed; the results are also shown in Fig. 4.4. Based

on SEM-BSE/EDS qualitative analysis, the NMIs consist of a mixture of oxide, sulfide, and carbide compounds, categorized as follows: Al-rich, (Mn,Al)-rich, and (Mn,Cr)-rich oxides; Mn-rich sulfides; and Cr-rich and Mn-rich carbides. A detailed analysis of composition and structure of the NMIs is beyond the scope of this work. In future work, these data should be considered, as NMIs, including their fraction, size distribution, morphology, and composition, may have a direct impact on the final properties of the material.

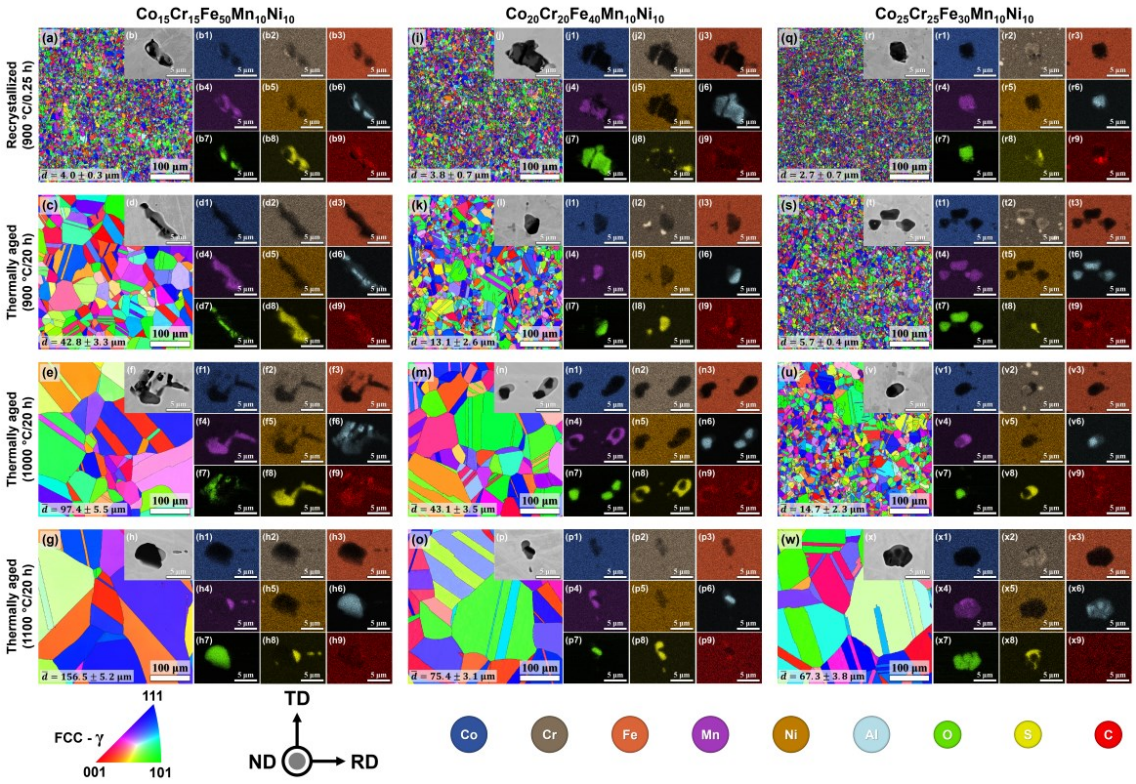

Figure 4.4 - Representative microstructure of M/HEAs (samples recrystallized and thermally aged). EBSD inverse pole figures (IPFs) of (a, c, e, g) Co15Cr15, (I, k, m, o) Co20Cr20, and (q, s, u, w) Co25Cr25 M/HEAs. SEM-BSE images of the typical non-metallic inclusions (NMIs) found in (b, d, f, h) Co15Cr15, (j, l, n, p) Co20Cr20, and (r, t, v, x) Co25Cr25. ((b1-b9), (d1-d9), (f1-f9), (h1-h9), (j1-j9), (l1-l9), (n1-n9), (p1-p9), (r1-r9), (t1-t9), (v1-v9), and (x1-x9)) correspond to EDS mapping of the NMIs shown in (b, d, f, h) Co15Cr15, (j, l, n, p) Co20Cr20, and (r, t, v, x) Co25Cr25, respectively. The mean grain size ($\overline{d}$) of each alloy is also indicated in the IPFs.

To support microstructure characterization, high-energy synchrotron X-ray diffraction (HE-SXRD) was utilized to comprehensively analyze phase structure evolution. The use of 2D detectors and high-penetration (transmission mode) with high-energy photons allowed for the rapid acquisition of complete Debye-Scheler rings, capturing bulk microstructure information in a single beam shot within seconds [116,117].

Integration of the obtained 2D diffraction rings into diffraction patterns is detailed in Fig. 4.5 (a-d), revealing the dominance of an FCC phase with very low traces of NMIs. The high signal-to-noise ratio of synchrotron X-ray sources enabled the identification of even minor phases [118], reinforcing the detection of extremely low-intensity diffraction peaks of the NMIs.

The patterns were indexed to the FCC phase (Ni - ICSD n° 260169 [119]) and NMIs, such as Al-rich oxide (Al_2O_3 - ICSD n° 130948 [120]), (Mn,Cr)-rich oxide ($MnCr_2O_4$ - ICSD n° 33337 [121]), (Mn,Al)-rich oxide ($MnAl_2O_4$ - ICSD n° 157282 [122]), Mn-rich sulfide (MnS ICSD n° 158647 [123]) and $M_{23}C_6$ carbide (ICSD n° 167668 [124]). These findings were consistent with SEM-BSE/EDS examinations, highlighting the presence of NMIs in all samples. It is worth noting that the low-intensity diffraction peaks at specific 2θ positions (dashed line) visible in Fig. 4.5 (a-d) can be attributed to FCC phase reflections caused by the 2^{nd} harmonic of the synchrotron X-ray beam [94–97].

Despite efforts to increase sigma phase formation kinetics by cold-rolling before thermal aging, both SEM-BSE/EDS and HE-SXRD analyses suggested the change in driving force and acceleration of sigma phase formation kinetics may not have been sufficient to induce sigma phase formation in these alloys. Schuh *et al.* [31] suggested the absence of clear experimental evidence of the sigma phase could possibly be attributed to kinetic suppression, rather than thermodynamic stability, implying thermodynamic equilibrium may not have been reached, even after prolonged aging at specific temperatures. However, this possibility seems remote, considering the long time (20 h) the samples were held at a high temperature, 900 °C and above, which corresponds to 68% (and above) of the homologous temperature. Additionally, since the samples

from this work were previously cold worked, it reinforces the idea that these samples should indeed be sigma-free at the temperatures investigated.

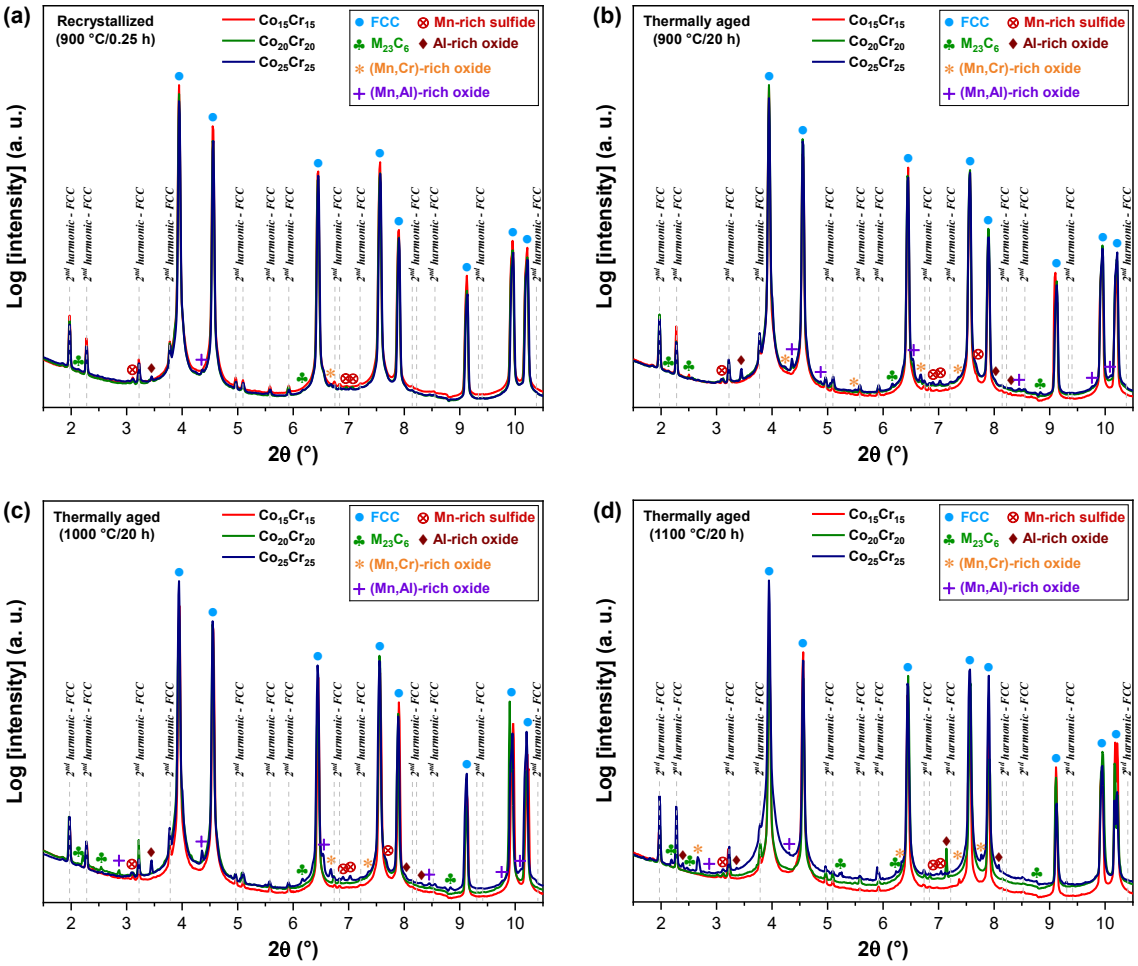

Figure 4.5 - Representative high-energy synchrotron X-ray diffraction patterns (logarithmic intensity scale) of the M/HEAs. (a) recrystallized at 900 °C for 0.25 h, (b) thermally aged at 900 °C for 20 h, (c) thermally aged at 1000 °C for 20 h, and (d) thermally aged at 1100 °C for 20 h. As shown, peaks of the FCC phase were predominantly observed, along with very weak signals corresponding to non-metallic inclusions (NMIs) identified as oxides, sulfides, and carbides. The not indexed low-intensity diffraction peaks (dashed line) correspond to FCC phase reflections caused by the 2nd harmonic of the synchrotron beam. Notably, no indications of the sigma phase were detected.

4.4 Comparative analysis of sigma phase prediction methods/criteria vs experimental data

After presenting and discussing the different aspects of phase prediction methods (CALPHAD and Tsai criteria) and experimental characterization (SEM-BSE/EDS and HE-SXRD analysis), it is possible to compare the predictions and experimental results, as shown in Table 4. When comparing the experimental results with the CALPHAD method, using the TCHEA5 and PanHEA2022 databases, the TCHEA5 database correctly predicted only 1 of the 9 conditions: the Co15Cr15 alloy when thermally aged at 1100 °C for 20 h, resulting in single-phase FCC only. However, it incorrectly predicted sigma formation for all of the other tested conditions. Conversely, PanHEA2022 database correctly predicted 8 of the 9 conditions, wrongly predicting (sigma formation) only for the Co25Cr25 alloy when thermally aged at 900 °C for 20 h. In practice, regardless of the aging temperatures studied, these alloys exhibited only the FCC phase and minority NMIs. The databases are predominantly based on the phase equilibria of binary and, to a lesser extent, ternary systems; an increasing body of evidence shows the fidelity of their predictions in higher order systems, such as M/HEAs, is unreliable [52,105,106,125,126]. Both databases present the f_{AB} = 1. However, whereas the TCHEA5 database presents a f_{AT} = 0.5, the PanHEA2022 database presents a f_{AT} = 0.8, as mentioned previously. When more experimental data on sigma phase stability becomes available, it should be possible to update and/or develop new databases, which should improve the predictability of the CALPHAD method.

Comparative analysis of experimental findings with the Tsai criteria revealed accurate predictions for all alloys, regardless of the temperatures studied. Furthermore, Tsai *et al.* [60] recommended the refinement of their criteria through extensive investigations encompassing different conditions. A noteworthy contribution of this study lies in its exploration of alloys subjected to thermal aging at three distinct temperatures (900, 1000, and 1100 °C), which deviate from the initially reported 700 °C employed to develop the Tsai criteria. The aging time of 20 h, however, was kept the same. It is worth noting that the

Tsai criteria represent an empirical methodology conceived with the primary objective of predicting the sigma phase within V- and Cr-containing M/HEAs. Nevertheless, this method demonstrated a high level of accuracy in predicting sigma-free or sigma-prone alloys in the CoCrFeMnNi system. Although accurate for the alloys studied here, Bertoli *et al.* [22] made comments regarding the most advantageous approach to enhance the predictability of the sigma phase using the Tsai criteria. They considered three potential strategies: one involving a unified VEC range for various alloys and temperatures, which benefits from a large dataset and extensive sampling; another involving specific VEC ranges tailored to each alloy system or temperature range, offering specialization and a well-defined scope; and a third that represents a compromise between the two previous possibilities.

Table 4.3 - Predicted vs experimentally observed phases for the studied M/HEAs compositions. Predictions by the CALPHAD method (at 900 ºC, 1000 ºC and 1100 ºC) and by the Tsai Criteria (Sigma-free - VEC outside 6.88-7.84 *or* PSFE < 25%; sigma-prone - VEC inside 6.88-7.84 *and* PSFE > 40%; and Uncertain - VEC inside 6.88-7.84 *and* PSFE between 25% and 40%). Experimentally observed phases obtained by a combination of scanning electron microscopy (EDS, BSE and EBSD) and high-energy synchrotron X-ray diffraction in the thermal aging condition (at 900 ºC, 1000 ºC and 1100 ºC for 20 h).

Alloys	Temperature (ºC)	CALPHAD method		Tsai criteria	Experimental
		TCHEA5 database	PanHEA2022 database	VEC | PSFE | Sigma-?	SEM and HE-SXRD
Co15Cr15	1100	FCC	FCC	7.95 | 30% | Sigma-free	FCC
	1000	FCC + 4% sigma	FCC		FCC
	900	FCC + 15% sigma	FCC		FCC
Co20Cr20	1100	FCC + 8% sigma	FCC	7.90 | 40% | Sigma-free	FCC
	1000	FCC + 20% sigma	FCC		FCC
	900	FCC + 30% sigma	FCC		FCC
Co25Cr25	1100	FCC + 10% sigma	FCC	7.85 | 50% | Sigma-free	FCC
	1000	FCC + 22% sigma	FCC		FCC
	900	FCC + 32% sigma	FCC + 2% sigma		FCC

Note: For all thermodynamic calculations using the CALPHAD method, Thermo-Calc® software using TCHEA5 database, and Pandat® software using PanHEA2022 database were used under equilibrium conditions. The data were plotted using nominal, rather than actual, alloy compositions. Although the FCC phase was predominantly observed through SEM and HE-SXRD experiments, the presence of non-metallic inclusions (NMIs), identified as oxides, sulfide, and carbides, was also detected at extremely low levels.

4.5 Recrystallization, grain growth and mechanical properties

SEM-EBSD inverse pole figures (IPFs) of the recrystallized M/HEAs are shown in Fig. 4.6-4.8 for Co15Cr15, Co20Cr20 and Co25Cr25, respectively. The IPF maps revealed that in all the annealing conditions, microstructures were fully recrystallized with significant fractions of annealing twins and showed random orientation. All samples present single-phase FCC. Furthermore, all micrographs exhibited a uniform grain size distribution. The temperature and time are proportional to the grain size. In addition, higher temperatures result in a more rapid grain growth compared to lower temperatures. Notably, the Co15Cr15 exhibits a pronounced tendency for faster grain growth than Co20Cr20 and Co25Cr25 alloys. The smallest grain sizes, measuring 4.0 μm (Co15Cr15), 3.8 μm (Co20Cr20), and 2.7 μm (Co25Cr25), were achieved through annealing at 900 °C for 0.25 h. Conversely, the largest grain sizes, measuring 102.5 μm (Co15Cr15), 77.7 μm (Co20Cr20), and 40.5 μm (Co25Cr25), were obtained by annealing at 1100 °C for 2 h.

Recent studies suggest that stacking fault energy (SFE) plays a role in controlling kinetic processes, such as rate of recovery, recrystallization, and grain growth [127]. Thirathipviwat *et al.* [128] confirmed that lower SFE led to partial dislocations that were difficult to climb and cross-slip, resulting in a lower grain growth rate for the CoCrFeMnNi HEA. In opposite, higher SFE in a FeNiCo alloy and in pure Ni showed easy climb and cross-slip, which provided faster recovery, extensive recrystallization, and grain growth. However, that the movement of dislocations is unrelated to diffusive processes rules out the possibility that the changes in recrystallization and grain growth are due to SFE, reinforcing the need for an alternative explanation.

It is known that Co and Cr additions decrease the SFE, which facilitates the occurrence of strain-induced HCP martensitic phase (TRIP effect) [13,14,32,129]. The alloys studied here present the following deformation mechanisms: Co15Cr15 (TWIP), Co20Cr20 (TWIP/TRIP), and Co25Cr25 (TRIP). The results to prove it are further described later. Thus, the nucleation of a second phase (strain-induced HCP martensitic phase) in the FCC matrix

after the cold rolling aggravates heterogeneous deformation. Hence, the effect of second phase increases stored energy during deformation, leading to significant misorientation and leaving numerous crystal defects, e.g. dislocations and stacking faults (SFs), providing more nucleation sites for recrystallization, leading to reduced grain growth [130–132].

Recently, Puosso *et al.* [133] and Bertoli *et al.* [73] evaluated the Hall-Petch and grain growth kinetics of CrCoNi alloys. While Puosso *et al.* [133] focused on the $Cr_{40}Co_{30}Ni_{30}$ alloy (TWIP dominant), Bertoli *et al.* [73] focused on the $Cr_{40}Co_{40}Ni_{20}$ alloy (TRIP dominant). Both studies strictly followed the same thermomechanical processing conditions (cold rolling to a thickness reduction of 40%), as well as annealing temperature and time. For all annealing conditions, the TWIP $Cr_{40}Co_{30}Ni_{30}$ alloy exhibited larger grain sizes when compared to the TRIP $Cr_{40}Co_{40}Ni_{20}$ alloy. It even surpassed twice the grain size when both were annealed at 900 °C for 0.5 h, measuring 8.4 μm ($Cr_{40}Co_{30}Ni_{30}$) compared to 4.1 μm ($Cr_{40}Co_{40}Ni_{20}$). Wei *et al.* [13] designed novel FCC phase non-equiatomic CoCrMnNiFe HEAs with different SFEs via modifying constituent concentrations. The same trend was observed, i.e., increasing Co and/or Cr content at the expense of Fe, Mn, and Ni, in addition to reducing the SFE value, decreased the mean grain size of the alloys ($Co_{20}Cr_{20}Mn_{20}Ni_{20}Fe_{20}$, Cantor alloy – TWIP dominant (19.8 μm), $Co_{35}Cr_{20}Mn_{15}Ni_{15}Fe_{15}$, TWIP dominant (16.3 μm), and $Co_{35}Cr_{25}Mn_{15}Ni_{15}Fe_{10}$, TRIP dominant (11.2 μm)). The alloys were cold-rolled to a thickness reduction of 40%, then annealed at 1000 °C for 0.1 h.

It is also worth noting that, during the grain growth stage of annealing, the average grain size is normally proportional to the square root of the product of diffusivity and time [134]. The larger grain size hence results from the higher diffusion rates of the alloy elements. This suggests the Co15Cr15 alloy with the largest grain size has relatively high diffusion rate compared with the Co20Cr20 and Co25Cr25 M/HEAs.

Hence, we believe that, although tuning the compositions led to a reduction in the SFE, it was not this parameter that was responsible for the increased recrystallization rate, resulting in a lower grain growth rate, but rather

the effect of the second phase (strain-induced HCP martensitic phase), as well as different diffusion rates, where we expect the latter to increase in the following order: Co25Cr25 < Co20Cr20 < Co15Cr15. However, a detailed analysis is beyond the scope of this study. Therefore, further research is necessary to understand the detailed mechanism of recrystallization and grain growth behavior of these alloys.

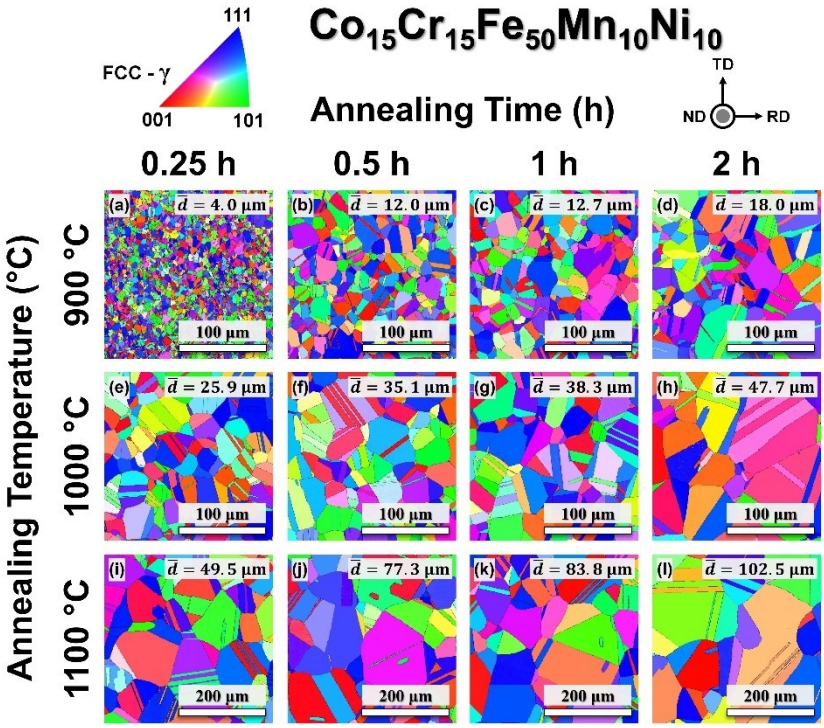

Figure 4.6 - Microstructure of the recrystallized M/HEAs. EBSD IPFs of Co15Cr15 alloy. The mean grain size ($\overline{d}$) of each alloy is also indicated in each IPF.

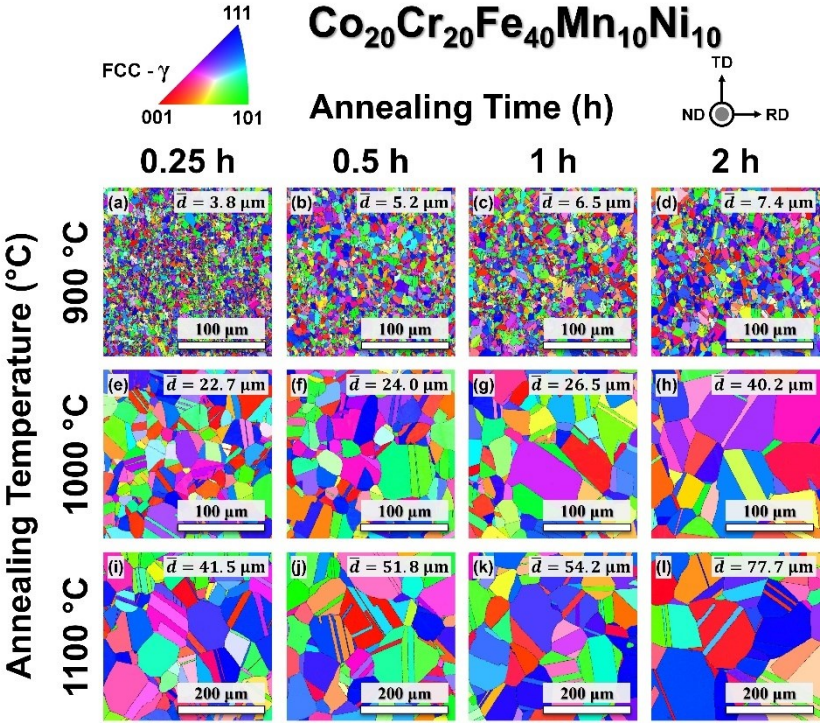

Figure 4.7 - Microstructure of the recrystallized M/HEAs. EBSD IPFs of Co20Cr20 alloy. The mean grain size ($\overline{d}$) of each alloy is also indicated in each IPF.

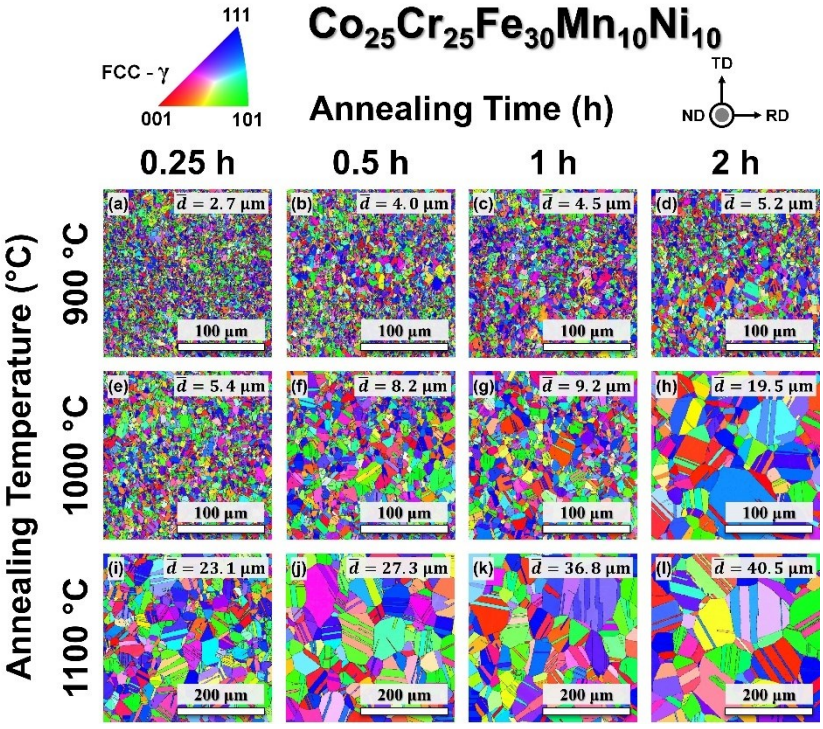

Figure 4.8 - Microstructure of the recrystallized M/HEAs. EBSD IPFs of Co25Cr25 alloy. The mean grain size ($\overline{d}$) of each alloy is also indicated in each IPF.

To demonstrate the mechanical performance of the M/HEAs and elucidate the influence of grain size, tensile tests were conducted at room temperature. Figure 4.9 (a-c, d-f, g-i) illustrates the representative engineering stress-strain curves for Co15Cr15, Co20Cr20, and Co25Cr25 M/HEAs, respectively. The corresponding strength and elongation values are summarized in the inserted table. As expected, both the yield strength (σ_y), determined as the stress at which 0.2% plastic strain occurs, and ultimate tensile strength (σ_u) decreased with an increase in grain size, but increased with higher Co and Cr contents. This suggests an enhancement in solid solution strengthening as the Co and Cr (mainly Cr) contents increase [135].

Regarding ductility (uniform and total elongation), we need to consider the effect of grain size on the stability of deformation mechanisms (TWIP and/or TRIP) in these alloys. The FCC grain size also plays a crucial role in these deformation mechanisms, leading to an increase in the SFE value due to grain refinement. The SFE including the grain size effect is called 'apparent' SFE, distinguished from 'intrinsic' SFE based upon the chemical composition of an alloy and temperature [136,137]. The effect of FCC grain size on the transition of deformation mechanisms (TRIP↔TWIP) has been extensively examined in several works inspired by medium- and high-Mn steels [138–140]. Jo *et al.* [141] reported that whereas only mechanical twins were observed in a tensile-fractured Fe–18Mn-0.6C-1.5Si (wt.%) TWIP steel with grain sizes smaller than 17.6 μm, strain-induced martensitic phase was observed in a sample with grain sizes above 20.3 μm. A study conducted by Lee *et al.* [142] concluded that when the FCC grain size decreased from 51.72 μm to 0.75 μm in a Fe–17Mn (wt.%) steel, the apparent SFE value increased from 10.8 mJ/m^2 to 23.4 mJ/m^2, and the transition from TRIP to TWIP occurred at the late stage of tensile strain in ultrafine-grained specimens with high apparent SFE values (>23.1 mJ/m^2). Experimentally, the SFE can be obtained using TEM analysis by measuring the distance between Shockley partial dislocations. In this analysis, several factors, including nearby grain boundaries, can limit the distance of the partials [143], which is reflected in the increase in the apparent SFE values.

Although not shown here, we believe that as grain size increases, it influences the stability of the FCC matrix, leading to a decrease in the apparent SFE, which may lead to a transition from TWIP to TRIP mechanisms. However, even though the grain sizes studied here may not provide sufficient driving force to lead to a transition of deformation mechanism, larger grain sizes facilitate an increase in the content of strain-induced HCP martensitic phase. This effect is particularly notable in alloys already exhibiting the TRIP effect at smaller grain sizes, thereby reinforcing the dominance of the TRIP effect as grain size increases. While several studies were conducted to investigate the TRIP↔TWIP transition, the optimal contribution of each of these mechanisms remains unclear. However, a detailed analysis of this is beyond the scope of this work. Future work should consider these data, as these deformation mechanisms have a direct impact on the mechanical properties.

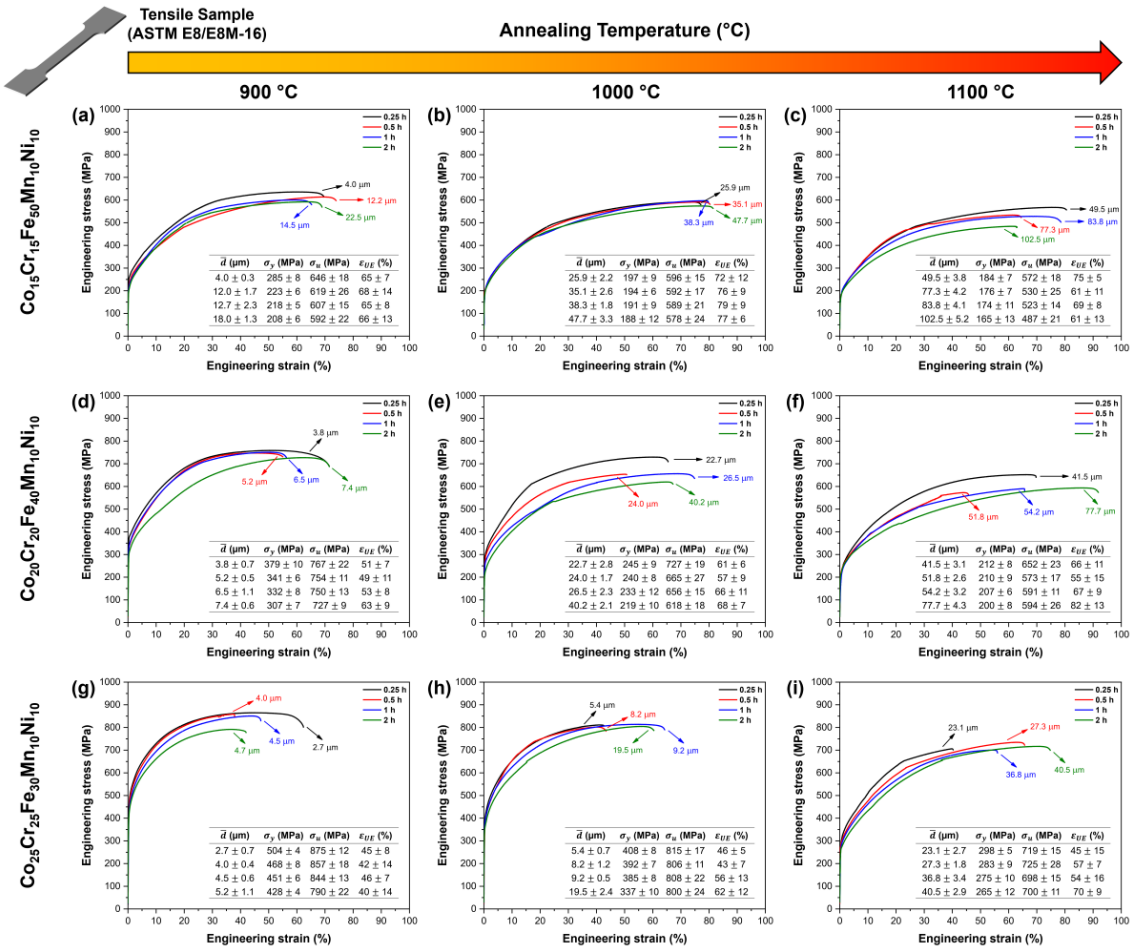

Figure 4.9 – Engineering stress-strain curves at room temperature of the recrystallized M/HEAs with different grain sizes. (a, b, c) Co15Cr15, (d, e, f) Co20Cr20, (g, h, i) Co25Cr25 M/HEAs annealed at 900, 1000 and 1100 °C for 0.25, 0.5, 1 and 2 h, respectively. The inserts in (a-i) summarize the mechanical properties of the alloys determined from tensile tests. σ_y, σ_u, and ε_{UE} refer to yield strength, ultimate tensile strength, and uniform elongation, respectively. σ_y was determined as the stress at which 0.2% plastic strain occurs.

As shown by the tensile properties (Fig. 4.9), the mechanical behavior of M/HEAs is strongly affected by grain size. The relation between yield strength (σ_y) and mean grain size (d) is given by the classical Hall–Petch equation [144,145]:

$$\sigma_y = \sigma_0 + k_{HP} d^{-1/2} \tag{4.1}$$

Where, σ_0 is the intrinsic resistance of the lattice to dislocation motion referred to as friction stress, and k_{HP} can be interpreted as the resistance offered by grain boundaries to the dislocation slip [146].

Fig. 4.10 shows the Hall-Petch plots for yield strength (0.2% proof stress, $\sigma_{0.2\%}$) versus inverse square root of the mean grain size ($d^{-1/2}$) of the M/HEAs at room temperature. It is observed that, within the current grain size range, the σ_y values follow the classical Hall-Petch relationship. The relationships for each alloy were determined by fitting the data using Eq. (4.1), with the respective equations presented in Fig. 4.10. The values of σ_0 are 144, 147, and 198 MPa for the Co15Cr15, Co20Cr20, and Co25Cr25 M/HEAs, respectively, as determined from the linear fittings (R^2 = 0.98-0.99). Although the difference in σ_0 is insignificant between Co15Cr15 and Co20Cr20 (≈ 2%), when compared with Co25Cr25, it was improved by 36%. The σ_0 of the M/HEAs was much larger than those of pure Ni (14.2 MPa), pure Al (4.0 MPa), and Ni-40Co alloy (51.9 MPa) [147]. Local lattice distortion (LLD) and chemical undulation, or short-range order (SRO), were shown to increase the lattice friction force of M/HEAs [148–151]. On the other hand, k_{HP} increased significantly from 275 to 516 MPa.μm$^{1/2}$, representing an approximately 88% increase when comparing Co15Cr15 and Co25Cr25 alloys. A high k_{HP} denotes that the (yield) strength considerably increases with the decreasing grain size. The k_{HP} of Co25Cr25 (516 MPa.μm$^{1/2}$) is comparable to the equiatomic CrCoNi and non-equiatomic $Cr_{40}Co_{40}Ni_{20}$ alloys [73], and much greater than commercial Cr–Ni austenitic stainless steels (395 MPa.μm$^{1/2}$) [152] and pure FCC metals (80–230 MPa.μm$^{1/2}$) [153].

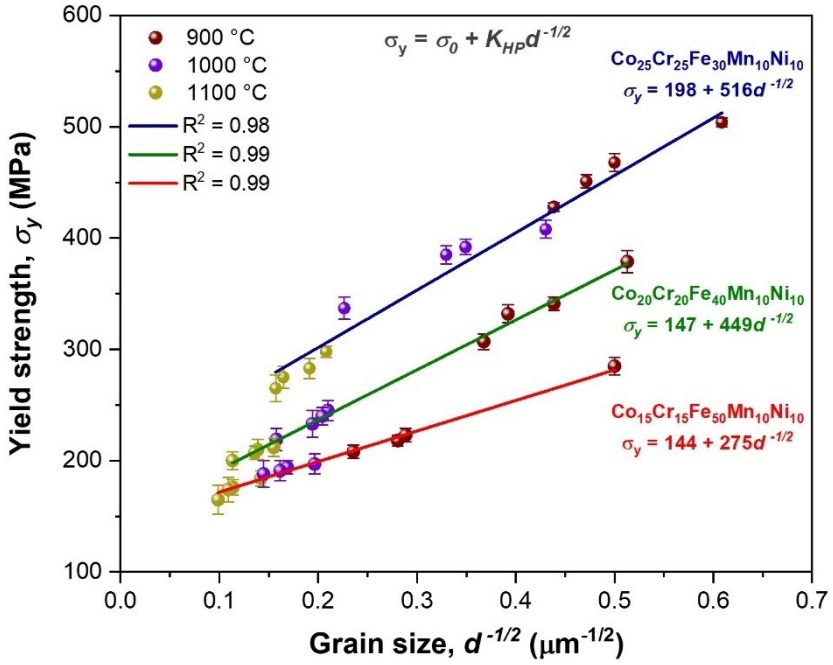

Figure 4.10 – Hall–Petch plot of the yield strength (σ_y) as a function of the mean FCC grain size ($d^{-1/2}$), excluding twin boundaries, of the M/HEAs.

The Hall-Petch slope, k_{HP}, can be fitted by the empirical Eq. (4.2) [153]:

$$K_{HP} = \beta G b^{1/2} \tag{4.2}$$

where, G is the shear modulus, b is the magnitude of the Burgers vector, and β is a model-dependent constant. For FCC alloys, β = 0.18 is accurate [153], thus it was used in this work.

The shear moduli (G) were calculated by extrapolating them to what would be expected from pure single-phase FCC Cr, Mn, Fe, and Co. Thus, the G values for each composition were calculated using Eq. (4.3) [135].

$$G = 103.5x_{Cr} + 81.0x_{Mn} + 51.7x_{Fe} + 81.0x_{Co} + 76.0x_{Ni} \tag{4.3}$$

The atomic radii (r) of the elements obtained by Coury et al. [135], calculated through the effective atomic radii for strength (EARS) methodology are: Cr (130.09 pm), Mn (129.41 pm), Fe (127.86 pm), Co (124.30 pm) and Ni (122.66 pm). This would be the atomic radius that these elements would present in an equiatomic CrMnFeCoNi alloy with an FCC structure.

Fig. 4.11 (a) shows the predicted K_{HP} values, in which pseudo-ternary phase diagram (in at.%) for the Fe-$Cr_{50}Co_{50}$-$Ni_{50}Mn_{50}$ system is presented. As can be seen, as the Co and Cr contents increase, in addition to the expected

reduction in SFE, there is also an increase in K_{HP}. Thus, indicating an inverse relationship, i.e., SFE^{-1} $\propto K_{HP}$. The shear modulus (G), increased from 69.2 GPa (Co15Cr15) to 73.3 GPa (Co20Cr20) and then to 77.3 GPa (Co25Cr25). As k_{HP} are proportional to G, an increase in G contributes to an increase in this parameter. Simultaneously, SFE affects the dislocation-slip behavior and the arrangement of dislocations, which is another reason for the differences in k_{HP}. According to Wei *et al.* [147], the restriction of Shockley partials is a prerequisite for cross-slip, which is suppressed by reducing SFE. Consequently, a larger shear stress is required for dislocation pile-ups to reach critical stress concentration. Thus, a decrease in SFE further contributes to the increase in k_{HP}. This behavior was also reported in other studies [73,133,154].

In order to predict the solid solution strengthening (σ_{ss}), the Varvenne model [151] (Eq. 4.4) was employed and plotted over the pseudo-ternary diagram (in at.%) for the Fe-$Cr_{50}Co_{50}$-$Ni_{50}Mn_{50}$ system. This model has proven to be accurate in FCC alloys of the CrMnFeCoNi system [135,155]. According to the model, the Peierls stress at 0 K (τ_0) and the activation energy for moving a dislocation (ΔE_b) are calculated by Eqs. (4.5 and 4.6), respectively.

$$\sigma_{ss}(T,\dot{\varepsilon}) = M\tau_0 \left[1 - \left(\frac{k_b T}{\Delta E_b} ln\frac{\dot{\varepsilon}_0}{\dot{\varepsilon}}\right)^{\frac{2}{3}}\right] \tag{4.4}$$

$$\tau_0 = 0.051\alpha^{-\frac{1}{3}} G \left(\frac{1+\nu}{1-\nu}\right)^{\frac{4}{3}} f_1(w_c) \left[\sum_n \frac{x_n \Delta\bar{V}_n^2}{b^6}\right]^{\frac{2}{3}} \tag{4.5}$$

$$\Delta E_b = 0.274\alpha^{\frac{1}{3}} G b^3 \left(\frac{1+\nu}{1-\nu}\right)^{\frac{2}{3}} f_2(w_c) \left[\sum_n \frac{x_n \Delta\bar{V}_n^2}{b^6}\right]^{\frac{1}{3}} \tag{4.6}$$

where M is the Taylor factor, which is used as 3.06 for FCC crystals, k_b is the Boltzmann constant, $\dot{\varepsilon}_0$ is a reference strain rate set at 10^{-4} s^{-1} [151]. The calculations were performed considering a temperature (T) of 293 K and a strain rate ($\dot{\varepsilon}$) of 10^{-3} s^{-1}, in accordance with the conducted tensile tests. The parameter α is a dimensionless constant related to the dislocation line tension, which is considered as 0.123 [156]. b is the dislocation Burgers vector length, G is the alloy shear modulus (Eq. (4.3)). The $f_1(w_c)$ and $f_2(w_c)$ terms are numerical coefficients related to dislocation core structures, nearly constant at 0.35 and 5.70, respectively [157]. The x_n term is the concentration of the nth

element in the alloy. The $\Delta\bar{V}_n$ term is the average misfit volume caused by the nth element in the solid solution. The atomic volume is calculated from the atomic radii. ν is the alloy Poisson ratio, calculated through Eq. (4.7) [135].

$$\nu = 0.275x_{Cr} + 0.056x_{Mn} + 0.353x_{Fe} + 0.293x_{Co} + 0.310x_{Ni} \quad (4.7)$$

The σ_{ss} calculated by Eq. (4.4) dominates at high stresses (when $\sigma_{ss}/\, M\tau_0 > 0.4$). However, at lower stresses (when $\sigma_{ss}/\, M\tau_0 \leq 0.4$), the σ_{ss} was recalculated using Eq. (4.8) [151].

$$\sigma_{SS}(T, \dot{\varepsilon}) = M\tau_0\, exp\left(-\frac{1}{0.51}\frac{k_bT}{\Delta E_b} ln\frac{\dot{\varepsilon}_0}{\dot{\varepsilon}}\right) \qquad if\ \frac{\sigma_{SS}}{M\tau_0} \leq 0.4 \quad (4.8)$$

The predicted σ_{ss} values calculated using Varvenne-EARS method [135], plotted over the pseudo-ternary diagram (in at.%) for the Fe-$Cr_{50}Co_{50}$-$Ni_{50}Mn_{50}$ system, are shown in Fig. 4.12 (b). The σ_{ss} grows towards Co and Cr-rich alloys (96, 119, and 144 MPa for Co15Cr15, Co20Cr20, and Co25Cr25 M/HEAs, respectively). However, unlike the trend observed in Fig. 4.12 (a), where the increase in K_{HP} grows towards Co-Cr binary alloy, σ_{ss} does not follow the same direction, as shown in Fig. 4.12 (b). This may be attributed to lattice distortion. In previous studies, Coury *et al.* [135] utilized high-throughput calculations to demonstrate that introducing Mn while removing Ni and Co in the CoCrFeMnNi system increases lattice distortion. This effect is attributed to the approach to a 50% ratio of large to small atoms, as Mn is larger than both Co and Ni but smaller than Cr. Conversely, Fe, being smaller than Mn, exhibits a similar effect at reduced magnitude. For this reason, elevated σ_{ss} values are observed near the composition of the $Co_{30}Cr_{30}Mn_{20}Ni_{20}$ alloy, see Fig. 4.12 (b). It is worth noting that the higher predicted σ_{ss} value found for $Co_{30}Cr_{30}Mn_{20}Ni_{20}$ is due to the constraints used to plot the pseudo-ternary diagram, i.e., Fe-$Cr_{50}Co_{50}$-$Ni_{50}Mn_{50}$ system. This indicates that $Co_{30}Cr_{30}Mn_{20}Ni_{20}$ alloy is not necessarily the one with the highest predicted σ_{ss} value in the Cantor system.

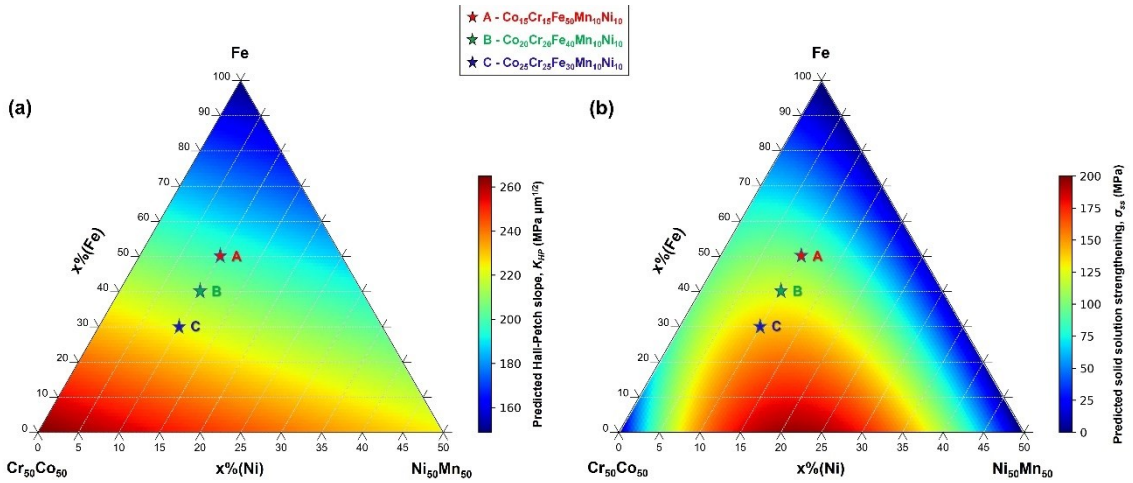

Figure 4.11 – (a) Predicted Hall-Petch slope (k_{HP}) plotted over the pseudo-ternary diagram (in at.%) for the Fe-$Cr_{50}Co_{50}$-$Ni_{50}Mn_{50}$ system. (b) Predicted solid solution strengthening (σ_{ss}) determined by the Varvenne-EARS method, plotted over the same compositional space.

Samples annealed at 900 °C for 0.25 h were employed for a comprehensive investigation into the microstructure-mechanical properties relationship. Fig. 4.12 (a) shows the engineering tensile stress-strain curves of the M/HEAs at room temperature. The σ_y and σ_u of the Co25Cr25 were improved by 77% and 35%, respectively, meanwhile the ε_{UE} decreased ≈ 31%, compared with Co15Cr15 alloy. To identify the optimal strength-ductility synergy, the product of yield strength and uniform elongation ($\sigma_y.\varepsilon_{UE}$), also referred to as tension toughness [53,158], was plotted against the yield strength (Fig. 4.12 (b)). As shown, the $\sigma_y.\varepsilon_{UE}$ is proportional to the σ_y. In addition, the Co15Cr15 exhibits the lowest product (18.5 GPa%), suggesting a poor balance of strength and ductility. With increasing Co and Cr contents, the $\sigma_y.\varepsilon_{UE}$ increases, and the optimal strength toughness is achieved for the Co25Cr25 (22.6 GPa%). This confirms that the Co25Cr25 indeed enables the optimal balance of yield strength and uniform elongation.

The σ_y of a polycrystalline alloy can be described as the sum of multiple strengthening contributions, as shown in Eq. (4.9):

$$\sigma_y = \sigma_{\rho i} + \sigma_{ss} + \sigma_{gb} + \sigma_{pp} \quad (4.9)$$

where, $\sigma_{\rho i}$, σ_{ss}, σ_{gb} and σ_{pp} are the initial dislocation density, solid solution, grain boundaries, and precipitation hardening contributions to the yield strength, respectively. Given that the alloys are fully recrystallized single-phase FCC, the σ_{pp} term can be disregarded.

The hardening effect of grain boundaries (σ_{gb}) is inversely related to the grain size by the Hall-Petch relationship:

$$\sigma_{gb} = k_{HP}/\sqrt{d} \quad (4.10)$$

where, k_{HP} is the Hall-Petch slope (275, 449 and 516 MPa.μm$^{1/2}$ for the Co15Cr15, Co20Cr20, and Co25Cr25 M/HEAs, respectively) and d is the mean grain size (4.0 μm for Co15Cr15, 3.8 μm for Co20Cr20, and 2.7 μm for Co25Cr25). Thus, stresses of 138, 230, and 314 MPa were obtained for the Co15Cr15, Co20Cr20, and Co25Cr25 M/HEAs, respectively, due to the contribution of grain boundaries (σ_{gb}). It should be noted that the Hall-Petch slope (k) values used to determine the hardening contribution of grain boundaries were those determined experimentally, see Fig. 4.10. Based on this result, the hardening effect of grain boundaries corresponds to about 48% for Co15Cr15, 61% for Co20Cr20 and 62% for Co25Cr25 of the yield strength. Furthermore, the smaller the grain size, the greater this effect (σ_{gb}).

The strengthening contribution from dislocations can be estimated according to Eq. 11 [159].

$$\sigma_{\rho i} = M\alpha Gb\rho i^{1/2} \quad (4.11)$$

where, M is the Taylor factor and its value is 3.06, α is a scaling factor and a value of 0.23 was used [160], G is the shear modulus (calculated using Eq. (4.3)), b is the magnitude of the Burgers vector, and ρi is the initial dislocation density (calculated using Eq. (3.5)). The $\sigma_{\rho i}$ contributed ≈ 110, 138, and 133 MPa for the Co15Cr15, Co20Cr20, and Co25Cr25 M/HEAs, respectively, calculated from the initial dislocation density of 7.9 x 10^{13} m^{-2} for Co15Cr15, 11.1 x 10^{13} m^{-2} for Co20Cr20, and 9.3 x 10^{13} m^{-2} μm for Co25Cr25. However, in terms of the dislocation strengthening ($\sigma_{\rho i}$), the difference is insignificant between the alloys. The predicted σ_y values from the sum of multiple strengthening contributions ($\sigma_{\rho i} + \sigma_{ss} + \sigma_{gb}$) were 344, 487, and 591

MPa for the Co15Cr15, Co20Cr20, and Co25Cr25 M/HEAs, respectively. Although the theoretically predicted σ_y values differ slightly from the experimentally calculated σ_y (0.2% proof stress) values (285, 379, and 504 MPa for Co15Cr15, Co20Cr20, and Co25Cr25 M/HEAs, respectively, as shown in Fig. 4.12 (a)), the same trend was observed. It could be concluded that, although the difference between σ_{ss} and σ_{gb} is insignificant for Co15Cr15, the net increment in σ_y was predominantly due to σ_{gb} for the Co20Cr20 and Co25Cr25 alloys.

Fig. 4.12 (c) shows the true stress-strain curves and strain-hardening curves of the M/HEAs. The alloys exhibit extensive work hardening. The curves indicate that, initially, up to approximately 5% true strain, there is a rapid decline. From 5% to around 35-45%, a plateau appears, attributed to the activation of deformation mechanisms (TWIP and/or TRIP). These mechanisms act as barriers to dislocation movements, delaying the point of plastic instability and enhancing plasticity [8,10,77,161]. As the necking point is approached, the work hardening rate decreases again. The Co25Cr25 alloy displays a higher and faster-decreasing strain-hardening rate compared to Co15Cr15, while the Co20Cr20 alloy exhibits an intermediate condition. This observation suggests differences in the induced plasticity mechanisms (TWIP and/or TRIP).

Although both TWIP and TRIP alloys display similar three stages in work hardening rates, TRIP alloys hinge on the transformation from FCC to HCP as the predominant deformation mechanism, leading to a pronounced work hardening rate. Moreover, the regime where the work hardening rate remains relatively constant corresponds to an increasing presence of the HCP phase with growing plastic strain [129]. In contrast, for TWIP alloys, the increased work hardening rate is attributed to the formation of twins during deformation. These mechanical twins may operate similarly to grain boundaries, with their fraction increasing with strain, resulting in enhanced strength through a dynamic grain refinement (Hall-Petch effect) [162–164].

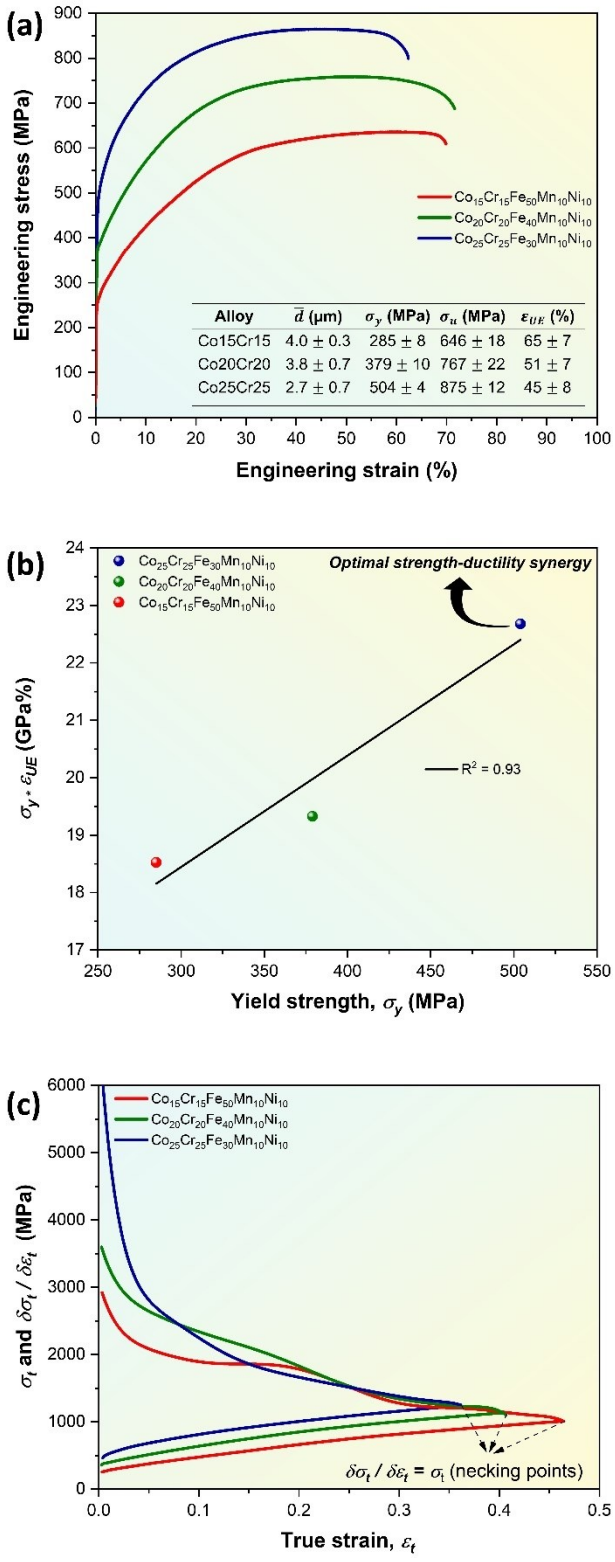

Figure 4.12 – (a) Representative engineering stress-strain curves at room temperature of the recrystallized M/HEAs (samples annealed at 900 °C for 0.25 h). (b) Product of strength and ductility ($\sigma_y.\varepsilon_{UE}$) against σ_y. (c) True stress-strain curves calculated from the engineering stress-strain curves.

Fig. 4.13 (a, b) presents the HE-SXRD patterns of the M/HEAs before and after tension, respectively. All the alloys exhibit a single-phase FCC structure before tension; however, while the Co15Cr15 remained single-phase FCC after tension, the HCP phase was observed in the Co20Cr20 (3%) and Co25Cr25 (18%) alloys after tension, indicating that the FCC→HCP phase transformation occurred during plastic deformation.

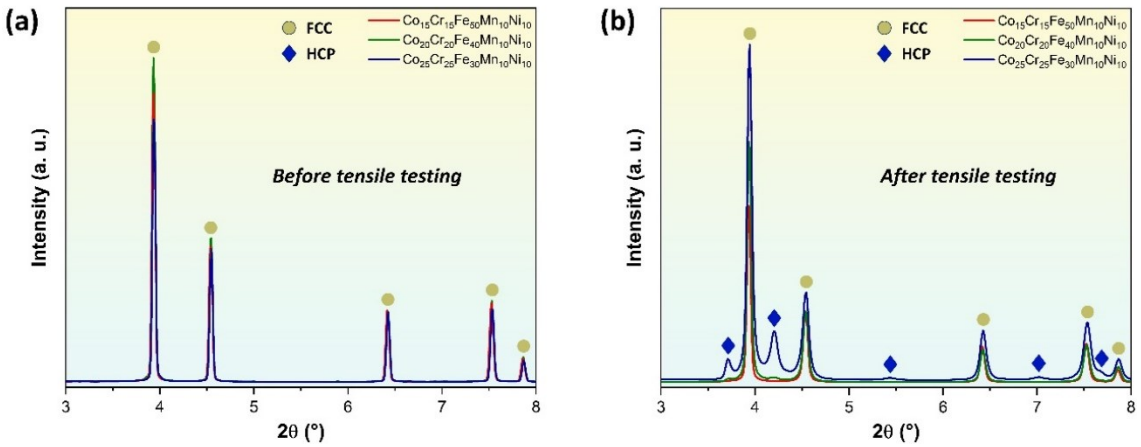

Figure 4.13 – HE-SXRD pattern (a) before and (b) after tensile testing.

Fig. 4.14 (a1,a2; c1,c2; e1,e2) shows the EBSD image quality (IQ) and phase maps of the Co15Cr15, Co20Cr20, and Co25Cr25 M/HEAs, respectively, after tension. The FCC→HCP martensitic transformation is obviously visible in the Co20Cr20 and Co25Cr25 alloys, with area fractions of the HCP phase being 6% and 40%, respectively. However, the Co15Cr15 remained single-phase FCC after tension. This further confirms that the area fraction of HCP-martensite phase gradually increases as the Co and Cr contents increase. It is important to mention that, with its limited spatial resolution, the EBSD analysis only captures a small surface area of the sample, with penetration depths in the order of nanometers [165]. In contrast, HE-SXRD analysis, with the use of 2D detectors and high penetration (transmission mode), provides more reliable data, capturing bulk microstructure information in a single beam shot within seconds [116,117]. This explains the slight difference in the phase fractions (FCC/HCP) obtained by HE-SXRD and EBSD. Both post-mortem analyses were carried out within the gauge length of tensile samples (uniform

deformation zone), but relatively near the fractured region. Thus, it is important to note that, in addition to enhancing contributions ($\sigma_{\rho i}$, σ_{ss}, and σ_{gb}), the TRIP effect likely also played a role in the high work hardening rate of the Co20Cr20, and more even so in the case of the Co25Cr25 alloy.

Further EDS elemental mapping taken across multiple grain boundaries (before tension) confirms that all the elements exhibit excellent elemental homogeneity (Fig. 4.14 (b1-b5) Co15Cr15, Fig. 4.14 (d1-d5) Co20Cr20, and Fig. 4.14 (f1-f5) Co25Cr25). The actual compositions deviate only slightly from the designed compositions ($Co_{14.7}Cr_{14.4}Fe_{49.5}Mn_{11.5}Ni_{9.9}$, $Co_{19.8}Cr_{19.5}Fe_{39.2}Mn_{11.4}Ni_{10.1}$, and $Co_{23.4}Cr_{23.6}Fe_{32.1}Mn_{11.1}Ni_{9.8}$, in at.%).

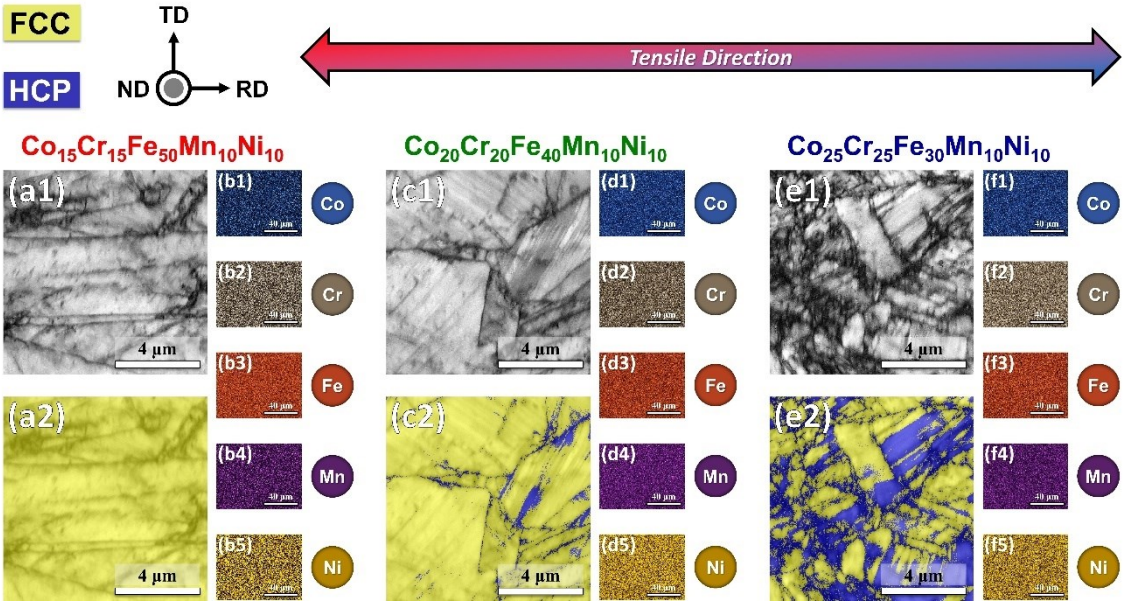

Figure 4.14 – (a1,a2; c1,c2; e1,e2) EBSD image quality (IQ) and phase maps of the Co15Cr15, Co20Cr20 and Co25Cr25 M/HEAs, respectively. (b1-b5, d1-d5, f1-f5) EDS maps of the Co15Cr15, Co20Cr20 and Co25Cr25 M/HEAs, respectively.

To clearly identify the transformed HCP-martensite and deformation twin, TEM analyses were conducted. Fig. 4.15 (a1-a3, b1-b3, c1-c3) shows TEM analysis, including bright field (BF), dark field (DF), and selected area electron diffraction (SAED) patterns of the Co15Cr15, Co20Cr20, and Co25Cr25 M/HEAs, respectively.

In the Co15Cr15 (Fig. 4.15 (a1-a3)), deformation twins actively formed inside an FCC grain without the formation of HCP-martensite, indicating that this alloy presents the TWIP effect as the dominant deformation mechanism. Although, the HCP-martensite phase was detected by HE-SXRD and EBSD in the Co20Cr20 (Fig. 4.15 (b1-b3)), due to its low fraction, as well as TEM sample size limitation, only deformation twins were seen. This indicates that both twins and the HCP-martensite phase are formed during the deformation process, confirming that the Co20Cr20 exhibit both TWIP and TRIP effects. In contrast, in the Co25Cr25, several lamellae with nanometric thickness were observed in the BF and DF images (Fig. 4.15 (c1, c2), identified as HCP-martensite phase in an FCC matrix, according to the SAED pattern (Fig. 4.15 (c3)). The strain-induced HCP phase and FCC matrix follow an orientation relationship of $\{111\}_{FCC}//(0001)_{HCP}$, $<110>_{FCC}//[2\bar{1}\bar{1}0]_{HCP}$, which is in accordance with that reported for other FCC-phase TRIP M/HEAs [147].

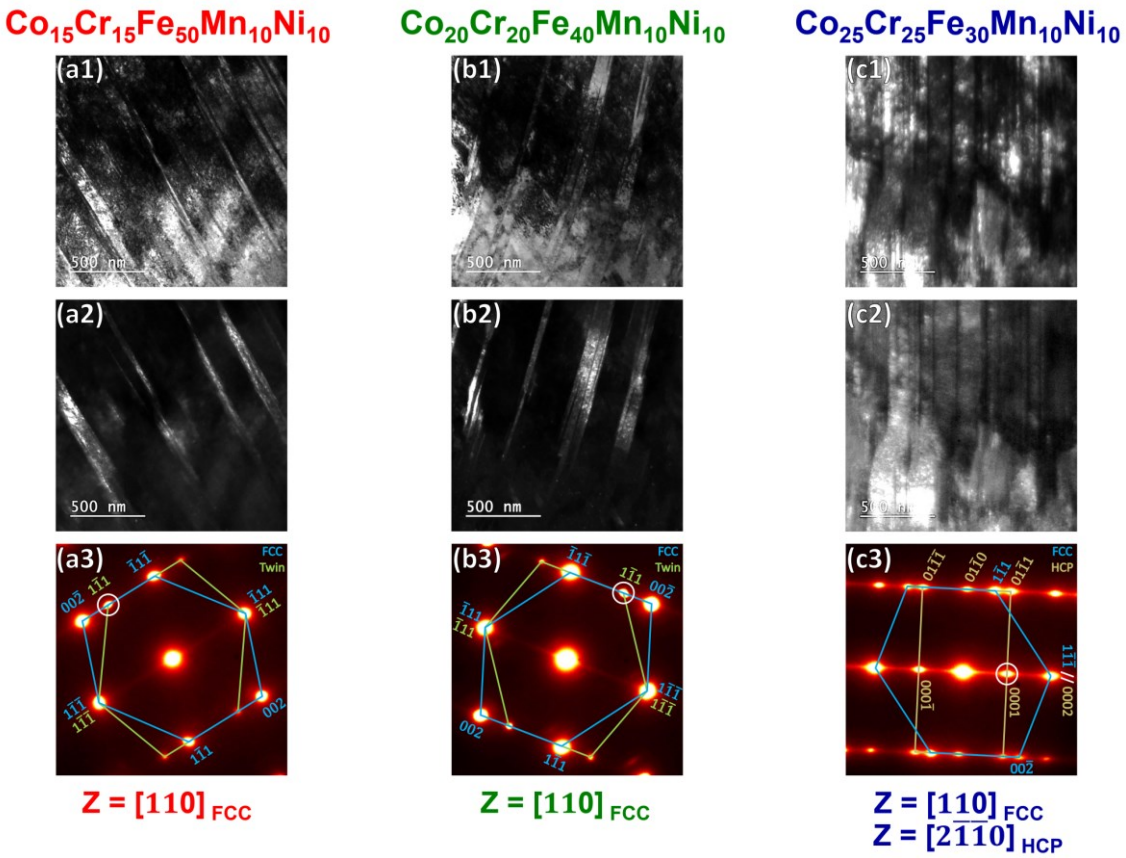

Figure 4.15 – (a1-a3, b1-b3, c1-c3) TEM analysis (bright field (BF), dark field (DF) and selected area electron diffraction (SAED) patterns of the Co15Cr15, Co20Cr20 and Co25Cr25 M/HEAs, respectively. The DF images were acquired using the $\{1\bar{1}1\}_{FCC}$ reflection for the Co15Cr15 and Co20Cr20 M/HEAs and $\{0001\}_{HCP}$ reflection for the Co25Cr25 HEA.

5 SUMMARY AND CONCLUSIONS

This study employed the CALPHAD method, using the TCHEA5 and PanHEA2022 databases, and a combination of two empirical approaches, namely valence electron concentration (VEC) and paired sigma-forming element (PSFE), to investigate the phase equilibria and sigma phase formation in the CoCrFeMnNi system. Isothermal aging treatments were conducted at temperatures between 900 °C and 1100 °C for 20 h, as the predictions from CALPHAD and VEC/PSFE methods diverged regarding sigma phase formation.

Studies indicate that for the temperature range (900-1100 °C) and chosen time (20 h) there would be sufficient kinetic conditions for the formation of the sigma phase in these alloys, if it were stable. Additionally, the samples from this work were previously cold worked, since plastic deformation during cold rolling can also accelerate sigma phase formation within HEAs by providing heterogeneous nucleation sites within the grains.

In a comparative analysis of the experimental results obtained through SEM-BSE/EDS and HE-SXRD analysis with predictions using the Tsai criteria, it is evident that the Tsai criteria consistently provided accurate predictions for all alloy compositions, regardless of the studied temperatures, resulting in sigma-free alloys. Notably, the Tsai criteria do not predict the sigma phase fractions, but rather indicate whether the alloy compositions are sigma-prone, which is useful for designing alloys that avoid sigma phase formation entirely. It is essential to highlight that, unlike the Tsai criteria that predict the formation of a specific phase (sigma) in a limited alloy system, the CALPHAD method can provide thermodynamic properties and phase equilibrium diagrams for a wide range of materials, if appropriate databases exist. Improving the predictability of the CALPHAD method will require continuous updates and the development of new databases. Unlike traditional alloys, the number of components must be restricted to create a high-fidelity database for M/HEAs.

The decrease in SFE led to a transition in the dominant deformation behavior from TWIP (Co15Cr15) to TWIP/TRIP (Co20Cr20) and finally to TRIP (Co25Cr25), presenting a higher HCP phase content for the Co25Cr25 alloy.

The fully-recrystallized FCC single phase microstructures with grain sizes ranging from 2.7 μm to 102.5 μm were successfully obtained by cold rolling and subsequent annealing. Notably, the Co25Cr25 alloy exhibited relatively higher recrystallization and slower grain growth rates compared to the Co20Cr20 and Co15Cr15 alloys, possibly attributed to the nucleation of a second phase (strain-induced HCP martensitic phase) in the FCC matrix after the cold rolling, as well as different diffusion rates where we expect the latter to increase in the following order: Co25Cr25 < Co20Cr20 < Co15Cr15. However, further research is necessary to understand the detailed mechanisms governing the recrystallization and grain growth behavior of these alloys.

A Hall-Petch relationship was established, revealing that both σ_0 and k_{HP} are increased with increasing the G and decreasing the SFE. The Co25Cr25 exhibited the highest sensitivity of strength to grain size ($k_{HP} = 516$ MPa.μm$^{1/2}$), indicating high strengthenability through grain refinement. Furthermore, Co25Cr25 presented an optimal strength-ductility balance. The higher σ_y observed in this alloy, while partially attributed to the contributions of $\sigma_{\rho i}$ and σ_{ss}, was predominantly influenced by σ_{gb} (≈ 62%). Additionally, Co25Cr25 exhibited a high ε_{UE} (≈ 65%), which is shown to be a strong consequence of the TRIP effect. It is noteworthy that besides the TRIP, the TWIP effect also played a significant role in contributing to the high work hardening rate.

This study not only unravels the interplay between recrystallization, grain growth, and the Hall-Petch relationship but also offers deep insights into the mechanical performance, plasticity, and strengthening mechanisms of the newly-developed M/HEAs. The connection between composition and substructure makes these alloys ideal model materials for thermodynamics-guided alloy design. Further, this work sheds light on the development of novel FCC M/HEAs from the CoCrFeMnNi system, by identifying alloys that exhibit an optimal strength-ductility balance. The discussions and critiques presented in this study contribute to further delineating the compositional fields of M/HEAs, providing guidance for future research in the CoCrFeMnNi system.

6 RECOMMENDATIONS FOR FUTURE WORK

Based on the experience and knowledge acquired in carrying out this work, the following topics are proposed as recommendations for future works:

- Carry out in-situ synchrotron X-ray diffraction (HE-SXRD) experiments during deformation to determine the stress onset for the TWIP/TRIP effect; dislocation density in the material as a function of strain and the transformed phase amount;
- Perform tensile test at room temperature and subzero temperature to verify the temperature dependent deformation behavior (TRIP-TWIP) in order to find a superior combination of strength and ductility;
- Investigate the effect of FCC grain size on the TRIP↔TWIP transition;
- Analyze the corrosion and passive mechanism to verify if the compositional changes lead to an improvement in corrosion resistance;
- Study the effect of tuning composition and deformation mechanisms (TRIP/TWIP) on the wear resistance.

7 REFERENCES

[1] F.G. Coury, P. Wilson, K.D. Clarke, M.J. Kaufman, A.J. Clarke, High-throughput solid solution strengthening characterization in high entropy alloys, Acta Mater. 167 (2019) 1–11. https://doi.org/10.1016/j.actamat.2019.01.029.

[2] F.G. Coury, G. Zepon, C. Bolfarini, Multi-principal element alloys from the CrCoNi family: outlook and perspectives, J. Mater. Res. Technol. 15 (2021) 3461–3480. https://doi.org/10.1016/j.jmrt.2021.09.095.

[3] D.B. Miracle, O.N. Senkov, A critical review of high entropy alloys and related concepts, Acta Mater. 122 (2017) 448–511. https://doi.org/10.1016/j.actamat.2016.08.081.

[4] K. Ming, L. Li, Z. Li, X. Bi, J. Wang, Grain boundary decohesion by nanoclustering Ni and Cr separately in CrMnFeCoNi high-entropy alloys, Sci. Adv. 5 (2019). https://doi.org/10.1126/sciadv.aay0639.

[5] G. Laplanche, A. Kostka, O.M. Horst, G. Eggeler, E.P. George, Microstructure evolution and critical stress for twinning in the CrMnFeCoNi high-entropy alloy, Acta Mater. 118 (2016) 152–163. https://doi.org/10.1016/j.actamat.2016.07.038.

[6] Y. Deng, C.C. Tasan, K.G. Pradeep, H. Springer, A. Kostka, D. Raabe, Design of a twinning-induced plasticity high entropy alloy, Acta Mater. 94 (2015) 124–133. https://doi.org/10.1016/j.actamat.2015.04.014.

[7] M.J. Yao, K.G. Pradeep, C.C. Tasan, D. Raabe, A novel, single phase, non-equiatomic FeMnNiCoCr high-entropy alloy with exceptional phase stability and tensile ductility, Scr. Mater. 72–73 (2014) 5–8. https://doi.org/10.1016/j.scriptamat.2013.09.030.

[8] Z. Li, K.G. Pradeep, Y. Deng, D. Raabe, C.C. Tasan, Metastable high-entropy dual-phase alloys overcome the strength–ductility trade-off, Nature. 534 (2016) 227–230. https://doi.org/10.1038/nature17981.

[9] B. Cantor, I.T.H. Chang, P. Knight, A.J.B. Vincent, Microstructural

development in equiatomic multicomponent alloys, Mater. Sci. Eng. A. 375–377 (2004) 213–218. https://doi.org/10.1016/j.msea.2003.10.257.

[10] B. Gludovatz, A. Hohenwarter, K.V.S. Thurston, H. Bei, Z. Wu, E.P. George, R.O. Ritchie, Exceptional damage-tolerance of a medium-entropy alloy CrCoNi at cryogenic temperatures., Nat. Commun. 7 (2016) 10602. https://doi.org/10.1038/ncomms10602.

[11] F. Otto, Y. Yang, H. Bei, E.P. George, Relative effects of enthalpy and entropy on the phase stability of equiatomic high-entropy alloys, Acta Mater. 61 (2013) 2628–2638. https://doi.org/10.1016/j.actamat.2013.01.042.

[12] G. Laplanche, P. Gadaud, O. Horst, F. Otto, G. Eggeler, E.P. George, Temperature dependencies of the elastic moduli and thermal expansion coefficient of an equiatomic, single-phase CoCrFeMnNi high-entropy alloy, J. Alloys Compd. 623 (2015) 348–353. https://doi.org/10.1016/j.jallcom.2014.11.061.

[13] D. Wei, X. Li, J. Jiang, W. Heng, Y. Koizumi, W.-M. Choi, B.-J. Lee, H.S. Kim, H. Kato, A. Chiba, Novel Co-rich high performance twinning-induced plasticity (TWIP) and transformation-induced plasticity (TRIP) high-entropy alloys, Scr. Mater. 165 (2019) 39–43. https://doi.org/10.1016/j.scriptamat.2019.02.018.

[14] D. Wei, X. Li, W. Heng, Y. Koizumi, F. He, W.-M. Choi, B.-J. Lee, H.S. Kim, H. Kato, A. Chiba, Novel Co-rich high entropy alloys with superior tensile properties, Mater. Res. Lett. 7 (2019) 82–88. https://doi.org/10.1080/21663831.2018.1553803.

[15] Z. Li, D. Raabe, Strong and Ductile Non-equiatomic High-Entropy Alloys: Design, Processing, Microstructure, and Mechanical Properties, JOM. 69 (2017) 2099–2106. https://doi.org/10.1007/s11837-017-2540-2.

[16] J.-W. Yeh, S.-K. Chen, S.-J. Lin, J.-Y. Gan, T.-S. Chin, T.-T. Shun, C.-H. Tsau, S.-Y. Chang, Nanostructured High-Entropy Alloys with Multiple Principal Elements: Novel Alloy Design Concepts and Outcomes, Adv.

Eng. Mater. 6 (2004) 299–303. https://doi.org/10.1002/adem.200300567.

[17] B. Gludovatz, A. Hohenwarter, D. Catoor, E.H. Chang, E.P. George, R.O. Ritchie, A fracture-resistant high-entropy alloy for cryogenic applications, Science (80-.). 345 (2014) 1153–1158. https://doi.org/10.1126/science.1254581.

[18] O.N. Senkov, D.B. Miracle, K.J. Chaput, J.-P. Couzinie, Development and exploration of refractory high entropy alloys—A review, J. Mater. Res. 33 (2018) 3092–3128. https://doi.org/10.1557/jmr.2018.153.

[19] Y. Qiu, S. Thomas, M.A. Gibson, H.L. Fraser, N. Birbilis, Corrosion of high entropy alloys, Npj Mater. Degrad. 1 (2017) 15. https://doi.org/10.1038/s41529-017-0009-y.

[20] N. Birbilis, S. Choudhary, J.R. Scully, M.L. Taheri, A perspective on corrosion of multi-principal element alloys, Npj Mater. Degrad. 5 (2021) 14. https://doi.org/10.1038/s41529-021-00163-8.

[21] S. Gorsse, J.P. Couzinié, D.B. Miracle, From high-entropy alloys to complex concentrated alloys, Comptes Rendus Phys. 19 (2018) 721–736. https://doi.org/10.1016/j.crhy.2018.09.004.

[22] G. Bertoli, V.G.L. de Sousa, D. de A. Santana, L.B. Otani, C.S. Kiminami, F.G. Coury, Phase equilibria of VCrMnFeCo high entropy alloys, J. Alloys Compd. 903 (2022) 163950. https://doi.org/10.1016/j.jallcom.2022.163950.

[23] W. Zhang, P.K. Liaw, Y. Zhang, Science and technology in high-entropy alloys, Sci. China Mater. 61 (2018) 2–22. https://doi.org/10.1007/s40843-017-9195-8.

[24] K. Lu, The future of metals, Science (80-.). 328 (2010) 319–320. https://doi.org/10.1126/science.1185866.

[25] Y. Zhang, T.T. Zuo, Z. Tang, M.C. Gao, K.A. Dahmen, P.K. Liaw, Z.P. Lu, Microstructures and properties of high-entropy alloys, Prog. Mater. Sci. 61 (2014) 1–93. https://doi.org/10.1016/j.pmatsci.2013.10.001.

[26] Y.F. Ye, Q. Wang, J. Lu, C.T. Liu, Y. Yang, High-entropy alloy: challenges and prospects, Mater. Today. 19 (2016) 349–362. https://doi.org/10.1016/j.mattod.2015.11.026.

[27] E.P. George, D. Raabe, R.O. Ritchie, High-entropy alloys, Nat. Rev. Mater. 4 (2019) 515–534. https://doi.org/10.1038/s41578-019-0121-4.

[28] M.C. Gao, J.-W. Yeh, P.K. Liaw, Y. Zhang, High-Entropy Alloys: Fundamentals and Applications, Springer International Publishing, Cham, 2016. https://doi.org/10.1007/978-3-319-27013-5.

[29] B.S. Murty, J.-W. Yeh, S. Ranganathan, P.P. Bhattacharjee, High-Entropy Alloys, 2019.

[30] F. Otto, A. Dlouhý, C. Somsen, H. Bei, G. Eggeler, E.P. George, The influences of temperature and microstructure on the tensile properties of a CoCrFeMnNi high-entropy alloy, Acta Mater. 61 (2013) 5743–5755. https://doi.org/10.1016/j.actamat.2013.06.018.

[31] B. Schuh, F. Mendez-Martin, B. Völker, E.P. George, H. Clemens, R. Pippan, A. Hohenwarter, Mechanical properties, microstructure and thermal stability of a nanocrystalline CoCrFeMnNi high-entropy alloy after severe plastic deformation, Acta Mater. 96 (2015) 258–268. https://doi.org/10.1016/j.actamat.2015.06.025.

[32] S.F. Liu, Y. Wu, H.T. Wang, W.T. Lin, Y.Y. Shang, J.B. Liu, K. An, X.J. Liu, H. Wang, Z.P. Lu, Transformation-reinforced high-entropy alloys with superior mechanical properties via tailoring stacking fault energy, J. Alloys Compd. 792 (2019) 444–455. https://doi.org/10.1016/j.jallcom.2019.04.035.

[33] L. Tang, F.Q. Jiang, J.S. Wróbel, B. Liu, S. Kabra, R.X. Duan, J.H. Luan, Z.B. Jiao, M.M. Attallah, D. Nguyen-Manh, B. Cai, In situ neutron diffraction unravels deformation mechanisms of a strong and ductile FeCrNi medium entropy alloy, J. Mater. Sci. Technol. 116 (2022) 103–120. https://doi.org/10.1016/j.jmst.2021.10.034.

[34] J. Su, D. Raabe, Z. Li, Hierarchical microstructure design to tune the

mechanical behavior of an interstitial TRIP-TWIP high-entropy alloy, Acta Mater. 163 (2019) 40–54. https://doi.org/10.1016/j.actamat.2018.10.017.

[35] Z. Li, F. Körmann, B. Grabowski, J. Neugebauer, D. Raabe, Ab initio assisted design of quinary dual-phase high-entropy alloys with transformation-induced plasticity, Acta Mater. 136 (2017) 262–270. https://doi.org/10.1016/j.actamat.2017.07.023.

[36] X.H. Du, W.P. Li, H.T. Chang, T. Yang, G.S. Duan, B.L. Wu, J.C. Huang, F.R. Chen, C.T. Liu, W.S. Chuang, Y. Lu, M.L. Sui, E.W. Huang, Dual heterogeneous structures lead to ultrahigh strength and uniform ductility in a Co-Cr-Ni medium-entropy alloy, Nat. Commun. 11 (2020) 2390. https://doi.org/10.1038/s41467-020-16085-z.

[37] Y.-J. Liang, L. Wang, Y. Wen, B. Cheng, Q. Wu, T. Cao, Q. Xiao, Y. Xue, G. Sha, Y. Wang, Y. Ren, X. Li, L. Wang, F. Wang, H. Cai, High-content ductile coherent nanoprecipitates achieve ultrastrong high-entropy alloys, Nat. Commun. 9 (2018) 4063. https://doi.org/10.1038/s41467-018-06600-8.

[38] T. Yang, Y.L. Zhao, Y. Tong, Z.B. Jiao, J. Wei, J.X. Cai, X.D. Han, D. Chen, A. Hu, J.J. Kai, K. Lu, Y. Liu, C.T. Liu, Multicomponent intermetallic nanoparticles and superb mechanical behaviors of complex alloys, Science (80-.). 362 (2018) 933–937. https://doi.org/10.1126/science.aas8815.

[39] U. Sunkari, S.R. Reddy, B.D.S. Rathod, S.S.S. Kumar, R. Saha, S. Chatterjee, P.P. Bhattacharjee, Heterogeneous precipitation mediated heterogeneous nanostructure enhances strength-ductility synergy in severely cryo-rolled and annealed CoCrFeNi2.1Nb0.2 high entropy alloy, Sci. Rep. 10 (2020) 6056. https://doi.org/10.1038/s41598-020-63038-z.

[40] Z. Wu, C.M. Parish, H. Bei, Nano-twin mediated plasticity in carbon-containing FeNiCoCrMn high entropy alloys, J. Alloys Compd. 647 (2015) 815–822. https://doi.org/10.1016/j.jallcom.2015.05.224.

[41] Y. Yin, Q. Tan, Q. Sun, W. Ren, J. Zhang, S. Liu, Y. Liu, M. Bermingham,

H. Chen, M.-X. Zhang, Heterogeneous lamella design to tune the mechanical behaviour of a new cost-effective compositionally complicated alloy, J. Mater. Sci. Technol. 96 (2022) 113–125. https://doi.org/10.1016/j.jmst.2021.03.083.

[42] J.-W. Yeh, Alloy Design Strategies and Future Trends in High-Entropy Alloys, JOM. 65 (2013) 1759–1771. https://doi.org/10.1007/s11837-013-0761-6.

[43] J.-H. Li, M.-H. Tsai, Theories for predicting simple solid solution high-entropy alloys: Classification, accuracy, and important factors impacting accuracy, Scr. Mater. 188 (2020) 80–87. https://doi.org/10.1016/j.scriptamat.2020.06.064.

[44] D. Ma, B. Grabowski, F. Körmann, J. Neugebauer, D. Raabe, Ab initio thermodynamics of the CoCrFeMnNi high entropy alloy: Importance of entropy contributions beyond the configurational one, Acta Mater. 100 (2015) 90–97. https://doi.org/10.1016/j.actamat.2015.08.050.

[45] F. Tian, L. Delczeg, N. Chen, L.K. Varga, J. Shen, L. Vitos, Structural stability of NiCoFeCrAlx high-entropy alloy from ab initio theory, Phys. Rev. B. 88 (2013) 085128. https://doi.org/10.1103/PhysRevB.88.085128.

[46] F. Zhang, C. Zhang, S.L. Chen, J. Zhu, W.S. Cao, U.R. Kattner, An understanding of high entropy alloys from phase diagram calculations, Calphad. 45 (2014) 1–10. https://doi.org/10.1016/j.calphad.2013.10.006.

[47] O.N. Senkov, J.D. Miller, D.B. Miracle, C. Woodward, Accelerated exploration of multi-principal element alloys for structural applications, Calphad. 50 (2015) 32–48. https://doi.org/10.1016/j.calphad.2015.04.009.

[48] S. Gorsse, O. Senkov, About the Reliability of CALPHAD Predictions in Multicomponent Systems, Entropy. 20 (2018) 899. https://doi.org/10.3390/e20120899.

[49] M.E. Bloomfield, K.A. Christofidou, N.G. Jones, Effect of Co on the phase stability of CrMnFeCoxNi high entropy alloys following long-duration exposures at intermediate temperatures, Intermetallics. 114 (2019)

106582. https://doi.org/10.1016/j.intermet.2019.106582.

[50] G. Laplanche, S. Berglund, C. Reinhart, A. Kostka, F. Fox, E.P. George, Phase stability and kinetics of σ-phase precipitation in CrMnFeCoNi high-entropy alloys, Acta Mater. 161 (2018) 338–351. https://doi.org/10.1016/j.actamat.2018.09.040.

[51] G. Laplanche, Growth kinetics of σ-phase precipitates and underlying diffusion processes in CrMnFeCoNi high-entropy alloys, Acta Mater. 199 (2020) 193–208. https://doi.org/10.1016/j.actamat.2020.08.023.

[52] K.A. Christofidou, T.P. McAuliffe, P.M. Mignanelli, H.J. Stone, N.G. Jones, On the prediction and the formation of the sigma phase in CrMnCoFeNix high entropy alloys, J. Alloys Compd. 770 (2019) 285–293. https://doi.org/10.1016/j.jallcom.2018.08.032.

[53] A.J. Zaddach, R.O. Scattergood, C.C. Koch, Tensile properties of low-stacking fault energy high-entropy alloys, Mater. Sci. Eng. A. 636 (2015) 373–378. https://doi.org/10.1016/j.msea.2015.03.109.

[54] K. Ming, X. Bi, J. Wang, Microstructures and deformation mechanisms of Cr26Mn20Fe20Co20Ni14 alloys, Mater. Charact. 134 (2017) 194–201. https://doi.org/10.1016/j.matchar.2017.10.022.

[55] K. Feng, Y. Zhang, Z. Li, C. Yao, L. Yao, C. Fan, Corrosion properties of laser cladded CrCoNi medium entropy alloy coating, Surf. Coatings Technol. 397 (2020) 126004. https://doi.org/10.1016/j.surfcoat.2020.126004.

[56] G. Laplanche, U.F. Volkert, G. Eggeler, E.P. George, Oxidation Behavior of the CrMnFeCoNi High-Entropy Alloy, Oxid. Met. 85 (2016) 629–645. https://doi.org/10.1007/s11085-016-9616-1.

[57] U.R. Kattner, The Calphad Method and Its Role in Material and Process Development, Tecnol. Em Metal. Mater. e Mineração. 13 (2016) 3–15. https://doi.org/10.4322/2176-1523.1059.

[58] F.G. Coury, T. Butler, K. Chaput, A. Saville, J. Copley, J. Foltz, P. Mason, K. Clarke, M. Kaufman, A. Clarke, Phase equilibria, mechanical properties

and design of quaternary refractory high entropy alloys, Mater. Des. 155 (2018) 244–256. https://doi.org/10.1016/j.matdes.2018.06.003.

[59] M.H. Tsai, K.Y. Tsai, C.W. Tsai, C. Lee, C.C. Juan, J.W. Yeh, Criterion for sigma phase formation in Cr- and V-Containing high-entropy alloys, Mater. Res. Lett. 1 (2013) 207–212. https://doi.org/10.1080/21663831.2013.831382.

[60] M.H. Tsai, K.C. Chang, J.H. Li, R.C. Tsai, A.H. Cheng, A second criterion for sigma phase formation in high-entropy alloys, Mater. Res. Lett. 4 (2016) 90–95. https://doi.org/10.1080/21663831.2015.1121168.

[61] S. Guo, C. Ng, J. Lu, C.T. Liu, Effect of valence electron concentration on stability of fcc or bcc phase in high entropy alloys, J. Appl. Phys. 109 (2011) 1–5. https://doi.org/10.1063/1.3587228.

[62] ASM Handbook, Alloy Phase Diagrams, 2004.

[63] Z. Li, C.C. Tasan, H. Springer, B. Gault, D. Raabe, Interstitial atoms enable joint twinning and transformation induced plasticity in strong and ductile high-entropy alloys, Sci. Rep. 7 (2017) 40704. https://doi.org/10.1038/srep40704.

[64] D. Liu, Q. Wang, J. Wang, X.F. Chen, P. Jiang, F.P. Yuan, Z.Y. Cheng, E. Ma, X.L. Wu, Chemical short-range order in Fe50Mn30Co10Cr10 high-entropy alloy, Mater. Today Nano. 16 (2021) 100139. https://doi.org/10.1016/j.mtnano.2021.100139.

[65] R. Zhang, S. Zhao, J. Ding, Y. Chong, T. Jia, C. Ophus, M. Asta, R.O. Ritchie, A.M. Minor, Short-range order and its impact on the CrCoNi medium-entropy alloy, Nature. 581 (2020) 283–287. https://doi.org/10.1038/s41586-020-2275-z.

[66] Y. Wu, F. Zhang, X. Yuan, H. Huang, X. Wen, Y. Wang, M. Zhang, H. Wu, X. Liu, H. Wang, S. Jiang, Z. Lu, Short-range ordering and its effects on mechanical properties of high-entropy alloys, J. Mater. Sci. Technol. 62 (2021) 214–220. https://doi.org/10.1016/j.jmst.2020.06.018.

[67] P. Singh, A. V. Smirnov, D.D. Johnson, Atomic short-range order and

incipient long-range order in high-entropy alloys, Phys. Rev. B. 91 (2015) 224204. https://doi.org/10.1103/PhysRevB.91.224204.

[68] Q. Ding, Y. Zhang, X. Chen, X. Fu, D. Chen, S. Chen, L. Gu, F. Wei, H. Bei, Y. Gao, M. Wen, J. Li, Z. Zhang, T. Zhu, R.O. Ritchie, Q. Yu, Tuning element distribution, structure and properties by composition in high-entropy alloys, Nature. 574 (2019) 223–227. https://doi.org/10.1038/s41586-019-1617-1.

[69] X. Chen, Q. Wang, Z. Cheng, M. Zhu, H. Zhou, P. Jiang, L. Zhou, Q. Xue, F. Yuan, J. Zhu, X. Wu, E. Ma, Direct observation of chemical short-range order in a medium-entropy alloy, Nature. 592 (2021) 712–716. https://doi.org/10.1038/s41586-021-03428-z.

[70] W.H. Liu, Y. Wu, J.Y. He, T.G. Nieh, Z.P. Lu, Grain growth and the Hall–Petch relationship in a high-entropy FeCrNiCoMn alloy, Scr. Mater. 68 (2013) 526–529. https://doi.org/10.1016/j.scriptamat.2012.12.002.

[71] Y. Zou, H. Ma, R. Spolenak, Ultrastrong ductile and stable high-entropy alloys at small scales, Nat. Commun. 6 (2015) 7748. https://doi.org/10.1038/ncomms8748.

[72] Z. Zhang, M.M. Mao, J. Wang, B. Gludovatz, Z. Zhang, S.X. Mao, E.P. George, Q. Yu, R.O. Ritchie, Nanoscale origins of the damage tolerance of the high-entropy alloy CrMnFeCoNi, Nat. Commun. 6 (2015) 10143. https://doi.org/10.1038/ncomms10143.

[73] G. Bertoli, L.B. Otani, A.J. Clarke, C.S. Kiminami, F.G. Coury, Hall–Petch and grain growth kinetics of the low stacking fault energy TRIP Cr 40 Co 40 Ni 20 multi-principal element alloy, Appl. Phys. Lett. 119 (2021) 061903. https://doi.org/10.1063/5.0057888.

[74] Y.-C. Huang, C.-H. Su, S.-K. Wu, C. Lin, A Study on the Hall–Petch Relationship and Grain Growth Kinetics in FCC-Structured High/Medium Entropy Alloys, Entropy. 21 (2019) 297. https://doi.org/10.3390/e21030297.

[75] S.J. Sun, Y.Z. Tian, H.R. Lin, X.G. Dong, Y.H. Wang, Z.J. Wang, Z.F.

Zhang, Temperature dependence of the Hall–Petch relationship in CoCrFeMnNi high-entropy alloy, J. Alloys Compd. 806 (2019) 992–998. https://doi.org/10.1016/j.jallcom.2019.07.357.

[76] I. Ondicho, B. Alunda, N. Park, Effect of Fe on the Hall-Petch relationship of (CoCrMnNi) Fe medium-and high-entropy alloys, Intermetallics. 136 (2021) 107239. https://doi.org/10.1016/j.intermet.2021.107239.

[77] G. Laplanche, A. Kostka, C. Reinhart, J. Hunfeld, G. Eggeler, E.P. George, Reasons for the superior mechanical properties of medium-entropy CrCoNi compared to high-entropy CrMnFeCoNi, Acta Mater. 128 (2017) 292–303. https://doi.org/10.1016/j.actamat.2017.02.036.

[78] R.S. Haridas, P. Agrawal, S. Yadav, P. Agrawal, A. Gumaste, R.S. Mishra, Work hardening in metastable high entropy alloys: a modified five-parameter model, J. Mater. Res. Technol. 18 (2022) 3358–3372. https://doi.org/10.1016/j.jmrt.2022.04.016.

[79] B.C. De Cooman, Y. Estrin, S.K. Kim, Twinning-induced plasticity (TWIP) steels, Acta Mater. 142 (2018) 283–362. https://doi.org/10.1016/j.actamat.2017.06.046.

[80] B.C. De Cooman, K. Chin, J. Kim, High Mn TWIP Steels for Automotive Applications, in: New Trends Dev. Automot. Syst. Eng., InTech, 2011. https://doi.org/10.5772/14086.

[81] R. Li, S. Lu, D. Kim, S. Schönecker, J. Zhao, S.K. Kwon, L. Vitos, Stacking fault energy of face-centered cubic metals: thermodynamic and ab initio approaches, J. Phys. Condens. Matter. 28 (2016) 395001. https://doi.org/10.1088/0953-8984/28/39/395001.

[82] H. Idrissi, K. Renard, L. Ryelandt, D. Schryvers, P.J. Jacques, On the mechanism of twin formation in Fe–Mn–C TWIP steels, Acta Mater. 58 (2010) 2464–2476. https://doi.org/10.1016/j.actamat.2009.12.032.

[83] S. Kibey, J.B. Liu, D.D. Johnson, H. Sehitoglu, Predicting twinning stress in fcc metals: Linking twin-energy pathways to twin nucleation, Acta Mater. 55 (2007) 6843–6851.

https://doi.org/10.1016/j.actamat.2007.08.042.

[84] S. Huang, H. Huang, W. Li, D. Kim, S. Lu, X. Li, E. Holmström, S.K. Kwon, L. Vitos, Twinning in metastable high-entropy alloys, Nat. Commun. 9 (2018) 2381. https://doi.org/10.1038/s41467-018-04780-x.

[85] H.-U. Jeong, N. Park, TWIP and TRIP-associated mechanical behaviors of Fe (CoCrMnNi) medium-entropy ferrous alloys, Mater. Sci. Eng. A. 782 (2020) 138896. https://doi.org/10.1016/j.msea.2019.138896.

[86] X.D. Xu, P. Liu, Z. Tang, A. Hirata, S.X. Song, T.G. Nieh, P.K. Liaw, C.T. Liu, M.W. Chen, Transmission electron microscopy characterization of dislocation structure in a face-centered cubic high-entropy alloy Al0.1CoCrFeNi, Acta Mater. 144 (2018) 107–115. https://doi.org/10.1016/j.actamat.2017.10.050.

[87] Z. Wang, I. Baker, Z. Cai, S. Chen, J.D. Poplawsky, W. Guo, The effect of interstitial carbon on the mechanical properties and dislocation substructure evolution in Fe40.4Ni11.3Mn34.8Al7.5Cr6 high entropy alloys, Acta Mater. 120 (2016) 228–239. https://doi.org/10.1016/j.actamat.2016.08.072.

[88] A.K. Chandan, S. Tripathy, B. Sen, M. Ghosh, S. Ghosh Chowdhury, Temperature dependent deformation behavior and stacking fault energy of Fe40Mn40Co10Cr10 alloy, Scr. Mater. 199 (2021) 113891. https://doi.org/10.1016/j.scriptamat.2021.113891.

[89] A. Šalak, M. Selecká, Manganese in powder metallurgy steels, in: Manganese Powder Metall. Steels, Cambridge International Science Publishing, Cambridge, 2012: pp. 22–38. https://doi.org/10.1007/978-1-907343-75-9.

[90] W. Lu, X. Luo, Y. Yang, J. Zhang, B. Huang, Effects of Al addition on structural evolution and mechanical properties of the CrCoNi medium-entropy alloy, Mater. Chem. Phys. 238 (2019) 121841. https://doi.org/10.1016/j.matchemphys.2019.121841.

[91] B. Beausir, J.-J. Fundenberger, Analysis Tools for Electron and X-ray

diffraction, (2017). www.atex-software.eu.

[92] N. Schell, R. V. Martins, F. Beckmann, H.U. Ruhnau, R. Kiehn, A. Schreyer, The High Energy Materials Science Beamline at PETRA III, Mater. Sci. Forum. 571–572 (2008) 261–266. https://doi.org/10.4028/www.scientific.net/MSF.571-572.261.

[93] J. Kieffer, D. Karkoulis, PyFAI, a versatile library for azimuthal regrouping, J. Phys. Conf. Ser. 425 (2013) 202012. https://doi.org/10.1088/1742-6596/425/20/202012.

[94] P. Erdely, P. Staron, E. Maawad, N. Schell, J. Klose, S. Mayer, H. Clemens, Effect of hot rolling and primary annealing on the microstructure and texture of a β-stabilised γ-TiAl based alloy, Acta Mater. 126 (2017) 145–153. https://doi.org/10.1016/j.actamat.2016.12.056.

[95] D. Wimler, J. Lindemann, C. Gammer, P. Spoerk-Erdely, A. Stark, H. Clemens, S. Mayer, Novel intermetallic-reinforced near-α Ti alloys manufactured by spark plasma sintering, Mater. Sci. Eng. A. 792 (2020) 139798. https://doi.org/10.1016/j.msea.2020.139798.

[96] S.C. Bodner, M. Meindlhumer, T. Ziegelwanger, H. Winklmayr, T. Hatzenbichler, C. Schindelbacher, B. Sartory, M. Krobath, W. Ecker, N. Schell, J. Keckes, Correlative cross-sectional characterization of nitrided, carburized and shot-peened steels: synchrotron micro-X-ray diffraction analysis of stress, microstructure and phase gradients, J. Mater. Res. Technol. 11 (2021) 1396–1410. https://doi.org/10.1016/j.jmrt.2021.01.099.

[97] M. Truschner, A. Janda, S.C. Bodner, A. Keplinger, G. Mori, Effect of cold deformation on the stress corrosion cracking resistance of a high-strength stainless steel, J. Mater. Sci. 57 (2022) 20447–20461. https://doi.org/10.1007/s10853-022-07866-6.

[98] T. Ungár, Microstructural parameters from X-ray diffraction peak broadening, Scr. Mater. 51 (2004) 777–781. https://doi.org/10.1016/j.scriptamat.2004.05.007.

[99] T. Ungár, A. Borbély, The effect of dislocation contrast on x-ray line

broadening: A new approach to line profile analysis, Appl. Phys. Lett. 69 (1996) 3173–3175. https://doi.org/10.1063/1.117951.

[100] G.. Williamson, W.. Hall, X-ray line broadening from filed aluminium and wolfram, Acta Metall. 1 (1953) 22–31. https://doi.org/10.1016/0001-6160(53)90006-6.

[101] B.H. Toby, R.B. Von Dreele, GSAS-II: the genesis of a modern open-source all purpose crystallography software package, J. Appl. Crystallogr. 46 (2013) 544–549. https://doi.org/https://doi.org/10.1107/S0021889813003531.

[102] R.A. Renzetti, H.R.Z. Sandim, R.E. Bolmaro, P.A. Suzuki, A. Möslang, X-ray evaluation of dislocation density in ODS-Eurofer steel, Mater. Sci. Eng. A. 534 (2012) 142–146. https://doi.org/10.1016/j.msea.2011.11.051.

[103] T. Ungár, I. Dragomir, Á. Révész, A. Borbély, The contrast factors of dislocations in cubic crystals: The dislocation model of strain anisotropy in practice, J. Appl. Crystallogr. 32 (1999) 992–1002. https://doi.org/10.1107/S0021889899009334.

[104] ASTM E8/E8M-16 Standard Test Methods for Tension Testing of Metallic Materials, (2016).

[105] G. Bracq, M. Laurent-Brocq, L. Perrière, R. Pirès, J.-M. Joubert, I. Guillot, The fcc solid solution stability in the Co-Cr-Fe-Mn-Ni multi-component system, Acta Mater. 128 (2017) 327–336. https://doi.org/10.1016/j.actamat.2017.02.017.

[106] K.A. Christofidou, E.J. Pickering, P. Orsatti, P.M. Mignanelli, T.J.A. Slater, H.J. Stone, N.G. Jones, On the influence of Mn on the phase stability of the CrMnxFeCoNi high entropy alloys, Intermetallics. 92 (2018) 84–92. https://doi.org/10.1016/j.intermet.2017.09.011.

[107] F. Otto, A. Dlouhý, K.G. Pradeep, M. Kuběnová, D. Raabe, G. Eggeler, E.P. George, Decomposition of the single-phase high-entropy alloy CrMnFeCoNi after prolonged anneals at intermediate temperatures, Acta Mater. 112 (2016) 40–52. https://doi.org/10.1016/j.actamat.2016.04.005.

[108] M. Tian, C. Wu, Y. Liu, H. Peng, J. Wang, X. Su, Phase stability and microhardness of CoCrFeMnxNi2-x high entropy alloys, J. Alloys Compd. 811 (2019) 152025. https://doi.org/10.1016/j.jallcom.2019.152025.

[109] C. Zhang, J. Zhu, W.S. Cao, S.L. Chen, S.M. Liang, F. Zhang, Development of Phase-Based Databases via CALPHAD Method for the Design of High-Entropy Alloys, J. Phase Equilibria Diffus. 43 (2022) 678–690. https://doi.org/10.1007/s11669-022-00970-9.

[110] M.E. Bloomfield, K.A. Christofidou, F. Monni, Q. Yang, M. Hang, N.G. Jones, The influence of Fe variations on the phase stability of CrMnFexCoNi alloys following long-duration exposures at intermediate temperatures, Intermetallics. 131 (2021) 107108. https://doi.org/10.1016/j.intermet.2021.107108.

[111] Z.G. Zhu, K.H. Ma, X. Yang, C.H. Shek, Annealing effect on the phase stability and mechanical properties of (FeNiCrMn)(100−)Co high entropy alloys, J. Alloys Compd. 695 (2017) 2945–2950. https://doi.org/10.1016/j.jallcom.2016.11.376.

[112] J. Pang, T. Xiong, X. Wei, Z. Zhu, B. Zhang, Y. Zhou, X. Shao, Q. Jin, S. Zheng, X. Ma, Oxide MnCr2O4 induced pitting corrosion in high entropy alloy CrMnFeCoNi, Materialia. 6 (2019) 100275. https://doi.org/10.1016/j.mtla.2019.100275.

[113] K.-M. Hsu, S.-H. Chen, C.-S. Lin, Microstructure and corrosion behavior of FeCrNiCoMnx (x = 1.0, 0.6, 0.3, 0) high entropy alloys in 0.5 M H2SO4, Corros. Sci. 190 (2021) 109694. https://doi.org/10.1016/j.corsci.2021.109694.

[114] K.P. Yu, S.H. Feng, C. Ding, P. Yu, M.X. Huang, Improving anti-corrosion properties of CoCrFeMnNi high entropy alloy by introducing Si into nonmetallic inclusions, Corros. Sci. 208 (2022) 110616. https://doi.org/10.1016/j.corsci.2022.110616.

[115] E.J. Pickering, R. Muñoz-Moreno, H.J. Stone, N.G. Jones, Precipitation in the equiatomic high-entropy alloy CrMnFeCoNi, Scr. Mater. 113 (2016)

106–109. https://doi.org/10.1016/j.scriptamat.2015.10.025.

[116] K.-D. Liss, A. Bartels, A. Schreyer, H. Clemens, High-Energy X-Rays: A tool for Advanced Bulk Investigations in Materials Science and Physics, Textures Microstruct. 35 (2003) 219–252. https://doi.org/10.1080/07303300310001634952.

[117] R. Rakowski, G. Golovin, J. O'Neal, J. Zhang, P. Zhang, B. Zhao, M.D. Wilson, M.C. Veale, P. Seller, S. Chen, S. Banerjee, D. Umstadter, M. Fuchs, Single-shot structural analysis by high-energy X-ray diffraction using an ultrashort all-optical source, Sci. Rep. 7 (2017) 16603. https://doi.org/10.1038/s41598-017-16477-0.

[118] W. Zhang, J. Shen, J.P. Oliveira, H. Wang, S. Feng, N. Schell, B.J. Kooi, Y. Pei, Deformation processes of additively manufactured interstitial-strengthened high entropy alloy: In-situ high-energy synchrotron X-ray diffraction and microstructural appraisal, Addit. Manuf. 76 (2023) 103791. https://doi.org/10.1016/j.addma.2023.103791.

[119] J. Rouquette, J. Haines, G. Fraysse, A. Al-Zein, V. Bornand, M. Pintard, P. Papet, S. Hull, F.A. Gorelli, High-Pressure Structural and Vibrational Study of PbZr 0.40 Ti 0.60 O 3, Inorg. Chem. 47 (2008) 9898–9904. https://doi.org/10.1021/ic8008688.

[120] P. Fabrykiewicz, R. Przeniosło, I. Sosnowska, F. Fauth, Positive and negative monoclinic deformation of corundum-type trigonal crystal structures of M 2 O 3 metal oxides, Acta Crystallogr. Sect. B Struct. Sci. Cryst. Eng. Mater. 74 (2018) 660–672. https://doi.org/10.1107/S2052520618014968.

[121] M. Javed, A.A. Khan, J. Kazmi, M.A. Mohamed, M.S. Ahmed, Y. Iqbal, Impedance spectroscopic study of charge transport and relaxation mechanism in MnCr2O4 ceramic chromite, J. Alloys Compd. 854 (2021) 156996. https://doi.org/10.1016/j.jallcom.2020.156996.

[122] U. Halenius, F. Bosi, H. Skogby, Galaxite, MnAl2O4, a spectroscopic standard for tetrahedrally coordinated Mn2+ in oxygen-based mineral

structures, Am. Mineral. 92 (2007) 1225–1231. https://doi.org/10.2138/am.2007.2481.

[123] C. McCammon, Static compression of ?-MnS at 298 K to 21 GPa, Phys. Chem. Miner. 17 (1991). https://doi.org/10.1007/BF00203844.

[124] M. Baricco, S. Enzo, T.A. Baser, M. Satta, G. Vaughan, A.R. Yavari, Amorphous/nanocrystalline composites analysed by the Rietveld method, J. Alloys Compd. 495 (2010) 377–381. https://doi.org/10.1016/j.jallcom.2009.11.024.

[125] D. Ma, M. Yao, K.G. Pradeep, C.C. Tasan, H. Springer, D. Raabe, Phase stability of non-equiatomic CoCrFeMnNi high entropy alloys, Acta Mater. 98 (2015) 288–296. https://doi.org/10.1016/j.actamat.2015.07.030.

[126] O.N. Senkov, S.V. Senkova, C. Woodward, D.B. Miracle, Low-density, refractory multi-principal element alloys of the Cr–Nb–Ti–V–Zr system: Microstructure and phase analysis, Acta Mater. 61 (2013) 1545–1557. https://doi.org/10.1016/j.actamat.2012.11.032.

[127] H. Hamdi, H.R. Abedi, Y. Zhang, A review study on thermal stability of high entropy alloys: Normal/abnormal resistance of grain growth, J. Alloys Compd. 960 (2023) 170826. https://doi.org/10.1016/j.jallcom.2023.170826.

[128] P. Thirathipviwat, G. Song, J. Jayaraj, J. Bednarcik, H. Wendrock, T. Gemming, J. Freudenberger, K. Nielsch, J. Han, A comparison study of dislocation density, recrystallization and grain growth among nickel, FeNiCo ternary alloy and FeNiCoCrMn high entropy alloy, J. Alloys Compd. 790 (2019) 266–273. https://doi.org/10.1016/j.jallcom.2019.03.052.

[129] F.G. Coury, D. Santana, Y. Guo, J. Copley, L. Otani, S. Fonseca, G. Zepon, C. Kiminami, M. Kaufman, A. Clarke, Design and in-situ characterization of a strong and ductile co-rich multicomponent alloy with transformation induced plasticity, Scr. Mater. 173 (2019) 70–74. https://doi.org/10.1016/j.scriptamat.2019.07.045.

[130] M.H. Mohammad-Ebrahimi, A. Zarei-Hanzaki, H.R. Abedi, S.M. Vakili, C.K. Soundararajan, The enhanced static recrystallization kinetics of a non-equiatomic high entropy alloy through the reverse transformation of strain induced martensite, J. Alloys Compd. 806 (2019) 1550–1563. https://doi.org/10.1016/j.jallcom.2019.07.105.

[131] Y.T. Zhu, X.L. Wu, X.Z. Liao, J. Narayan, L.J. Kecskés, S.N. Mathaudhu, Dislocation–twin interactions in nanocrystalline fcc metals, Acta Mater. 59 (2011) 812–821. https://doi.org/10.1016/j.actamat.2010.10.028.

[132] H. Huang, J. Wang, H. Yang, S. Ji, H. Yu, Z. Liu, Strengthening CoCrNi medium-entropy alloy by tuning lattice defects, Scr. Mater. 188 (2020) 216–221. https://doi.org/10.1016/j.scriptamat.2020.07.027.

[133] F.C. Puosso, G. Bertoli, F.G. Coury, A Hall–Petch study of the high toughness Cr40Co30Ni30 multi-principal element alloy, J. Mater. Res. 38 (2023) 215–227. https://doi.org/10.1557/s43578-022-00729-5.

[134] M. Vaidya, K.G. Pradeep, B.S. Murty, G. Wilde, S. V. Divinski, Radioactive isotopes reveal a non sluggish kinetics of grain boundary diffusion in high entropy alloys, Sci. Rep. 7 (2017) 12293. https://doi.org/10.1038/s41598-017-12551-9.

[135] F.G. Coury, K.D. Clarke, C.S. Kiminami, M.J. Kaufman, A.J. Clarke, High Throughput Discovery and Design of Strong Multicomponent Metallic Solid Solutions, Sci. Rep. 8 (2018) 8600. https://doi.org/10.1038/s41598-018-26830-6.

[136] S. Allain, J.-P. Chateau, O. Bouaziz, S. Migot, N. Guelton, Correlations between the calculated stacking fault energy and the plasticity mechanisms in Fe–Mn–C alloys, Mater. Sci. Eng. A. 387–389 (2004) 158–162. https://doi.org/10.1016/j.msea.2004.01.059.

[137] O.A. Zambrano, Stacking Fault Energy Maps of Fe–Mn–Al–C–Si Steels: Effect of Temperature, Grain Size, and Variations in Compositions, J. Eng. Mater. Technol. 138 (2016). https://doi.org/10.1115/1.4033632.

[138] H. Gwon, J.H. Kim, J.-K. Kim, D.-W. Suh, S.-J. Kim, Role of grain size on

deformation microstructures and stretch-flangeability of TWIP steel, Mater. Sci. Eng. A. 773 (2020) 138861. https://doi.org/10.1016/j.msea.2019.138861.

[139] S. Lee, B.C. De Cooman, Annealing Temperature Dependence of the Tensile Behavior of 10 pct Mn Multi-phase TWIP-TRIP Steel, Metall. Mater. Trans. A. 45 (2014) 6039–6052. https://doi.org/10.1007/s11661-014-2540-6.

[140] B.K. Sahoo, V.C. Srivastava, B. Mahato, S. Ghosh Chowdhury, Microstructure-mechanical property evaluation and deformation mechanism in Al added medium Mn steel processed through intercritical rolling and annealing, Mater. Sci. Eng. A. 799 (2021) 140100. https://doi.org/10.1016/j.msea.2020.140100.

[141] S.Y. Jo, J. Han, J.-H. Kang, S. Kang, S. Lee, Y.-K. Lee, Relationship between grain size and ductile-to-brittle transition at room temperature in Fe–18Mn–0.6C–1.5Si twinning-induced plasticity steel, J. Alloys Compd. 627 (2015) 374–382. https://doi.org/10.1016/j.jallcom.2014.11.232.

[142] J.-Y. Lee, J.-S. Hong, S.-H. Kang, Y.-K. Lee, The effect of austenite grain size on deformation mechanism of Fe–17Mn steel, Mater. Sci. Eng. A. 809 (2021) 140972. https://doi.org/10.1016/j.msea.2021.140972.

[143] Y.-K. Lee, C. Choi, Driving force for γ→ε martensitic transformation and stacking fault energy of γ in Fe-Mn binary system, Metall. Mater. Trans. A. 31 (2000) 355–360. https://doi.org/10.1007/s11661-000-0271-3.

[144] E.O. Hall, The Deformation and Ageing of Mild Steel: III Discussion of Results, Proc. Phys. Soc. Sect. B. 64 (1951) 747–753. https://doi.org/10.1088/0370-1301/64/9/303.

[145] N.J. Petch, The cleavage strength of polycrystals, J. Iron Steel Inst. (1953) 25–28.

[146] N. Hansen, Hall–Petch relation and boundary strengthening, Scr. Mater. 51 (2004) 801–806. https://doi.org/10.1016/j.scriptamat.2004.06.002.

[147] D. Wei, W. Gong, T. Tsuru, T. Kawasaki, S. Harjo, B. Cai, P.K. Liaw, H.

Kato, Mechanical behaviors of equiatomic and near-equiatomic face-centered-cubic phase high-entropy alloys probed using in situ neutron diffraction, Int. J. Plast. 158 (2022) 103417. https://doi.org/10.1016/j.ijplas.2022.103417.

[148] Q.-J. Li, H. Sheng, E. Ma, Strengthening in multi-principal element alloys with local-chemical-order roughened dislocation pathways, Nat. Commun. 10 (2019) 3563. https://doi.org/10.1038/s41467-019-11464-7.

[149] N.L. Okamoto, K. Yuge, K. Tanaka, H. Inui, E.P. George, Atomic displacement in the CrMnFeCoNi high-entropy alloy – A scaling factor to predict solid solution strengthening, AIP Adv. 6 (2016). https://doi.org/10.1063/1.4971371.

[150] I. Toda-Caraballo, P.E.J. Rivera-Díaz-del-Castillo, Modelling solid solution hardening in high entropy alloys, Acta Mater. 85 (2015) 14–23. https://doi.org/10.1016/j.actamat.2014.11.014.

[151] C. Varvenne, A. Luque, W.A. Curtin, Theory of strengthening in fcc high entropy alloys, Acta Mater. 118 (2016) 164–176. https://doi.org/10.1016/j.actamat.2016.07.040.

[152] I. Shakhova, V. Dudko, A. Belyakov, K. Tsuzaki, R. Kaibyshev, Effect of large strain cold rolling and subsequent annealing on microstructure and mechanical properties of an austenitic stainless steel, Mater. Sci. Eng. A. 545 (2012) 176–186. https://doi.org/10.1016/j.msea.2012.02.101.

[153] Z.C. Cordero, B.E. Knight, C.A. Schuh, Six decades of the Hall–Petch effect – a survey of grain-size strengthening studies on pure metals, Int. Mater. Rev. 61 (2016) 495–512. https://doi.org/10.1080/09506608.2016.1191808.

[154] Z. Wu, H. Bei, F. Otto, G.M. Pharr, E.P. George, Recovery, recrystallization, grain growth and phase stability of a family of FCC-structured multi-component equiatomic solid solution alloys, Intermetallics. 46 (2014) 131–140. https://doi.org/10.1016/j.intermet.2013.10.024.

[155] E.P. George, W.A. Curtin, C.C. Tasan, High entropy alloys: A focused review of mechanical properties and deformation mechanisms, Acta Mater. 188 (2020) 435–474. https://doi.org/10.1016/j.actamat.2019.12.015.

[156] B. Yin, W.A. Curtin, First-principles-based prediction of yield strength in the RhIrPdPtNiCu high-entropy alloy, Npj Comput. Mater. 5 (2019) 14. https://doi.org/10.1038/s41524-019-0151-x.

[157] C. Varvenne, W.A. Curtin, Strengthening of high entropy alloys by dilute solute additions: CoCrFeNiAl and CoCrFeNiMnAl alloys, Scr. Mater. 138 (2017) 92–95. https://doi.org/10.1016/j.scriptamat.2017.05.035.

[158] F.J. Guo, Y.F. Wang, M.S. Wang, W. Wei, Q. He, Q.Y. Wang, C.X. Huang, R.R. Jin, The critical grain size for optimal strength–ductility synergy in CrCoNi medium entropy alloy, Scr. Mater. 218 (2022) 114808. https://doi.org/10.1016/j.scriptamat.2022.114808.

[159] A.S. Argon, Strengthening Mechanisms in Crystal Plasticity, Oxford University Press, 2008.

[160] T. Ungár, A.D. Stoica, G. Tichy, X.-L. Wang, Orientation-dependent evolution of the dislocation density in grain populations with different crystallographic orientations relative to the tensile axis in a polycrystalline aggregate of stainless steel, Acta Mater. 66 (2014) 251–261. https://doi.org/10.1016/j.actamat.2013.11.012.

[161] Z. Li, C.C. Tasan, K.G. Pradeep, D. Raabe, A TRIP-assisted dual-phase high-entropy alloy: Grain size and phase fraction effects on deformation behavior, Acta Mater. 131 (2017) 323–335. https://doi.org/10.1016/j.actamat.2017.03.069.

[162] Z. Zhang, H. Jing, L. Xu, Y. Han, L. Zhao, C. Zhou, Effects of nitrogen in shielding gas on microstructure evolution and localized corrosion behavior of duplex stainless steel welding joint, Appl. Surf. Sci. 404 (2017) 110–128. https://doi.org/10.1016/J.APSUSC.2017.01.252.

[163] J. Miao, C.E. Slone, T.M. Smith, C. Niu, H. Bei, M. Ghazisaeidi, G.M.

Pharr, M.J. Mills, The evolution of the deformation substructure in a Ni-Co-Cr equiatomic solid solution alloy, Acta Mater. 132 (2017) 35–48. https://doi.org/10.1016/j.actamat.2017.04.033.

[164] C.E. Slone, S. Chakraborty, J. Miao, E.P. George, M.J. Mills, S.R. Niezgoda, Influence of deformation induced nanoscale twinning and FCC-HCP transformation on hardening and texture development in medium-entropy CrCoNi alloy, Acta Mater. 158 (2018) 38–52. https://doi.org/10.1016/j.actamat.2018.07.028.

[165] S.I. Wright, M.M. Nowell, J.F. Bingert, A Comparison of Textures Measured Using X-Ray and Electron Backscatter Diffraction, Metall. Mater. Trans. A. 38 (2007) 1845–1855. https://doi.org/10.1007/s11661-007-9226-2.